ISSN 1451 - 9372 (Print)
ISSN 2217 - 7434 (Online)
APRIL-JUNE 2025
Vol.31, Number 2, 95-172

Chemical Industry & Chemical Engineering Quarterly

SERBIA
Belgrade
AChE

The AChE Journal for Chemical Engineering,
Biochemical Engineering, Chemical Technology,
New Materials, Renewable Energy and Chemistry

www.ache.org.rs/ciceq

Journal of the
Association of Chemical Engineers of
Serbia, Belgrade, Serbia

Chemical Industry &
Chemical Engineering
CI&CE Quarterly

EDITOR-In-Chief

Vlada B. Veljković
Faculty of Technology, University of Niš, Leskovac, Serbia
E-mail: veljkovicvb@yahoo.com

ASSOCIATE EDITORS

Srđan Pejanović
Department of Chemical Engineering, Faculty of Technology and Metallurgy, University of Belgrade, Belgrade, Serbia

Dunja Sokolović
Faculty of Technical Sceinces, University of Novi Sad, Serbia

Ivona Radović
Faculty of Technology and Metallurgy, University of Belgrade, Serbia

EDITORIAL BOARD (Serbia)

Đorđe Janaćković, Ivanka Popović, Viktor Nedović, Goran Nikolić, Sanja Podunavac-Kuzmanović, Siniša Dodić, Zoran Todorović, Olivera Stamenković, Marija Tasić, Jelena Avramović, Jasna Canadanovic-Brunet, Ivana Karabegović

ADVISORY BOARD (International)

Dragomir Bukur
Texas A&M University,
College Station, TX,
USA

Milorad Dudukovic
Washington University,
St. Luis, MO, USA

Jiri Hanika
Institute of Chemical Process Fundamentals, Academy of Sciences
of the Czech Republic, Prague, Czech Republic

Maria Jose Cocero
University of Valladolid,
Valladolid, Spain

Tajalli Keshavarz
University of Westminster,
London, UK

Zeljko Knez
University of Maribor,
Maribor, Slovenia

Igor Lacik
Polymer Institute of the Slovak Academy of Sciences,
Bratislava, Slovakia

Denis Poncelet
ENITIAA, Nantes, France

Ljubisa Radovic
Pen State University,
PA, USA

Peter Raspor
University of Ljubljana,
Ljubljana, Slovenia

Constantinos Vayenas
University of Patras,
Patras, Greece

Xenophon Verykios
University of Patras,
Patras, Greece

Ronnie Willaert
Vrije Universiteit,
Brussel, Belgium

Gordana Vunjak Novakovic
Columbia University,
New York, USA

Dimitrios P. Tassios
National Technical University of Athens,
Athens, Greece

Hui Liu
China University of Geosciences, Wuhan, China

FORMER EDITOR (2005-2007)

Professor Dejan Skala
University of Belgrade, Faculty of Technology and Metallurgy, Belgrade, Serbia

FORMER ASSOCIATE EDITORS

Milan Jakšić, *ICEHT/FORTH, University of Patras, Patras, Greece*
Jonjaua Ranogajec, *Faculty of Technology, University of Novi Sad, Novi Sad, Serbia*

Journal of the
Association of Chemical Engineers of
Serbia, Belgrade, Serbia

Chemical Industry &
Chemical Engineering
CI&CE Quarterly

Vol. 31 Belgrade, April-June 2025 No. 2

Chemical Industry & Chemical Engineering Quarterly (ISSN 1451-9372) is published quarterly by the Association of Chemical Engineers of Serbia, Kneza Miloša 9/I, 11000 Belgrade, Serbia

Editor:
Vlada B. Veljković
veljkovic@yahoo.com

Editorial Office:
Kneza Miloša 9/I, 11000 Belgrade, Serbia
Phone/Fax: +381 (0)11 3240 018
E-mail: shi@ache.org.rs
www.ache.org.rs

For publisher:
Ivana T. Drvenica

Secretary of the Editorial Office:
Slavica Desnica

Marketing and advertising:
AChE Marketing Office
Kneza Miloša 9/I, 11000 Belgrade, Serbia
Phone/Fax: +381 (0)11 3240 018

Publication of this Journal is supported by the Ministry of Education, Science and Technological Development of the Republic of Serbia

Subscription and advertisements make payable to the account of the Association of Chemical Engineers of Serbia, Belgrade, No. 205-2172-71, Komercijalna banka a.d., Beograd

Technical Editor:
Marija B. Tasić

Journal manager:
Aleksandar B. Dekanski

Printed by:
Faculty of Technology and Metallurgy, Research and Development Centre of Printing Technology, Karnegijeva 4, P.O. Box 3503, 11120 Belgrade, Serbia

Abstracting/Indexing:
Articles published in this Journal are indexed in *Thompson Reuters* products: *Science Citation Index - Expanded*™ - access *via Web of Science*®, part of *ISI Web of Knowledge*℠

CONTENTS

The activities of the Association of Chemical Engineers of Serbia are supported by:

**MINISTRY OF SCIENCE,
TECHNOLOGICAL DEVELOPMENT
AND INNOVATION
OF REPUBLIC OF SERBIA**

Faculty of Technology and
Metallurgy, University of Belgrade

Faculty of Science, University of Novi Sad

ITNMS
Institute for Technology of Nuclear
and Other Mineral Raw Materials,
Bekgrade

Faculty of Technology,
University of Novi Sad

Institute of Chemistry, Technology and Metallurgy,
University of Belgrade

Faculty of Technical Sciences
University of Novi Sad

Faculty of Technology,
University of Niš, Leskovac

Faculty of Technical Sciences,
University of Priština, Kosovska Mitrovica

IMS Institute, Belgrade

DCP HEMIGAL
Leskovac

Elixir Prahovo

CI&CEQ
Chemical Industry & Chemical Engineering Quarterly

Available online at
Association of the Chemical Engineers of Serbia *AChE*
www.ache.org.rs/CICEQ

Chem. Ind. Chem. Eng. Q. 31 (2) 95–104 (2025) CI&CEQ

IMENE GHEZAL[1,2]
ALI MOUSSA[1,2]
IMED BEN MARZOUG[1,3]
AHMIDA EL-ACHARI[4,5]
CHRISTINE CAMPAGNE[4,5]
FAOUZI SAKLI[1,3]

[1]Textile Engineering Laboratory, University of Monastir, Ksar-Hellal, Tunisia

[2]National Engineering School of Monastir, University of Monastir, Monastir, Tunisia

[3]Higher Institute of Technological Studies of Ksar-Hellal, Ksar-Hellal, Tunisia

[4]Université Lille Nord de France, Lille, France

[5]ENSAIT, GEMTEX, 2 Allée Louise et Victor Champier, Roubaix, France

SCIENTIFIC PAPER

UDC 66.02:678.7:544

DEVELOPMENT OF A BREATHABLE POLYMERIC MEMBRANE AND PROCESS OPTIMIZATION BY USING A GENERAL FULL FACTORIAL DESIGN

Article Highlights

- A hydrophilic membrane was produced with a knife on a roller-coating machine
- The membrane was mainly composed of aliphatic polyester polyurethane and acrylic ester copolymers
- The water vapor permeability index and absorption rate responses were analyzed
- The polymeric membrane formulation was optimized by using a general full factorial design
- The optimal membrane was judged breathable

Abstract

This research aimed to produce a breathable hydrophilic membrane that can be laminated to textile fabrics to enhance their resistance to water penetration without restricting their breathability. For this purpose, aliphatic polyester polyurethane and acrylic ester copolymers were used. Quantities of both chemicals were varied according to three levels each. A general full factorial design was used to analyze responses that were the water vapor permeability index (WVPI (%)) and the absorption rate (Abs rate (%)). The membrane synthesis process was then optimized by using the Minitab response optimizer. The optimum polymeric membrane water vapor permeability and absorption rate were equal to 504 g·m^{-2}·day^{-1} and 50.4%, respectively. Based on the results obtained, the developed polymeric membrane was judged breathable. The morphological aspect of the dense membrane was also analyzed. It was noticed that air bubbles with different morphological types appeared in the nonporous membrane structure. Finally, it was concluded that the developed membrane can be thermo-assembled with other textile layers to enhance their resistance to wind and water penetration without affecting their breathability.

Keywords: dense membrane; breathable membrane; absorption rate; water vapor permeability; windproofness.

Traditional fabrics made with natural fibers are hygroscopic and non-durable [1]. On the other hand, synthetic fibers are not as breathable as natural ones [2]. The emergence of polymeric membranes took place to facilitate the production of materials that ensure protection and comfort to the wearer [3–8]. In the 1970s, the first waterproof breathable membranes were developed and then laminated to textiles. Since then, these materials have been gaining interest due to their interesting properties such as their ability to protect the wearer against rain, wind, and snow while ensuring the evacuation of moisture vapor from the cloth's inner side to the surrounding atmosphere [9,10].

The space between the wearer's skin and the cloth is defined as the microclimate [2]. For wearer comfort, this microclimate should not be affected and the moisture between the skin and the cloth should be evacuated to the surrounding environment [2,11].

Waterproof breathable membranes can be used

Correspondence: I. Ghezal, Textile Engineering Laboratory, University of Monastir, 5070 Ksar-Hellal, Tunisia.
E-mail: elghezalimene@hotmail.com
Paper received: 2 February, 2024
Paper revised: 16 April, 2024
Paper accepted: 8 May, 2024

https://doi.org/10.2298/CICEQ240202017G

for producing directional water transport textile fabrics [12]. These membranes can be classified according to two categories: (a) microporous membranes and (b) hydrophilic ones [9,13]. For microporous membranes, water vapor transmission occurs through micropores. However, for hydrophilic ones, the moisture vapor is transmitted from the inner side to the outer side by sorption, diffusion, and desorption processes [2]. The adsorption of water vapor by the membrane surface depends on the used polymer hydrophilicity and the material matrix-free volume. Actually, water vapor molecules diffuse from the inner side to the outer side of the membrane by physicochemical interactions between water vapor molecules and membrane hydrophilic sites. This migration depends on water vapor pressure and concentration, surrounding temperature, and humidity [2].

In the textile area, the most used polymers for membrane synthesis are polyurethanes, polytetrafluoroethylenes, acrylics, and poly(amino acids) [13–16]. Waterborne polyurethanes are mainly used for enhancing the resistance to water penetration of textiles [17]. They are mixed with acrylates to obtain enhanced hydrophobicity and water penetration resistance [17,18]. However, previously developed membranes present a poor breathability [19]. Added to that, used processes for producing these membranes are complicated and not easily applicable [6]. Generally, air permeability, water vapor permeability, and wettability are among the most tested properties for evaluating membrane comfort performance [20].

Recently, many researchers focused on the development of porous membranes. Zhou *et al.* [21] used the electrospinning method for producing porous polyurethane-based membranes. They found that developed structures exhibit desirable breathable performances [21]. In another study [22], polyamide and polydimethylsiloxane were both used for preparing nanofibrous membranes. The direct electrospinning technique was employed [22]. It was found that the produced polymer material presented high breathability [22]. In a research conducted by Zhou *et al.* [23] heat treatment was applied to waterborne polyurethane membranes produced with emulsion electrospinning [23]. Ren *et al.* [24] also investigated the performances of post-heated silicone-based polyurethane/ polymethacrylate membranes constructed by the electrospinning technique [24]. Exceptional breathability results were obtained when evaluating the performances of porous membranes produced by Zhou *et al.* [23] and Ren *et al.* [24]. Lv *et al.* [25] incorporated halloysite nanotube nanofluids onto polyacrylonitrile porous membranes obtained by the electrospinning technology [25].

Despite the numerous studies devoted to the development of porous membranes, these structures still have some limits such as pores blocking which engender a drop in the membrane breathability and its structure deterioration [26]. To remedy this issue, many researchers tried to modify porous membrane surface chemistry with expensive and arduous methods [26]. Nevertheless, poor adhesion between deposit polymers and membrane surface was reported [26].

Other researchers focused on the development of nonporous membranes. Generally known, these polymer products are polyacrylonitrile-based and show low mechanical performances [9]. On the other hand, nonporous materials are almost always produced by the melt extrusion method. However, membranes obtained by this technique have low water vapor permeability [9]. In a study conducted by Gorji *et al.* [27] a dense membrane was produced with graphene oxide-based nanocomposite hydrogel. The obtained structure with amended breathability was judged suitable for producing protective garments [27].

In this research, a hydrophilic breathable membrane was produced by using a facile technique that does not require expensive equipment. The aim was to obtain an industrializable breathable membrane that could be laminated to other textile layers to enhance their surface hydrophobicity and resistance to water penetration without restricting their breathability.

MATERIAL AND METHODS

Chemicals and reagents

To produce the dense membrane, the first chemical product (Product (A)) was an aliphatic polyester polyurethane copolymer dispersion, namely Appretan® N5122 liq. The second one (Product (B)), namely Appretan® N92101 liq was an acrylic ester copolymer dispersion. A thickener (Lutexal CSN liq) was also used. All products were supplied from Archroma, Spain.

Polymeric membrane preparation

To obtain membranes with uniform thicknesses a Werner Mathis laboratory coating machine type AG (Oberhasi, Switzerland) was utilized. This machine is composed essentially of two compartments; a coating head and an oven. The coating head consists of a roller and a blade. The position of the blade can be adjusted by varying its height and the angle that it forms with the horizontal plane. The blade height can be adjusted to an accuracy of 0.01 mm with the aim of clock gauges. To obtain the polymeric membrane the blade was fixed at position four (this parameter defines the angle that forms the blade with the horizontal plane) and its height was adjusted at 0.8 mm. The membrane preparation process is presented in Figure 1.

Experimental design

The main parameters that can affect the membrane hydrophilicity are its thickness, the quantities of the two used products, and the polymer blend viscosity. For hydrophilic membranes, the lower the thickness, the higher the water vapor transmission rate [2,28].

In this research, it was not possible to obtain membranes with a blade height of less than 0.8 mm. The total thickness (thickness of the release fabric and the paste layer) was equal to 0.8 mm. The viscosity of the polymeric paste was fixed in a way to obtain a homogenous even layer. For each set of experiments, the thickener quantity was determined so that the same viscosity could be obtained for all prepared pastes. The viscosity of the prepared polymer blend was controlled by using a Brookfield DV-I viscometer (Massachusetts, USA). The viscosity mean value was fixed at 80000 Pa·s. The chosen viscosity value ensures the obtention of a polymeric paste that can be easily spread on the released textile fabric. Based on pre-tests, drying temperature and time were set at 115 °C and 3 min, respectively. For the crosslinking time, it was fixed at 3 min. The crosslinking temperature was specified by the product supplier and was equal to 165 °C. Dried and cured membranes were then removed from the textile carrier.

As a pre-test, the first membrane was prepared only with acrylic ester copolymer (Product (B)). The composition was 60 mL of distilled water and 40 g of acrylic ester copolymer. The paste viscosity was adjusted and fixed at 80000 Pa·s by adding 1.8 g of thickener. The water vapor permeability of the obtained membrane was 399.5 g·m^{-2}·day^{-1}. To enhance the membrane breathability, polyester polyurethane dispersion was added to the mixture. Both product quantities were chosen and fixed based on pre-tests. The lowest and the highest quantities for products (A) and (B) were determined in a way to obtain a breathable membrane that can be easily removed from the siliconized textile career.

To study the effects of both chemical products on the obtained membrane breathability, a general full factorial design was used. This design accommodates factors with more than two levels. For statistical analysis, the test significance level (α) was fixed at 10% which means that factors with p-values lower than 0.1 were considered significant. Factors that might influence the obtained membrane breathability were studied. These factors were polyester polyurethane copolymer and acrylic ester copolymer quantities. Studied factors and corresponding levels are recapitulated in Table 1.

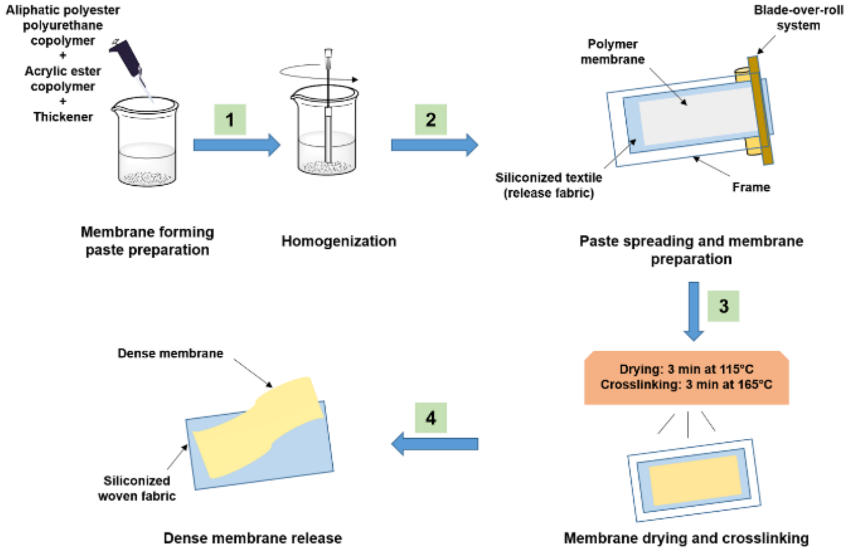

Figure 1. Membrane preparation process.

Table 1. Studied factors and corresponding levels.

Factors	Factor Codes	Variation Levels		
		Level 1	Level 2	Level 3
Product A quantity (g)	A	8	12	16
Product B quantity (g)	B	40	50	60

Product A: aliphatic polyester polyurethane dispersion. Product B: acrylic ester copolymer dispersion.

Using the Minitab 18 statistical software nine experiments were generated. Each experiment set was carried out three times. To evaluate the breathability of produced membranes, two responses were analyzed. These responses were the water vapor permeability index (WVPI (%)) and the absorption rate (Abs rate (%)). The effects of both used products on the studied responses were evaluated by using the ANOVA analysis tool. Factors and interactions with p-values equal to 0 were considered highly significant and those with p-values less or equal to 0.1 were considered significant. Optimum sets for inputs that give the highest absorption rate (%) and water vapor permeability index (%) values were also determined.

Absorption rate determination

To evaluate the absorption rates membrane square samples with an area equal to 25 cm² were weighed and impregnated in 100 mL of distilled water for 30 minutes then drained for 5 minutes. Samples were then re-weighed and absorption rate values were determined by using Eq. (1) [29]:

$$Abs\ rate(\%)=\frac{M_f-M_i}{M_i}\cdot 100 \tag{1}$$

where *Abs Rate (%)* is the membrane absorption rate, M_f (g) is the membrane mass after 30 minutes in distilled water and 5 minutes of draining time, and M_i (g) is the dry membrane mass.

Water vapor permeability index determination

To avoid discomfort feeling, perspiration should be evacuated from the skin to the surrounding atmosphere. The high water vapor permeability of a cloth assures a comfortable sensation to the wearer. On the other hand, fabric water vapor permeability (WVP) can be defined as the mass of water vapor that is transported through a unit area of fabric in a defined time [30–33].

To evaluate the breathability of produced membranes, a water vapor permeability apparatus type M261 (SDL Atlas, Rock Hill, USA) was used and WVPs (g·m^{-2}·day^{-1}) were determined as specified in the BS 7290:1990 standard and calculated by referring to Eq. (2) [34].

$$WVP\left(gm^{-2}day^{-1}\right)=\frac{24\cdot M_{loss}}{A\cdot t} \tag{2}$$

where M_{loss} (g) is the assembly (dish filled with distilled water, support, cover ring, and test membrane) mass loss after the testing period, A (m^2) is the exposed test membrane area, and t (h) is the testing time.

To eliminate errors due to conditioning a dense cellophane membrane, which was supplied from Measurement Technology Northwest, USA was used as a reference. The WVP of the reference membrane was determined and was equal to 1344 g·m^{-2}·day^{-1}. The water vapor permeability indexes (WVPIs (%)) for prepared membranes were then deduced by using Eq. (3) [34].

$$WVPI(\%)=\frac{WVP_{membrane}}{WVP_{reference}}\cdot 100 \tag{3}$$

where $WVP_{membrane}$ (g·m^{-2}·day^{-1}) is the water vapor permeability of the produced membrane and $WVP_{reference}$ (g·m^{-2}·day^{-1}) is the water vapor permeability of the reference cellophane membrane.

Surface free energy determination

The surface free energy of the optimal membrane was determined by referring to the Owens-Wendt-Rabel-Kaelble (OWRK) method. For this purpose, water (polar liquid) and diiodomethane solution (non-polar solution) were used. The wettability of the obtained product was evaluated by measuring contact angles that form each liquid with the dense membrane surface. For each liquid, an equation relating the membrane surface free energy polar and dispersive components to the contact angle was established (Eq. (4)) [35,36].

$$\gamma_L(1+\cos\theta_L)=2\sqrt{\gamma_{ds}\gamma_{dL}}+2\sqrt{\gamma_{ps}\gamma_{pL}} \tag{4}$$

where γ_L (mN·m^{-1}) is the used liquid surface tension, θ_L (°) is the measured contact angle, γ_{dS} and γ_{pS} (mN·m^{-1}) are respectively dispersive and polar components of the membrane surface free energy, and γ_{dL} and γ_{pL} (mN·m^{-1}) are respectively dispersive and polar components of the used liquid surface tension.

The resolution of the obtained two equations system and the determination of γ_{dS} and γ_{pS} (mN·m^{-1}) enable us to calculate their sum which corresponds to the surface free energy of the produced optimal membrane [35,36].

Membrane morphology analysis

The polymeric membrane external morphology was analyzed with a scanning electron microscope type Jeol, JSM-5400. The applied voltage for sample scanning was equal to 15 kV. Front and back sides as well as the section view of the membrane were captured with magnifications ranging from 50 to 350×.

RESULTS AND DISCUSSION

Study of the absorption rate

To prevent uncomfortable feelings resulting from transpiration accumulation, the water absorption rates of the produced membranes were measured. A general full factorial design was used to evaluate the effects of both used products on the Abs rate (%) response. Absorption rate values (%) of prepared membranes are recapitulated in Table 2.

Using the adjusted sum of squares for tests, the analysis of variance for the absorption rate response was elaborated and generated by the Minitab 18 software. Results from the two-way ANOVA analysis showed that product (B) had a significant effect on the studied response with a *p*-value lower than 0.1 (*p*-value = 0.059) and an adjusted sum of squares (Adj SS) equal to 338.06. The effect of product (A) was judged not significant (p-value = 0.583> 0.1). The main effects plot for the absorption rate is represented in Figure 2a. It was found that the quantities of products (A) and (B) had a negative effect on the absorption rate response.

For product (B) this effect was highly significant with a plotted line that was very steep from the *x*-axis. On average, when product (B) quantity was varied from 40 to 60 g, a decrease in the absorption rate percentage was noticed. Water absorption was influenced by the polymeric membrane composition. The variation of product (B) quantity had the most important effect on the mean absorption rate value. An augmentation in product (B) quantity indeed heightened the presence of hydrophilic sites (-O-) coming from the acrylic ester copolymer chains (Figure 3), however, a high concentration of this product exhibited the water absorption rate since it restricted chain inter-spaces and decreased the interactions between the hydrophilic groups of polymer chains and water molecules. Also, there are hydrophobic sites on the backbone chains of the acrylic ester copolymer. The presence of these sites also affected negatively the absorption rate. This explains the decrease in water absorption rate values when product (B) quantity was increased.

Table 2. Absorption rate values for the different prepared membranes.

Exp. N°	Factors		Thickener quantity (g)	Abs rate (%)	
	Product A (g)	Product B (g)		Mean values (%)	Coefficient of variation (%)
1	8	40	2.0	45.992	4.447
2	8	50	2.60	45.142	1.564
3	8	60	3.04	38.790	6.093
4	12	40	2.50	51.229	3.740
5	12	50	2.92	40.770	1.890
6	12	60	2.95	39.080	2.292
7	16	40	2.70	52.401	4.642
8	16	50	2.85	39.096	1.342
9	16	60	3.50	26.782	3.671

The absorption rate mean values (Abs rate (%)) are the average of three different measurements.

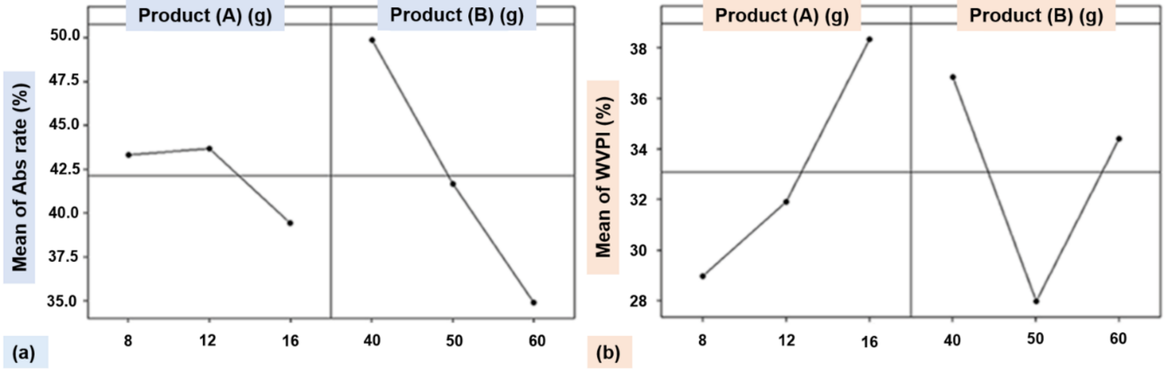

Figure 2. Main effects plots (data means) for: (a) Abs rate (%) and (b) WVPI (%) of the polymeric membranes studied.

On the other hand, when product (A) quantity was varied from 8 to 12 g the absorption rate increased. Yet, this augmentation is not important since the plotted line relating the two mean values for both categories is almost parallel to the x-axis. Added to that, a decrease

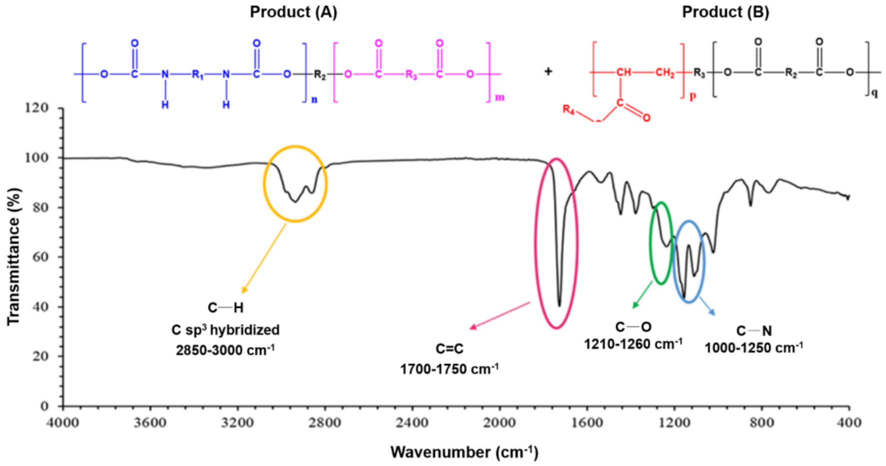

Figure 3. FT-IR spectrum of the membrane produced with polyurethane polyester and acrylic ester copolymer dispersions (Product A: polyester polyurethane copolymer; Product B: acrylic ester copolymer).

in absorption rate values was noticed when this product quantity was varied from 12 to 16 g. The interpretation made when varying product (B) quantity remains valid in this case.

Study of the water permeability index

The WVPI values (%) were measured for all prepared membranes. The obtained results are recapitulated in Table 3.

Table 3. WVPI (%) values for the different prepared membranes.

Exp. N°	Factors		WVPI (%)	
	Product A (g)	Product B (g)	Mean values (%)	CV (%)
1	8	40	34.478	2.073
2	8	50	21.239	0.685
3	8	60	30.747	3.438
4	12	40	38.139	1.453
5	12	50	25.806	4.73
6	12	60	31.778	2.81
7	16	40	37.510	1.283
8	16	50	36.787	4.7
9	16	60	40.715	4.35

The water vapor permeability index mean values (WVPI (%)) are the average of three different measurements.

The analysis of variance for the WVPI response was elaborated by using the adjusted sum of squares for tests. After ANOVA analysis, it was noticed that both studied products had a significant effect on the WVPI (%) with *p*-values lower than 0.1. *p*-values were equal to 0.082 and 0.093, respectively for products (A) and (B). It was concluded that product (A) had the most significant effect on the studied response with the lowest *p*-value and the highest adjusted sum of squares (Adj SS equal to 137.7 and 126.3 for products (A) and (B), respectively).

From the main effects plot of the WVPI (%) presented in Figure 2b, it can be noticed that as well as the quantity of product (A) increased there was an increase in the WVPI (%). For hydrophilic membranes, the water vapor permeability is governed by chemical interactions between polymer hydrophilic sites (Figure 3) and water vapor molecules. The rise in the water vapor permeability when increasing product (A) quantity was the result of the increase in the number of sites that can interact with water vapor molecules. In addition, the membrane thickness and the concentration of water vapor adsorbed and absorbed in the membrane polymeric matrix affected its water vapor transmission rate. As well as the thickness of the membrane increased, its water vapor permeability decreased.

Generally known, polyurethanes are hydrophobic [15]. On the other hand, for non-homogenous polymeric systems, the diffusion rate of water vapor molecules depends on their concentration in the membrane. The diffusion of water vapor molecules through the membrane can be described by Fick's second law [2].

Apart from this, considering that product (A) is a polyester polyurethane dispersion and that polyester polyurethane copolymer is not soluble in an aqueous solution, hydrophilic segments are generally incorporated in its chain to make it dispersible in water.

In this research, polymeric membranes with the same thickness were produced. When the quantity of product (A) was increased the amount of hydrophilic sites in the membrane was enhanced. As a result, the water vapor content on the membrane increased. Based on Fick's second law, the diffusion rate also rose. As a consequence, an augmentation in the water vapor permeability index was noticed.

For quantities of product (B) varying from 40 to 50 g, the WVPI (%) decreased. This is due to the restriction of the free volume in the polymeric matrix. Higher interactions between polymeric chains made amorphous region gaps and chain interspaces smaller which blocked the water vapor passage.

Optimization of the polymeric membrane formulation

To produce a membrane with the best performance in terms of breathability, a general full factorial design was used. Two factors that are the quantities of aliphatic polyester polyurethane (product (A)) and acrylic ester (product (B)) copolymers were studied. Analyzed and optimized responses were the absorption rate (%) and the water vapor permeability index (%). The set target was to maximize both studied responses to obtain a nonporous membrane with the highest performances in terms of water vapor permeability and absorption rate. The obtained optimized values are shown in Figure 4.

Predicted optimized values for the absorption rate (%) and the water vapor permeability index (%) were equal to 47.2 (d = 0.795) and 42.1% (d = 1), respectively. The composite desirability (D) was of 0.89. This value was close to the unit meaning that the obtained responses satisfied the set goals. The best performances in terms of absorption rate (%) and water vapor permeability index (%) were obtained with 16 and 40 g of product (A) and product (B), respectively. Based on the obtained results, the optimal membrane was judged breathable. The surface free energy (SFE, mN.m^{-1}) of the membrane produced with the optimized formulation was also determined by referring to the Owens-Wendt method [35,36]. Contact angles (Θ_{water}) and ($\Theta_{diiodomethane}$) were measured with distilled water and diiodomethane solution. Obtained results are shown in Table 4.

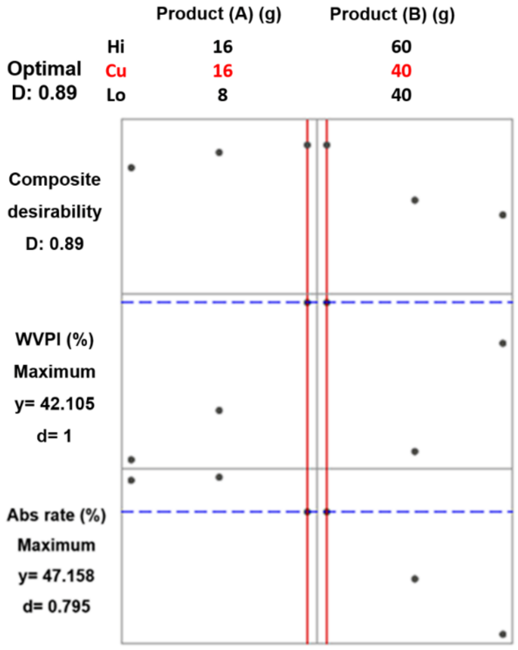

Figure 4. Polymeric membrane formulation optimization.

Table 4. Optimal membrane characteristics.

Characteristics	Values
Thickness [37]	293 µm ± 2.449 %
Mass per unit area [37]	152.96 g·m^{-2} ± 2.875 %
Θ_{water}	66° ± 8.557%
$\Theta_{diiodomethane}$	34° ± 8.98%
SFE	39.234 mN·m^{-1}
WVPI	37.510% ± 1.283%
Absorption rate	52.401% ± 4.642%
Air permeability [37]	0 L·m^{-2}·s^{-1}
RWP [37]	88.26 Schmerber ± 1.6%

Θ_{water} (°) and $\Theta_{diiodomethane}$ (°) are contact angles measured respectively with distilled water and diiodomethane solution, WVP (g·m^{-2}·day^{-1}) and WVPI (%) are respectively the water vapor permeability and the water vapor permeability index, and RWP (Schmerber) is the resistance to water penetration.

In a previous study done by Ghezal *et al.* [37], other physical characteristics of the optimal membrane such as the mass per unit area and the thickness were determined [37]. Ghezal *et al.* [37] also tested the air permeability (L·m^{-2}·s^{-1}) and the resistance to water penetration (RWP, Schmerber) of the developed optimal membrane. They concluded that the membrane's windproofness resulted from the absence of pores in the produced polymeric structure [37].

The external morphology of the produced dense membrane was also investigated. Front and back sides as well as the section view of the polymeric structure are shown in Figure 5.

Micrographs of the obtained membrane (Figures 5a, b, and c) displayed blind micropores. The produced material was considered a dense nonporous membrane since it contained closed pores. These blind micropores did not result from the presence of pore-forming agents nor the release of low-molecular-weight products during polymer materials thermosetting. From Figure 6, we noticed that the obtained blind micropores were of two different morphological types. These close micropores are not only caused by entrapped air in the paste mixture used for producing the polymer membrane but also by the method employed for the polymer mixture spreading on the siliconized textile.

After polymer layer thermosetting, the persistence of microfoam is the main reason for the appearance of these close micropores in the produced membranes.

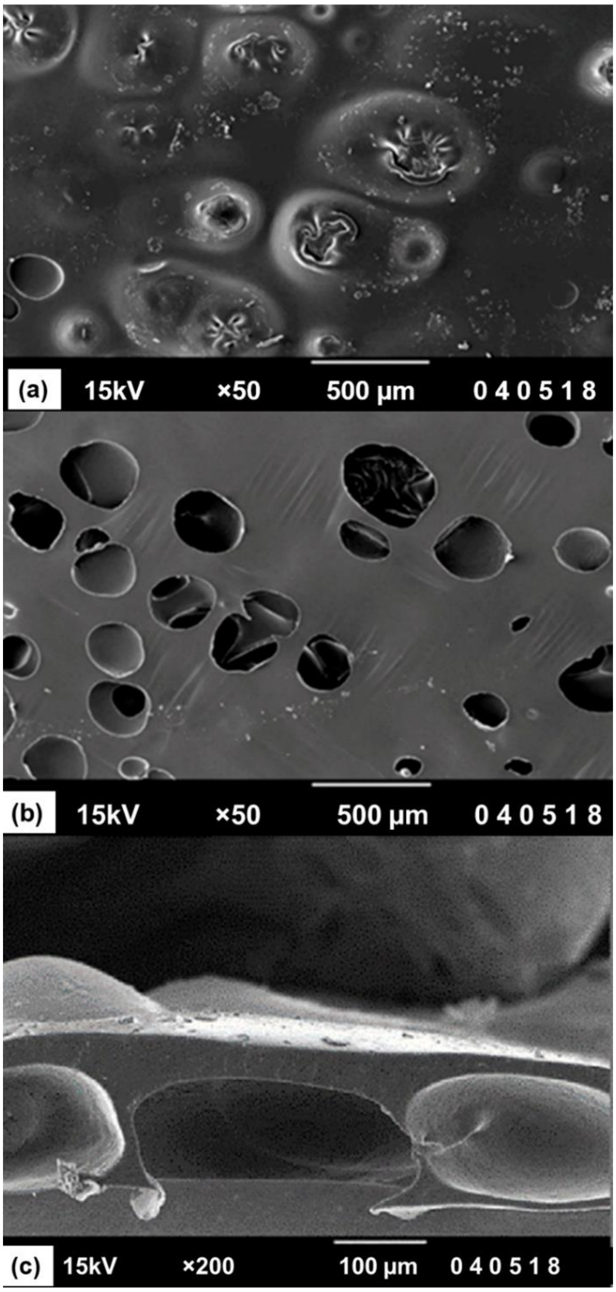

Figure 5. Scanning electron microscope image of the dense membrane (aliphatic polyester polyurethane dispersion: 16 g; acrylic ester copolymer dispersion: 40 g): (a) front side, (b) backside, and (c): section view.

The membrane side which was in direct contact with the siliconized textile fabric (Figure 5b) was smoother than its front side which presented some irregularities (Figure 5a).

CONCLUSION

The aim of this research was the development of a breathable membrane that can be laminated to textile and non-woven fabrics. Developed membranes were mainly made from aliphatic polyester polyurethane and acrylic ester copolymer dispersions. To optimize the membrane formulation, quantities of polyester polyurethane and acrylic ester copolymer dispersions were varied. Water vapor permeability index (%) and water absorption rate (%) responses were analyzed. For this purpose, a general full factorial design was employed. The effects of studied factors on both studied responses were investigated. Based on the obtained results, it was found that Product (B) quantity had the most significant effect on the water absorption rate. Considering obtained p-values it was found that both used products had a significant effect on studied responses.

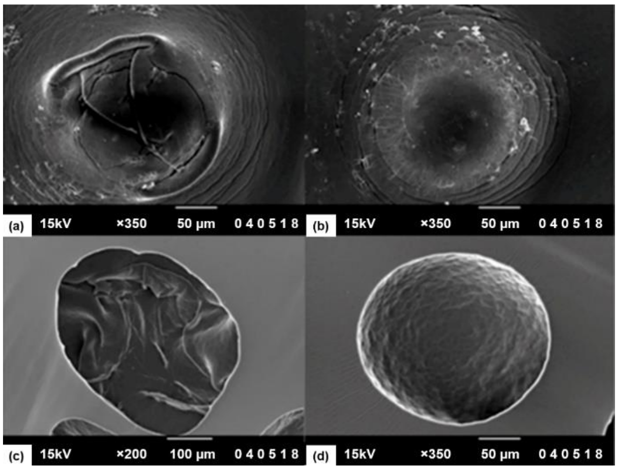

Figure 6. Scanning electron microscope image of air bubbles in the dense membrane (aliphatic polyester polyurethane dispersion (product A): 16 g; acrylic ester copolymer dispersion (product B): 40 g); (a, b) front views and (c, d) back views.

Determined optimal values of used products were equal to 16 g and 40 g, respectively for aliphatic polyester polyurethane and acrylic ester copolymers. Predicted optimized responses were 47.2% for the absorption rate and 42.1% for the WVPI. Finally, it was concluded that the developed membrane was breathable, windproof, and hydrophobic.

REFERENCES

[1] M. Zahid, G. Mazzon, A. Athanassiou, I.S. Bayer, Adv. Colloid Interface Sci. 270 (2019) 216–250. https://doi.org/10.1016/j.cis.2019.06.001.

[2] A. Gugliuzza, E. Drioli, J. Memb. Sci. 446 (2013) 350–375. https://doi.org/10.1016/j.memsci.2013.07.014.

[3] F.J. Maksoud, M. Lameh, S. Fayyad, N. Ismail, A.R. Tehrani-Bagha, N. Ghaddar, K. Ghali, J. Appl. Polym. Sci. 135 (2018) 45660. https://doi.org/10.1002/app.45660.

[4] Waterproof Breathable Fabrics Report, Balancing Performance and Environmental Sustainability,

https://www.innovationintextiles.com/waterproof-breathable-fabrics-balancing-performance-and-environmental-sustainability/ [accessed 2 February 2024].

[5] J. Sheng, Y. Xu, J. Yu, B. Ding, ACS Appl. Mater. Interfaces 9 (2017) 15139–15147. https://doi.org/10.1021/acsami.7b02594.

[6] J. Zhao, W. Zhu, X. Wang, L. Liu, J. Yu, B. Ding, ACS Nano 14 (2020) 1045–1054. https://doi.org/10.1021/acsnano.9b08595.

[7] F. Fornasiero, Curr. Opin. Chem. Eng. 16 (2017) 1–8. https://doi.org/10.1016/j.coche.2017.02.001.

[8] Y. Zhang, X. Li, H. Wang, B. Wang, J. Li, D. Cheng, Y. Lu, Nanomaterials 12 (2022) 3071. https://doi.org/10.3390/nano12173071.

[9] Y. Chang, F. Liu, Materials (Basel, Switz) 16 (2023) 5339. https://doi.org/10.3390/ma16155339.

[10] S. Shi, Y. Han, J. Hu, Prog. Org. Coat. 137 (2019) 105303. https://doi.org/10.1016/j.porgcoat.2019.105303.

[11] D. Negru, L. Buhu, E. Loghin, I. Dulgheriu, A. Buhu, Ind. Text. 68 (2017) 269–274. http://doi.org/10.35530/IT.068.04.1350.

[12] S. Shi, C. Zhi, S. Zhang, J. Yang, Y. Si, Y. Jiang, Y. Ming, K.T. Lau, B. Fei, J. Hu, ACS Appl. Mater. Interfaces 14 (2022) 39610–39621. https://doi.org/10.1021/acsami.2c11251.

[13] A. Mukhopadhyay, V.K. Midha, J. Ind. Text. 37 (2008) 225–262. https://doi.org/10.1177/1528083707082164.

[14] A. Mukhopadhyay, V.K. Vinay Kumar Midha, J. Ind. Text. 38 (2008) 17–41. https://doi.org/10.1177/1528083707082166.

[15] M. Gorji, M. Karimi, S. Nasheroahkam, J. Ind. Text. 47 (2018) 1166–1184. https://doi.org/10.1177/1528083716682920.

[16] E.-Y. Kim, J.-H. Lee, D.-J. Lee, Y.-H. Lee, J.-H. Lee, H.-D. Kim, J. Appl. Polym. Sci. 129 (2013) 1745–1751. https://doi.org/10.1002/app.38860.

[17] L. Sheng, X. Zhang, Z. Ge, Z. Liang, X. Liu, C. Chai, Y. Luo, J. Coat. Technol. Res. 15 (2018) 1283–1292. https://doi.org/10.1007/s11998-018-0096-x.

[18] Y. Ma, M. Zhang, W. Du, S. Sun, B. Zhao, Y. Cheng, Polymers (Basel, Switz). 15 (2023) 1759. https://doi.org/10.3390/polym15071759.

[19] Y. Guo, W. Zhou, L. Wang, Y. Dong, J. Yu, X. Li, B. Ding, ACS Appl. Bio Mater. 2 (2019) 5949–5956. https://doi.org/10.1021/acsabm.9b00875.

[20] Y. Zhang, T.T. Li, H.T. Ren, F. Sun, B.C. Shiu, C.W. Lou, J.H. Lin, J. Sandwich Struct. Mater. 23 (2021) 2817–2831. https://doi.org/10.1177/1099636220909750.

[21] W. Zhou, X. Gong, Y. Li, Y. Si, S. Zhang, J. Yu, B. Ding, J. Colloid Interface Sci. 602 (2021) 105–114. https://doi.org/10.1016/j.jcis.2021.05.171.

[22] W. Zhou, J. Yu, B. Ding, Compos. Commun. 35 (2022) 101337. https://doi.org/10.1016/j.coco.2022.101337.

[23] W. Zhou, X. Gong, Y. Li, Y. Si, S. Zhang, J. Yu, B. Ding, Chem. Eng. J. (Amsterdam, Neth.) 427 (2021) 130925. https://doi.org/10.1016/j.cej.2021.130925.

[24] G. Ren, Z. Li, L. Tian, D. Lu, Y. Jin, Y. Zhang, B. Li, H. Yu, HeJianxin, D. Sun, Colloids Surf., A 658 (2023) 130643. https://doi.org/10.1016/j.colsurfa.2022.130643.

[25] Y. Lv, X. Sun, S. Yan, S. Xiong, L. Wang, H. Wang, S. Yang, X. Yin, Compos. Commun. 33 (2022) 101211. https://doi.org/10.1016/j.coco.2022.101211.

[26] A. Saffar, P.J. Carreau, A. Ajji, M. R.Kamal, J. Membr. Sci. 462 (2014) 50–61. https://doi.org/10.1016/j.memsci.2014.03.024.

[27] M. Gorji, M. Karimi, G. Mashaiekhi, S. Ramazani, Polym.-Plast. Technol. Mater. 58 (2019) 182–192. https://doi.org/10.1080/03602559.2018.1466174.

[28] K.T. Djoko, H. Hadiyanto, D. Deariska, L. Nugraha, Chem. Ind. Chem. Eng. Q. 24 (2018) 139–147. https://doi.org/10.2298/CICEQ170112026K.

[29] Z. Li, X. Yue, G. He, Z. Li, Y. Yin, M. Gang, M. Gang, M. Gang, Z. Jiang, Int. J. Hydrogen Energy 40 (2015) 8398–8406. https://doi.org/10.1016/j.ijhydene.2015.04.138.

[30] B. Das, A. Das, V.K. Kothari, R. Fanguiero, M. de Araújo, Autex Res. J. 7 (2007) 100–110. https://doi.org/10.1515/aut-2007-070204.

[31] B. Das, A. Das, V.K. Kothari, R. Fangueiro, M. de Araújo, Autex Res. J. 7 (2007) 194–216. https://doi.org/10.1515/aut-2007-070305.

[32] A. Razzaque, P. Tesinova, L. Hes, J. Salacova, H.A. Abid, Fibers Polym. 18 (2017) 1924–1930. https://doi.org/10.1007/s12221-017-1154-1.

[33] J. Huang, Text. Res. J. 86 (2016) 325–336. https://doi.org/10.1177/0040517515588269.

[34] The British Standards Institution, BS 7209:Water Vapor Permeable Apparel Fabrics (1990). https://knowledge.bsigroup.com/products/specification-for-water-vapour-permeable-apparel-fabrics/standard.

[35] A. Rudawska, E. Jacniacka, Int. J. Adhes. Adhes. 29 (2009) 451–457. https://doi.org/10.1016/j.ijadhadh.2008.09.008.

[36] Lefebvre, G. (2011). [Ph.D. Thesis, University of Toulouse]. HAL Open Science. https://theses.hal.science/tel-04274825/document.

[37] I. Ghezal, A. Moussa, I. Ben Marzoug, A. El-Achari, C. Campagne, F. Sakli, Chem. Ind. Chem. Eng. Q. (2023). https://doi.org/10.2298/CICEQ230407029G.

IMENE GHEZAL[1,2]
ALI MOUSSA[1,2]
IMED BEN MARZOUG[1,3]
AHMIDA EL-ACHARI[4,5]
CHRISTINE CAMPAGNE[4,5]
FAOUZI SAKLI[1,3]

[1]Textile Engineering Laboratory, University of Monastir, Ksar-Hellal, Tunisia

[2]National Engineering School of Monastir, University of Monastir, Monastir, Tunisia

[3]Higher Institute of Technological Studies of Ksar-Hellal, Ksar-Hellal, Tunisia

[4]Université Lille Nord de France, Lille, France

[5]ENSAIT, GEMTEX, 2 Allée Louise et Victor Champier, Roubaix, France

NAUČNI RAD

RAZVOJ PROZRAČNE POLIMERNE MEMBRANE I OPTIMIZACIJA PROCESA OPŠTEG PUNOG FAKTORIJALNOG DIZAJNA

U ovom istraživanju, dobijena je prozračna hidrofilna membrana koja se može laminirati na tekstilne tkanine, kako bi se poboljšala njihova otpornost na prodiranje vode bez ograničavanja prozračnosti. U tu svrhu, korišćeni su alifatični poliestarski poliuretan i kopolimeri akrilnih estra. Količine obe hemikalije su varirale na tri nivoa. Opšti puni faktorijalni dizajn je korišćen za analizu odgovora, tj. indeksa propusnosti vodene pare i stepena apsorpcije. Proces sinteze membrane je zatim optimizovan korišćenjem softvera Minitab. Optimalna propustljivost vodene pare polimerne membrane bila je 504 g·m^{-2}·dan^{-1} i stepena apsorpcije 50,4%. Na osnovu dobijenih rezultata, dobijena polimerna membrana je ocenjena kao prozračna. Analiziran je i morfološki aspekt guste membrane. Uočeno je da se u neporoznoj strukturi membrane pojavljuju mehurići vazduha različitih morfoloških tipova. Konačno, zaključeno je da se dobijena membrana može termo-sastavljati sa drugim tekstilnim slojevima, kako bi se poboljšala njihova otpornost na vetar i prodor vode bez uticaja na prozračnost.

Ključne reči: gusta membrana; prozračna membrana; stepen apsorpcije; propustljivost vodene pare; otpornost na vetar.

CI&CEQ
Chemical Industry & Chemical Engineering Quarterly

Available online at
Association of the Chemical Engineers of Serbia *AChE*
www.ache.org.rs/CICEQ

Chem. Ind. Chem. Eng. Q. 31 (2) 105–111 (2025) CI&CEQ

AYUNI YUSTIRA[1]
HAFIFUDDIN ARIF[1]
ZAHEDI ZAHEDI[2]
FACHRUR RAZI[3]

[1]Department of Chemical Engineering, Faculty of Engineering Universitas Sumatera Utara Medan, Indonesia

[2]Department of Mathematics, Faculty of Mathematics and Natural Sciences Universitas Sumatera Utara Medan, Indonesia

[3]Department of Civil Engineering, Faculty of Engineering Universitas Al-Washliyah Medan, Indonesia

SCIENTIFIC PAPER

UDC 546.76:544.7:663.9:504.5

INFLUENCE OF ACTIVATORS ON SPENT COFFEE GROUNDS AS BIOSORBENT FOR CHROMIUM

Article Highlights

- Characteristic Adsorbent of Spent Coffee Ground (SCG)
- Determination of the best activator for iodine absorption
- Determination of pH of Cr solution
- Determination of contact time against the percentage of removal
- Determination of concentration to the percentage of Cr(VI) removal

Abstract

Global production of Cr(VI) can reach 44 million metric tons annually, of which 49% is released into the environment. Developments in the industry are to blame for this. There are numerous ways to defend against the damaging impact that heavy metals have on the environment. The presence of Cr(VI) causes environmental problems because it can endanger the physical and ecosystem balance of aquatic fauna in river flows. Exposure to Cr(VI) causes health problems such as liver, lung, and kidney damage. Adsorption is a straightforward, affordable, and user-friendly technique. The adsorbent utilized is derived from biomass waste, specifically spent coffee ground (SCG), but its potential as an adsorbent still needs to be developed. The purpose of this work was to examine the impact of activators on activated SCG and its capacity to adsorb Cr(VI) compounds. Nitric and bromide acid were used to activate 25 g of SCG for 1, 2, and 3 hours. Adsorbent-to-activator ratios were 1:4, 1:5, and 1:6. Cr(VI) solution was started at a concentration of 100 mg/L, and the adsorption process was stirred at 300 rpm. In the adsorption process, a ratio of 1:6 was best, along with an HNO_3 solution (pH 4) as the best activator, a contact time of 120 minutes, and an initial Cr(VI) concentration of 20 mg/L. OH is the major functional group of both adsorbents.

Keywords: Cr(VI) removal; nitric acid activator; bromide acid activator; spent coffee grounds bio-waste.

Wastewater containing heavy metals, such as Cr(VI) ions, which are a source of environmental contamination, is produced by mining, electrical equipment, leather tanning, and electroplating companies, or so-called anthropogenic activities [1]. Because heavy metals cannot break down they will be hazardous if they contaminate water. The overall annual output of chromium is 44 million metric tons, of which 49% is generated in Finland, Brazil, Zimbabwe, Kazakhstan, India, South Africa, Turkey, and Zimbabwe. Additionally, more than 170.000 tons of Cr(VI) are released into the environment annually [2,3].

The development of industrialization, urbanization, and globalization causes water pollution. Polluted water contains Cr(VI) ions. Hexavalent chromium is toxic and can be easily found in river flows. The presence of Cr(VI) ions causes environmental problems because they can endanger the physical and ecosystem balance of aquatic fauna in river flows [4,5]. Long-term exposure to high concentrations of Cr(VI) triggers liver, lung, and kidney damage. Meanwhile,

---

Correspondence: A. Yustira, Department of Chemical Engineering, Faculty of Engineering Universitas Sumatera Utara Medan 20155, Indonesia.
E-mail: ayuni@usu.ac.id
Paper received: 26 January, 2024
Paper revised: 9 May, 2024
Paper accepted: 14 May, 2024

https://doi.org/10.2298/CICEQ240126018Y

short-term exposure to Cr(VI) causes skin irritation. The maximum tolerable concentration of Cr(VI) set by the US Protection Agency (EPA) is 100 mg/L [6,7].

Certain heavy metal species are present in soil, water, and air streams. These species include Pb, Cu, Cd, Hg, As, Ni, and Cr. This is a result of rapid industrial development and poses a risk to human health as well as the environment at the moment [8,9]. The adsorption process is one of many strategies that can be employed to guard against the damaging effects of heavy metals on the environment. In theory, this strategy is straightforward, affordable, and simple to implement [10].

Research is currently focused on using biomass waste, such as potato skins [11], *Lathyrus sativus* husk [12], corncob [13], and garlic straw [14], to create a bio-adsorbent. Though coffee is the second most significant commodity in the world and the largest agricultural product after petroleum [15], the use of spent coffee ground (SCG), one of the biomass wastes, as an adsorbent is still neglected [16].

SCG is the residue left over after brewing coffee grinds [17]. If not properly treated, SCG frequently ends up as waste that pollutes the environment. Compared to the process, which requires high working temperatures, processing SCG as an adsorbent chemically with an activator has a number of advantages, including direct processing without treatment, operating at ambient temperature, and using less energy [18].

The selectivity and adsorption affinity of SCG are lower, and regeneration is inefficient due to the complexity of the polymers of SCG. However, several modification methods, such as physical, mechanical, and chemical, make SCG more efficient in the adsorption process. Therefore, the primary objective of this study was to improve the efficacy of modified SCG for Cr(VI) adsorption by altering the type of activator, adjusting the activator ratio, and varying the activation time. SCG was activated with solutions of nitric and bromide acids by opening the pores of SCG.

MATERIAL AND METHODS

Preparation and characterization of SCG

A total of 2 kg of SCG was obtained from Cafetaria Jl. Karya Waisata, Medan Johor, North Sumatra. The SCG was first washed with hot water (preheated to 100 °C) and then rinsed with clean water. Next, the SCG was dried in an oven at 55 °C for 24 hours. To make 1.000 ml of a synthetic Cr(VI) solution, 0.283 g of potassium dichromate ($K_2Cr_2O_7$) (Pudak. P.a ≥ 99.8%) was dissolved in water. Nitric (65%, Emsure) and bromic (48%, Chemie) acids were used as activators for adsorbent activation using the batch technique.

The purity of all the substances utilized was analytical. Fourier transform infrared (FTIR) was used to identify functional groups of the adsorbent material. FTIR wave readings were carried out in the middle spectrum region (mid-infrared) in the wavelength range of 400–4000 cm^{-1}. The results of the FTIR test were in the form of a graph between the wavelength (λ) on the *x*-axis and the amount of light reflected or the percentage (%) transmittance on the *y*-axis. FTIR test results were analyzed by looking at specific peaks at certain wavelengths. Each specific peak indicates a functional type in the adsorbent compound. Scanning electron microscope (SEM) analysis was carried out to determine the surface structure and particle size of each adsorbent. The SEM tool used was JSM-6510 LA, 20 kV 57 PA. The iodine number was carried out to determine the ability of each adsorbent activated by nitric or bromide acids to adsorb Cr(VI), where KI solution was used as an iodine solvent. To determine the iodine concentration, the iodometric titration method was used. The iodine number was measured for both the pre and post-activation states of SCG.

Activation procedure

Distilled water was used three times to get rid of contaminants that stuck to the SCG collected from the café. Next, the SCG is dried for 24 hours at a steady weight in an oven (Memmert, UF110) set to 55 °C. Following the process of drying, The SCG is activated with an activator of nitric and bromide acids (0,1 N), activation time of 1, 2, and 3 hours, and an activator to the adsorbent ratio of 1:4, 1:5, and 1:6. After that, the treated adsorbent was dried for two hours at 110 °C using Whatman No. 40 filter paper to remove it from the acid solution and wash it with distilled water until the pH was neutral [19].

Adsorption experiment

The adsorbent was activated using inorganic acids, and the adsorption test was conducted at room temperature using the batch method. In a 250 mL glass beaker, up to 25 g of adsorbent was combined with a synthetic Cr(VI) solution. A hotplate magnetic stirrer 79 min^{-1} was used to stir the mixture under the following adsorption working parameters: 300 rpm stirring, pH 1–5, and 60–140 minutes of contact time. After filtering the mixture, an atomic adsorption spectrometer (AAS-7000) was used to measure the concentration of the Cr(VI) synthesis solution before and after adsorption. The determination of Cr(VI) removal was calculated using the following equation [17]:

$$\text{Removal}(\%) = \frac{C_i - C_e}{C_i} \cdot 100 \quad (1)$$

where C_i is the initial concentration of the solution Cr(VI) (mg/L) and C_e is the equilibrium concentration of the solution Cr(VI) (mg/L).

RESULTS AND DISCUSSION

Adsorbent characteristics

Pore structure analysis using scanning electron microscope (SEM)

Figure 1 shows the findings of the SEM analysis for the SCG activated by nitric and bromide acids. They indicate a particle shape change, with the surface having large holes and a uniformly rough texture. It can be believed that the activators like strong acids can facilitate the release of contaminants from the SCG material and the dehydration process in the activation process, hence enabling the formation of larger holes.

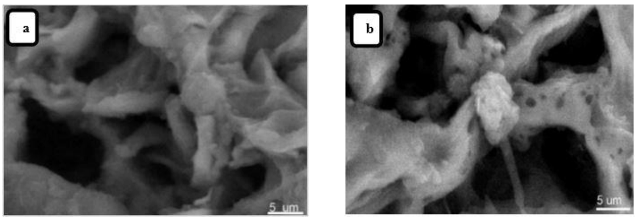

Figure 1. SEM micrographs of the surface morphology of SCG activated with (a) nitric acid, and (b) bromide acid.

Surface functional group analysis of SCG by FTIR

FTIR is employed in the absorption process to identify the adsorbent's functional groups that can interact with the adsorbate [20].

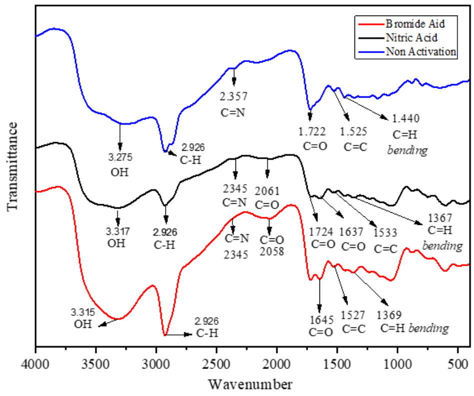

Figure 2. FTIR spectra of activated and non-activated SCG.

FTIR spectra of SCG activated by bromide or nitric acid are shown in Figure 2. The results of the infrared (IR) analysis produce the broadest absorption peaks with a spectrum value of 3316 cm^{-1} for activators bromide and nitric acids as big 3318 cm^{-1} as well as indicated by the presence of compounds O-H (Hydrogen bonds, alcohols, and phenols). The presence of compound elements C-H (alkanes) for activator bromide and nitric acids identified at the adsorption peak 2926,01 cm^{-1}, adsorption peak 2345 cm^{-1} identified compounds C=N that is a triple bond. In the SCG activation process, bonds C=O were identified at the absorption peaks 2058 cm^{-1}and 1645 cm^{-1} for the bromide acid-activated SCG and 2062 cm^{-1}, 1724 cm^{-1}, and 1636 cm^{-1} for the nitric acid-activated SCG. The bond strain C=O can be associated with amino acids and derivatives of xanthene in the form of caffeine and carboxylic acids from pectin, esters, and aldehydes, which in the adsorption process can participate [18].

The existence of aromatic ring compounds (C=C) was discovered at the absorption peak 1369 cm^{-1} for bromide acid and 1368 cm^{-1} for nitric acid, which indicated the C-H bending. The peaks of bromide acid and nitric acids are at 2058 cm^{-1} and 2062 cm^{-1}, respectively. The molecules C-O (carboxyl) detected by activator Bromide acid have an absorption peak of 1056.99 cm^{-1}.

The functional groups of SCG were activated using inorganic acids, so the FTIR analysis was utilized to identify the compound elements that contained C=N (triple bond), OH, C-H (alkanes), C=O, aromatic ring (C=C), C-H bending, and C-O (carboxyl). In addition, with a different and increasing number of OH intensities in the activated adsorbent, the OH group is an ideal active site, and at the same time, indicates that the resulting adsorbent is negatively charged. The research results obtained agree with Imessaoudene *et al.* [21] who used SCG in adsorbing cobalt.

The activator's ability to adsorb iodine

The iodimetric titration method is used to determine the adsorption capacity and quality of adsorbent in adsorbing the adsorbate, where the adsorbed amount of iodine serves as an indicator. SCG can adsorb iodine because it contains OH compounds. When SCG is activated using nitric or bromide acid, the intensity of OH compounds in SCG continues to increase, whereas the OH group becomes an ideal active site for the adsorption of iodine by SCG. Figure 3 shows that the adsorption value of iodine differs for two adsorbents due to differences in the ability of solutions or activators to facilitate the pyrolytic decomposition process for the formation of structures related to pores and the surface area of the adsorbent. The adsorption capacity of iodine can be greatly impacted by hydration and pyrolytic breakdown that occur in the adsorbent material [22]. The surface area of the adsorbent is also related to the ability of each activator to increase the porosity characteristics of the adsorbent so that the iodine adsorption capacity increases significantly [23].

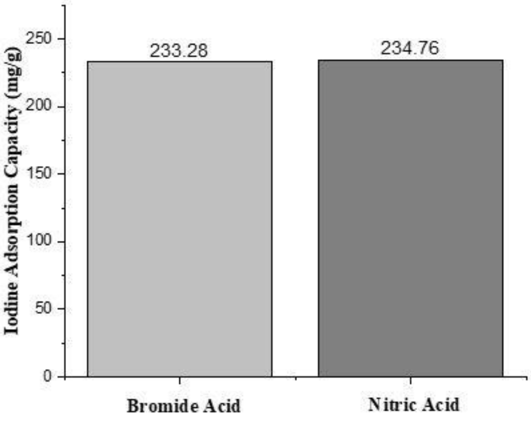

Figure 3. The activator's ability to adsorb iodine.

Determination of the best activator

The adsorption atom spectrometer (AAS-7000) can be used to examine the initial and final concentrations of the Cr(VI) solution. In the adsorption procedure, 25 mL of Cr(VI) solution at a concentration of 100 mg/L, 60 minutes of contact time, and 300 rpm stirring rate were utilized. There is a considerable variation in the percentage of each adsorbent activated with inorganic acids; bromide and nitric acids have the highest percentages of elimination Cr(VI) at 86.2% and 86.7%, respectively. This is ascribed to the resultant pores, so the surface area becomes more open, impacting the adsorption; on the other hand, the activating ingredient of the inorganic acid utilized can volatile compounds and remove adhering impurities or metal linked to the adsorbent. [22,23].

Effect of pH on Cr(VI) removal

The force of attraction between the adsorbent and the adsorbate is a mechanism of adsorption. The pH variation used in this experiment was 1–5. This aims to determine the best pH conditions for the adsorption of Cr(VI) using an adsorbent activated by bromide and nitric acids. The concentration of the solution was 100 mg/L, the adsorbent dose was 25 g, the contact time was 60 minutes, and the stirring rate was 300 rpm.

Figure 5 shows the removal of Cr(VI) using an adsorbent activated with inorganic acids. The maximum removals of Cr(VI) were 98.9% and 98.4% for the nitric and bromide acid-activated SCGs, respectively, at pH 4. At pH 5, the percentage of Cr(VI) removal decreases because when the acidic pH comes into contact with lignocellulose materials, it will reduce Cr(VI) to Cr(III). Adsorption of Cr(VI) ions using coffee grounds adsorbent is more beneficial at low pH because at low pH chromium reduction occurs, namely a reaction that binds protons so that it can reduce Cr(VI) to Cr(III) [24]. Maximum Cr(VI) removal efficiency can be achieved at low pH due to the presence of various forms of chromium because it can reduce the SCG surface charge [25].

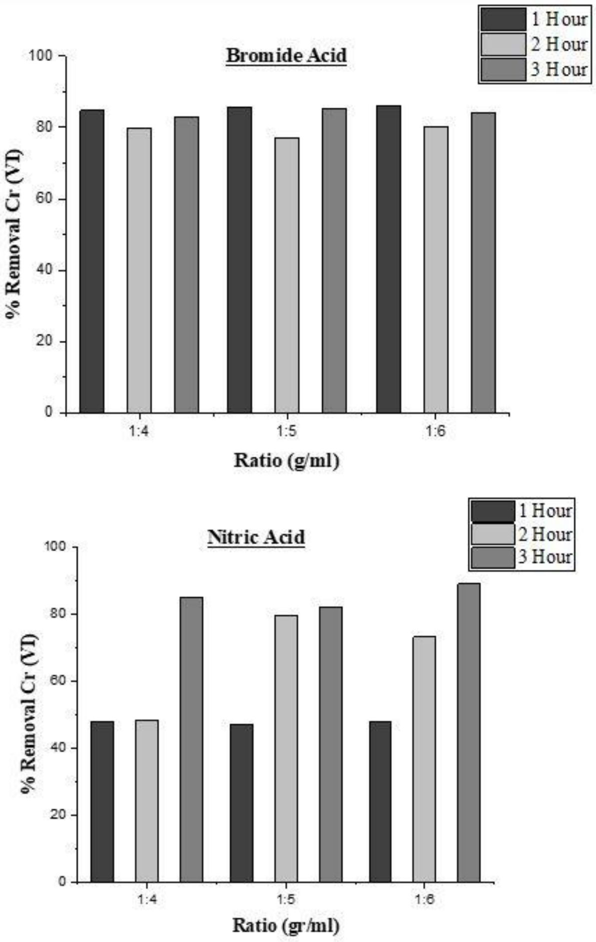

Figure 4. Uptake (percentage of removal) of Cr(VI) by investigated materials.

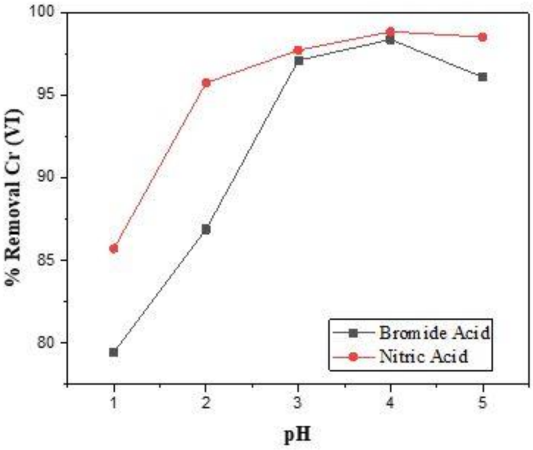

Figure 5. The influence of working pH on Cr(VI) removal.

Effect of contact time on Cr(VI) removal

Another crucial factor in the adsorption process is the contact time, which is utilized to calculate the ideal mixing [26]. The time variable (60–140 minutes), the adsorbent weight (25 g/L), the initial Cr(VI) concentration (100 mg/L), pH 4 (obtained from earlier investigations), and the stirring rate (300 rpm) were the working parameters.

With an optimal contact time of 120 minutes, the maximum percentages of Cr(VI) removal obtained were 97.9% and 94.9% for the nitric and bromide acid-activated (Figure 6). SCG, as an adsorbent, demonstrated a significant increase in the percentage of removal as the contact time increased due to a large number of active sites participating in chromate ion adsorption, which will be gradually used up as the contact time is longer [20].

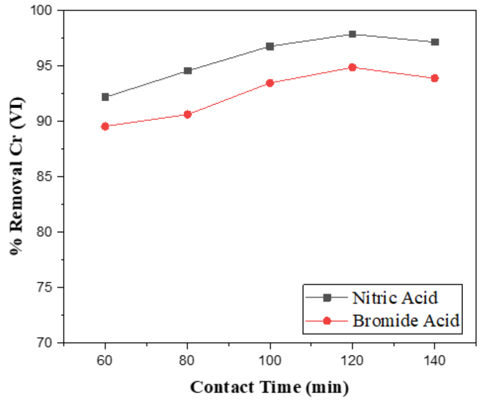

Figure 6. The influence of contact time between adsorbent and pollutant on Cr(VI) adsorption.

Effect of the initial concentration of Cr(VI) on the percentage removal

The operating conditions used in the experiment to determine the effect of the initial Cr(VI) concentration on the percentage of Cr(VI) removal were obtained from earlier experiments. These conditions included a 120-minute contact time, an adsorbent weight of 25 g/l, a pH of 4, and a stirring rate of 300 rpm. The Cr(VI) concentration employed in this experiment was varied at 20, 50, 80, 110, and 140 mg/L.

As the initial Cr(VI) concentration increased, the percentage of removal Cr(VI) dropped. It is depicted in Figure 7, showing that 20 mg/L is the ideal concentration for the adsorbents activated with nitric or bromide acid. This is attributed to the availability of a larger surface area of the adsorbent at low concentrations that might accelerate the adsorption [27]. On the other hand, the percentage of removal is low at higher concentrations, as the sites undergo saturation, allowing for the maximal adsorption of metal ions [28].

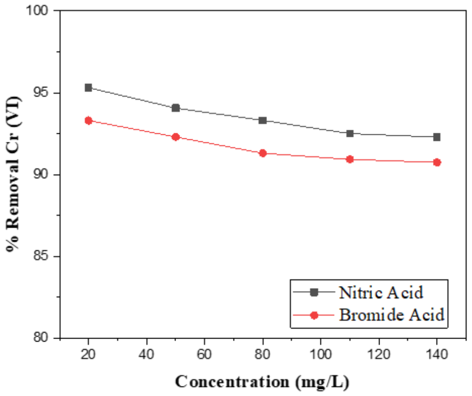

Figure 7. The influence of the initial concentration of Cr(VI) on the percentage of its removal.

CONCLUSION

In this study, the ability of SCG to absorb Cr(VI) as a pollutant was investigated. The effectiveness of nitric and bromic acids as SCG activators was also investigated. SCG was initially activated with nitric and bromide acids for three hours. The SCG activated with nitric acid provided the best iodine adsorption results by showing a removal percentage of 88.9% (an adsorption value of 235 mg/g) at an adsorbent-to-activator ratio of 1:6. Based on the SEM examination results, the adsorbent activated with nitric acid had a larger surface texture and more cavities compared to the adsorbent activated with bromic acid. The most dominant functional group of the two adsorbents is the OH group. In testing the adsorption process, the best operating conditions were determined, namely pH 4, contact time 120 minutes, and solution concentration 20 mg/L.

SCG is used as an adsorbent because it, as a biomass waste, is easy to obtain. However, the use of SCG as an adsorbent requires further activation to increase the adsorption capability. Therefore, it has not been used more widely in wastewater treatment processes. The application of SCG-based adsorbents in wastewater treatment has challenges because SCG adsorbents require the use of strong acid solutions, such as nitric and bromide acids, which are not safe and environmentally friendly. Potential limitations or obstacles in the use of strong acid as an activator can be overcome using an alternative activator that is more environmentally friendly or an adsorbent of natural origin with a higher percentage of adsorption without activation. Future potential or findings that are in line with the use of SCG are that it has been widely used as an adsorbent of contaminants in the form of dyes, Pb and Cr(III), active carbon precursors, and for composting.

REFERENCES

[1] H. Zeng, H. Zeng, H. Zhang, A. Shahab, K. Zang, Y. Lu, I. Nabi, F. Naseem, H. Ullah, J. Cleaner Prod. 286 (2021) 124964. https://doi.org/10.1016/j.jclepro.2020.124964.

[2] K.P. Nickens, S.R. Patierno, S. Ceryak, Chem. Biol. Interact. 188 (2010) 276–288. https://doi.org/10.1016/j.cbi.2010.04.018

[3] C.R. Myers, Free Radicals Biol. Med. 52 (2012) 2091–2107. http://doi.org/10.1016/j.freeradbiomed.2012.03.013.

[4] M.E. González-López, C.M. Laureano-Anzaldo, A.A. Pérez-Fonseca, M. Arellano, J.R. Robledo-Ortíz, Sep. Purif. Rev. 50 (2021) 333–362. https://doi.org/10.1080/15422119.2020.1783311.

[5] I. Loulidi, F Biukhlifi, M Ouchabi, A Amar, M Jabri, A Kali, C Hadey. Int Jour. Che. Eng. (2021) 11. https://doi.org/10.1155/ 2021/9977817.

[6] E. Cerrahoğlu Kaçakgil, S. Çetintaş.Sustain Chem. Pharm. 22 (2021) 100468. https://doi.org/10.1016/j.scp.2021.100468.

[7] M. E. González-López, C. M. Laureano-Anzaldo, A. A. Pérez-Fonseca, M. Arellano, J. R. Robledo-Ortíz. Sep. Purif. Rev. 50 (2021) 333–362. https://doi.org/10.1080/15422119.2020.1783311.

[8] N. Sankararamakrishnan, A. Dixit, L. Iyengar, R. Sanghi. Bio. Tech. 97 (2006) 2377–2382. https://doi.org/10.1016/j.biortech.2005.10.024.

[9] A. Parus, D. Rosińska, B. Karbowska, Chem. Ecol. 3(2020) 16–20. https://doi.org/10.1080/02757540.2019.1676418.

[10] E. Sharifikolouei, F. Baino, C. Galletti, D. Fino, M. Ferraris, Int. J. Appl. Ceram. Technol. 17 (2020) 105–112. https://doi.org/10.1111/ijac.13356.

[11] K. Bouhadjra, W. Lemlikchi, A. Ferhati, S. Mignard, Sci. Rep. 11 (2021) https://doi.org/10.1038/s41598-020-79069-5.

[12] I. Ghosh, S. Kar, T. Chatterjee, N. Bar, S. K. Das, Process Saf. Environ. Prot. 149 (2021) 345–361. https://doi.org/10.1016/j.psep.2020.11.003.

[13] M.E. Peñafiel, J.M. Matesanz, E. Vanegas, D. Bermejo, M.P. Ormad, Sep. Sci. Technol. 55 (2020) 3060–3071. https://doi.org/10.1080/01496395.2019.1673414.

[14] F. Kallel, F. Chaari, F. Bouaziz, F. Bettaieb, R. Ghorbel, S.E. Chaabouni, J. Mol. Liq. 219 (2016) 279–288. https://doi.org/10.1016/j.molliq.2016.03.024.

[15] A. Kovalcik, S. Obruca, I. Marova, Food Bioprod. Process. 110 (2018) 104–119. https://doi.org/10.1016/j.fbp.2018.05.002.

[16] I. Loulidi, F. Boukhlifi, M. Ouchabi, A. Amar, M. Jabri, A. Kali, C. Hadey, Int. J. Chem. Eng. 2021 (2021) https://doi.org/10.1155/2021/9977817.

[17] H.Y. Koay, A.T. Azman, Z. Mohd Zin, K.L Portman, M. Hasmadi, N.D Rusli, O. Aidat, M.K. Zainol, Future Foods 8 (2023) 100245. https://doi.org/10.1016/j.fufo.2023.100245.

[18] K. Ting Lee, Y. Tse Shih, S. Rajendran, Y. Kwon Park, W. Hsin Chen, Environ. Pollut. 324 (2023) 121330. https://doi.org/10.1016/j.envpol.2023.121330.

[19] G.V. Krishna Mohan, A. Naga Babu, K. Kalpana, K. Ravindhranath, Int. J. Environ. Sci. Technol. 16 (2019) 101–112. https://doi.org/10.1007/s13762-017-1593-7.

[20] I. Anastopoulos, M. Karamesouti, A.C. Mitropoulos, G.Z. Kyzas, J. Mol. Liq. 229 (2017) 555–565. https://doi.org/10.1016/j.molliq.2016.12.096.

[21] D. Imessaoudene, S. Hanini, A. Bouzidi, A. Ararem, Desalin. Water Treat. 57 (2016) 6116–6123. https://doi.org/10.1080/19443994.2015.1041049.

[22] N. Feng, X. Guo, S. Liang, Y. Zhu, J. Liu, J. Hazard. Mater. 185 (2011) 49–54. https://doi.org/10.1016/j.jhazmat. 2010.08.114.

[23] M. Amirudin, E. Novita, T. Tasliman, Agroteknika 3 (2020) 99–108. https://doi.org/10.32530/agroteknika.v3i2.73.

[24] N. Fiol, C. Escudero, I. Villaescusa, Sep. Sci. Technol. 43 (2008) 582–596. https://doi.org/10.1080/01496390701812418.

[25] F. Benmahdi, S. Khettaf, M. Kolli. Bio. Conv. Bio. 14 (2024) 7087–7101. https://doi.org/10.1007/s13399-022-03041-8.

[26] H. Zian, I. Ulfin, dan Harmami, J. Sain. Sen. ITS 5 (2016) 107–110. https://ejurnal.its.ac.id/index.php/sains seni/article /view/17119/0.

[27] P. Senthil Kumar, S. Ramalingam, C. Senthamarai, M. Niranjanaa, P. Vijayalakshmi, S. Sivanesan, Desalination 261(2010) 52–60. https://doi.org/10.1016/j.desal.2010.05.032.

[28] N. Azouaou, Z. Sadaoui, A. Djaafri, H. Mokaddem, J. Hazard. Mater. 184 (2010) 126–134. https://doi.org/10.1016/j.jhazmat.2010.08.014.

AYUNI YUSTIRA[1]
HAFIFUDDIN ARIF[1]
ZAHEDI ZAHEDI[2]
FACHRUR RAZI[3]

[1]Department of Chemical Engineering, Faculty of Engineering Universitas Sumatera Utara Medan, Indonesia

[2]Department of Mathematics, Faculty of Mathematics and Natural Sciences Universitas Sumatera Utara Medan, Indonesia

[3]Department of Civil Engineering, Faculty of Engineering Universitas Al-Washliyah Medan, Indonesia

NAUČNI RAD

UTICAJ AKTIVATORA NA OTPADNI TALOG KAFE KAO BIOSORBENTA ZA HROM

Globalna proizvodnja Cr(VI) može dostići 44 miliona metričkih tona godišnje, od čega se 49% ispušta u životnu sredinu za šta je kriv razvoj industrije. Prisustvo Cr(VI) izaziva ekološke probleme jer može ugroziti fizičku i ekosistemsku ravnotežu vodene faune u rečnim tokovima. Izloženost Cr(VI) izaziva zdravstvene probleme, kao što su oštećenje jetre, pluća i bubrega. Postoje brojni načini za odbranu od štetnog uticaja koji teški metali imaju na životnu sredinu. Adsorpcija je jednostavna, pristupačna i laka tehnika. Adsorbent koršćen u ovom radu je dobijen iz otpada biomase, tj. korišćene mlevene kafe (SCG). Njegov potencijal kao adsorbenta tek treba da se razvije. Svrha ovog rada je bila da se ispita uticaj aktivatora na SCG i njegov kapacitet da adsorbuje Cr(VI) jedinjenja. Azotna i bromidna kiselina su korišćene za aktiviranje 25 g SCG tokom 1, 2 i 3 sata. Odnosi adsorbenta i aktivatora bili su 1:4, 1:5 i 1:6. Početna koncentracija rastvora Cr(VI) je 100 mg/l, a a brzina mešanja 300 o/min. Najbolji rezultati adsorpcije postignuti su sa rastvorom HNO_3 (pH 4) kao boljim aktivatorom pri odnosu 1:6, vremenom kontakta 120 minuta i početnoj koncentracija Cr(VI) 20 mg/l. OH je glavna funkcionalna grupa oba adsorbenta.

Ključne reči: uklanjanje Cr(VI); azotna kiselina; bromidna kiselina; otpadni talog kafe.

CI&CEQ
Chemical Industry & Chemical Engineering Quarterly

Available online at
Association of the Chemical Engineers of Serbia *AChE*
www.ache.org.rs/CICEQ

Chem. Ind. Chem. Eng. Q. 31 (2) 113–121 (2025) CI&CEQ

ÇETIN KADAKAL[1]
BILGE AKDENIZ[2]
AYTEN EKINCI[3]
LUZIANA HOXHA[4]
PINAR ŞENGÜN[1]

[1]Department of Food Engineering, Faculty of Engineering, University of Pamukkale, Kinikli-Denizli, Turkey

[2]Department of Food Engineering, Faculty of Engineering, University of Afyon Kocatepe, Erenler-Afyonkarahisar, Turkey

[3]Vocational School of Technical Sciences, University of Pamukkale, Kinikli-Denizli, Turkey

[4]Agricultural University of Tirana, Faculty of Biotechnology and Food, Str. Pajsi Vodica, Koder Kamez, Tirana, Albania

SCIENTIFIC PAPER

UDC 577.161.12:632:635.64:543:66

THE RELATIONSHIP BETWEEN ERGOSTEROL AND *ALTERNARIA* MYCOTOXINS IN TOMATOES WITH DIFFERENT SURFACE DECAYED PROPORTIONS

Article Highlights

- Ergosterol has the potential to be used as a quality parameter instead of Alternaria mycotoxins
- Correlation between ergosterol and Alternaria of TPU samples with different TSD proportions
- Depending on mold genera, Alternaria and ergosterol can be produced in TPO and TPU samples

Abstract

This study evaluates the relationship between ergosterol (ERG) and Alternaria mycotoxins (AOH, AME, TenA) concentrations in tomato samples with varying decay levels. Using Rio Grande tomatoes, decay levels ranged from 89% to 99%. Samples were categorized based on visible mold, processed into pulp, and evaluated for quality parameters such as soluble solids, pH, acidity, and color. HPLC determined ERG, TenA, AOH, and AME levels, providing data on standard curve linearity, detection limit, recovery, and precision. Correlations between decay proportions and toxin concentrations were analyzed to understand variable relationships and quality implications for the tomato industry. Results indicate significant (p<0.05) effects of decay levels on toxin concentrations, emphasizing the importance of these measures for tomato quality assessment. The strong correlations among parameters underscore their relevance for quality control in tomato processing. This study contributes valuable insights for future research in this domain.

Keywords: alternariol; alternariol monomethyl ether; decay; ergosterol; tenuazonic acid; tomatoes.

The presence of mold in processed foods is a clear indicator of non-ideal processing conditions and the use of raw materials that do not meet the required quality standards [1]. Fungi are known as organisms that produce many different secondary metabolites, and many of these metabolites are called mycotoxins. Mycotoxins play an important role in the pathogenicity of fungi and pose a serious threat to agricultural products [2]. However, many of these mycotoxins are known to have adverse effects on both animals and humans when consumed. Therefore, it is important to prevent unhealthy processing conditions and the use of low-quality raw materials in the food industry. Compliance with hygienic standards and quality controls during food production and processing can help prevent mycotoxins from entering the food chain

---

Correspondence: P. Şengün, Department of Food Engineering, Faculty of Engineering, University of Pamukkale, 20160 Kinikli-Denizli, Turkey.
E-mail: lhoxha@ubt.edu.al

Paper received: 27 June, 2023
Paper revised: 6 November, 2024
Paper accepted: 15 May, 2024

https://doi.org/10.2298/CICEQ230627019K

[3,4,5].

Alternaria mold species are widespread, in both semi-arid and humid lands. *Alternaria* mold can spread, both to adapt to environmental conditions and to easily infect plant hosts [3,6–8]. Many plants, including cereals, oilseeds, tomatoes, and citrus fruits, are susceptible to severe diseases caused by these fungi [9,10]. Tomatoes are easily infected by *Alternaria* species during and after harvest. As a result of these infections, black rot occurs on the fruits. This infection caused by *Alternaria* mold species causes significant problems in tomato production. Control and management of these pathogens are of great importance for tomato production and tomato products [11,12].

Alternaria mold species are common fungal genera that, under appropriate conditions produce several metabolites, such as mycotoxins. One of the most critical mycotoxins-producing species is *Alternaria alternata*. Researchers have stated that fruits and vegetables with soft peels, such as tomatoes are susceptible to the *A. alternata* invasion [13]. During the ripening phase, water can be found on the surface of the fruit from the dew, or excessive irrigation. Fungus spores sprouting, which can be found on the surface of the fruit, are due to the accumulation of water [14].

Contamination of food with *Alternaria* mycotoxins occurs as a result of *Alternaria* species infecting food crops and agricultural products. *Alternaria* fungi can cause lesions on plant leaves, stems, or fruit. Apart from this, *Alternaria* toxins are formed in humid and hot environments during the storage of agricultural products. Additionally, it can also pass into food when agricultural products are processed. Mycotoxins are released into food during the processing of infected tomatoes, especially in processed foods such as tomatoes or tomato products. It has been reported in studies that *Alternaria* mycotoxins were detected in grains and products produced from grains [15,16], feeds [17], milk and dairy products [18], nuts [19], oilseeds [20], vegetable oils [21] and fermented beverages [22].

To penetrate and grow in tomatoes, *A. alternata* needs a damaged or soft texture. Thus, during harvesting, the fungus can penetrate the tomato peel, caused by physiological disorders (spotty ripening, cracking, sunburn, yellow spot), injuries by insects, puncture injuries, or the calyxes mold growth associated with the scar [23]. For many *Alternaria* spp. that could contaminate tomatoes, the biggest concerns arise from *Alternaria* mycotoxins, which are produced by such species [9]. Several *Alternaria* mycotoxins that are detected in moldy tomatoes include alternariol monomethyl ether (AME), alternariol (AOH), tenuazonic acid (TenA), altertoxin (ATX), and altenuenes (ALT) [9], found even in tomato products with potentially adverse effects on human health [6–8]. The presence of TenA in tomato products may indicate that rotten tomatoes were used in the processing procedure [6]. So, to prevent mycotoxin contamination, damaged or mold-decayed tomatoes should not be used in the processing of tomato products [25].

Even in our daily consumption of fruits and vegetables, these mycotoxins may be considered toxic contaminants, as *Alternaria* mycotoxins can be produced naturally in them in case of infection [3]. Even in Europen Food Safety Authority's (EFSA) opinion [8] stated the need for defined performance criteria and certified reference materials for the analysis of *Alternaria* toxins in various foods and feeds. EFSA has been collecting information on *Alternaria* toxins in food and processed products for a long time. According to EFSA, tomatoes, and tomato products are also exposed to mycotoxins [26]. The co-occurrence of *Alternaria* toxins and metabolites in foods constitutes a problem and remains to be investigated, as well as stated in the International Regulations of Commercial Products [3]. This situation causes a number of difficulties in the trade of products coming from different geographies around the world as a part of international trade. Therefore, further investigation and control of the presence of these mycotoxins in foods is of critical importance both to protect consumer health and to make the food industry safer [27].

Ergosterol (ERG) (3β-hydroxy-5,7,22-ergostatriene) is a substance that forms the fungal cell wall and is widely found in all foods, especially tomatoes [28]. Ergosterol is a critical fungal sterol, the primary sterol in fungal membranes, and has a regulatory role in the selective permeability and location in the membrane. It is considered an essential component of a healthy fungal cell. Studies have shown that there is a positive correlation between mold growth, ERG levels, and subsequent toxin production. This is why the ERG has recently been recognized as an indicator for the determination of fungal growth. The detection of ERG presence is considered a significant quality parameter for the decision on the fungal growth levels in food [29–31]. Ergosterol is a part of mold membranes and is found in high levels in molds. In addition, it is a minor component of various plant and animal sterols. The sterol content in bacteria is insignificant. Because they constitute less than 0.01% of the dry weight and very little of it belongs to ergosterol. Ergosterol can also be found in the structure of yeasts, but molds are considered the primary producers due to their greater biosynthetic capacity compared to yeasts [32].

The presence of ergosterol is associated with the presence of molds in foods, but no specific conditions for ergosterol formation have been identified. However, it may be associated with conditions that cause mold growth. Some mold species, such as *Fusarium, Alternaria*, *Aspergillus, Penicillium*, and *Mucor*, have been reported to produce significant amounts of ergosterol [28]. Moreover, the presence of ergosterol is mainly associated with active biomass and not with total biomass. Marin *et al.* [33] also noticed the high correlation between ergosterol and colony diameter and emphasized the potential for use of both parameters. *A. flavus*, *B. fulva, B. nivea, F. oxsporum, M. plumbeus, P. commune* and *P. roqueforti* with the same colony diameter have also been reported to produce variable levels of ergosterol [34].

For identifying molds, the chemical and biochemical methods are based on the detection and quantification of some specific components, such as ERG, chitin, fungal volatiles, and adenosine triphosphate (ATP). For ERG analysis, the methods are based on direct saponification, hexane extraction, and quantification using TLC (Thin Layer Chromatography), LC (Liquid Chromatography), HPLC (High-Performance Liquid Chromatography), or spectrophotometric methods (UV, infrared) [8,29–31, 35–39]. There exists a relationship between Howard mold count (HMC)-ERG-mycotoxins depending on the decay proportion of figs, apples, nuts, and tomatoes [28], and depending on this relationship, ERG may be used as a microbiological fungal growth indicator. For this reason, various research studies are needed to examine the ERG-mycotoxin relationships in other foodstuffs and, to use ERG as an alternative to mycotoxin analysis as a microbiological quality parameter.

To the best of our knowledge, there is no published research study on the determination of the relationship between ERG and *Alternaria* mycotoxins in pulp and tomato paste obtained from tomatoes with different surface decay rates. The data obtained through this study can be considered an important indicator for the tomato processing industry in terms of product quality.

The objectives of this study are as follows;

1. To determine the contents of ERG and *Alternaria* mycotoxins (AOH, AME, TA) in tomato pulp (TPU) and tomato paste (TPO) samples obtained from tomatoes with different surface rot (25,50,75, and 100%).
2. To reveal the correlation between Ergosterol and *Alternaria* in TPU samples with different TSD ratios.

To investigate the potential of using ergosterol as a quality parameter instead of *Alternaria* mycotoxins.

MATERIAL AND METHODS

Tomato sampling and procedures

For this study, the Rio Grande variety, one of Turkey's most common industrial type tomato varieties, for tomato paste production, is obtained from the Honaz Tomato Paste Factory, located in Honaz district of Denizli province, Turkey. This factory has a daily capacity of 50 tons of tomato processing. The samples were taken from eight different batch productions. With an average value of 4 kg of tomatoes taken for each decay proportion from each production batch. Samples were immediately transported to the university laboratory and processed further into tomato pulp (TPU). Tomatoes were classified in percentage as having a 25, 50, 75, and 100% rotting rate, based on visibly rotten molds on their surface, before processing to TPU. Tomato surface decay (TSD) proportions were determined according to the method of Kadakal *et al.* [40].

The tomatoes were processed with a plant finisher (pilot-type Langsenkamp mfr., model 185S, Indianapolis, IN). Then, the inactivation of the pectolytic enzyme was achieved by heat treatment at 90°C for 3 minutes and then cooled to 25 °C in a cooling water circulating container [40]. After cooling, the samples were passed through a finisher with a series of three sieves, respectively equipped with 1.8, 0.71, and 0.5 mm mesh sizes. Separated pomace and pulp tomatoes samples using a finisher, and were kept at -20 °C until the final determinations.

Determination of some quality parameters: soluble solids, pH, titratable acidity, and color measurement

The soluble solids of TPU samples were determined by refractive index measurements as the mean of two parallels and expressed as Brix degree (°Bx) using a digital refractometer, model RFM 340 (Bellingham & Stanley Co., Atlanta, GA) [40–42].

The pH of TPU samples was measured with a pH meter, model WTW pH 537 (WTW Measurement System Inc., Fort Myers, FL). The titratable acidity (TA) of TPU samples was measured with the titrimetric method and expressed as citric acid g/L. The results are expressed as the mean of two parallel measurements [40,41,43].

The color of the TPU samples is measured as reflectance with a chroma meter, model Konica Minolta CR-300 (Minolta Co., Osaka, Japan). As color values are measured for three color components (Hunter L*, a*, b*). The food industry has widely adopted this effective system, Hunter L* a* b* color space, for measuring color differences. On the tristimulus coordinate system, the L* value indicates lightness (0 is black and 100 is white), the a* value indicates red (+), or green (-) color, and the b* value indicates yellow (+), or blue (-) color [44]. Results are calculated as the mean value of five parallel measurements.

Determination of ergosterol and *Alternaria* mycotoxins

The HPLC method was used to determine ERG in the samples according to Kadakal *et al.* [10]. ERG an analytical-grade reagent, in crystalline form, was obtained from Sigma (Sigma-Aldrich Chemie GmbH, Deisenhofen-Germany). To determine TenA, AOH, and AME, the HPLC method was used, according to Terminiello *et al.* [45]. Each of the standards for AOH (*Alternaria sp.),* AME (*Alternaria alternata* (*tenuis*), and TenA (*Alternaria alternata*) were obtained from Sigma (St. Louis MO, USA).

The chromatographic separation was performed with an Inertsil 100A ODS-3 reversed-phase column (4.6×150 mm, 5 µm BGB Analytik AG, Boeckten, Switzerland). A photodiode array detector (SPD-M10 Avp, Shimadzu, Kyoto, Japan) set at 282 nm, a Shimadzu LC-10AT-VP HPLC pump, and a column oven (CTO-10AS, Shimadzu) set at 25 °C. The sample (20 µl) was injected into the HPLC system with a syringe (Hamilton Co., Reno, NV). The LabSolutions software (Shimadzu) was used.

A recovery test was performed to determine the extraction efficiency of the method. For this purpose, different concentrations of ERG, TenA, AOH, and AME standards were added to TPU samples of known ERG, TenA, AOH, and AME concentrations. In Table 1, are given data on the linearity of the standard curve, limit of detection, recovery, and precision of the proposed method for the determination of ERG, TenA, and AME.

Table 1. Characteristics of the proposed method: the linearity of the calibration curve, limit of detection, recovery, and precision.

Alternaria Toxins and ERG	Linear range (µg/L)	R	R^2	Detection limit (µg /kg)	Recovery (%)	Precision
					Mean SD^b	R.S.D. (%)
TenA	5.0-30000	0.9994	99.71	2.2	92.86 ± 0.9	5.7
AOH	1.0-30000	0.9990	99.90	0.8	95.40 ± 1.0	4.1
AME	1.0-30000	0.9976	99.88	1.1	92.60 ± 1.1	2.34
ERG	1-25000	0.9999	99.93	1.0	94.50 ± 1.0	3.68

Mean SDb: Mean ± standard deviation. R.S.D: Relative standard deviation.

Statistical analysis

Statistical analysis of the data was performed using IBM SPSS statistical analysis software for Windows version 23.0 (IBM Corp. 2015). The analysis of variance (ANOVA) revealed a significant effect ($p<0.05$), and the data means are compared with the least significant difference (LSD) test. Furthermore, bivariate correlations revealing a significant effect ($p<0.05$ and $p<0.01$) were examined.

RESULTS AND DISCUSSION

The relationship between ERG and *Alternaria* mycotoxins (TenA, AOH, and AME) concentrations of TPO samples with different surface decay proportions

Table 2 shows ERG (mg/kg) and *Alternaria* mycotoxin (TenA, AOH, and AME) (µg/kg) data for TPO samples, produced with decay proportions of: 25, 50, 75, and 100%. In the moldy tomato samples were detected *Alternaria* mycotoxins, including AOH, AME, and TenA, and these are in accordance with the statements of Hasan [46]. Nizamlıoğlu [26] reported that there is a linear relationship between ergosterol and *Alternaria* toxins depending on the decay rate, and that ergosterol is correlated with the AOH and TenA concentration in tomato paste. ERG and *Alternaria* mycotoxins concentrations in the TPU samples were significantly ($p<0.05$) affected by surface decay proportions (SDP).

Table 2. The relationships of ERG and Alternaria mycotoxins concentrations in TPO samples, with different surface decay proportions.

TSD proportion (%)	ERG (mg/kg)^x	*Alternaria* Mycotoxins		
		TenA (µg/kg)^x	AOH (µg/kg)^x	AME(µg/kg)^x
0	nd^{a*}	nd^{a*}	nd^{a*}	nd^{a*}
25	0.4^b	340^b	426^b	120^b
50	3.54^c	2190^c	2582^c	1364^c
75	5.68^d	2980^{cd}	3620^d	2468^d
100	8.40^e	4270^d	5106^e	2500^d

nd: not detected. *Values within the column with different letters are statistically significant ($p<0.05$). ^{x}Mean values of ten determinations with two replicates.

There is a positive relationship between TSD proportions and ERG concentrations, as revealed by

HPLC analysis in TPO samples. A similar trend is observed even for *Alternaria* mycotoxins concentrations measured. With the raising of TSD proportions, reaching 100%, the ERG concentrations in TPO have been increased too, from an undetectable value to 8.40 mg/kg. Also, the same phenomena are observed for *Alternaria* mycotoxins (TenA, AOH, and AME), where from an undetected level till the TSD proportions reached 100%, such concentrations reached respectively 4270, 5106, and 2500 µg/kg. A limited number of studies have been conducted in the literature on the AME, AOH, and TA contents of tomato paste and tomato pulp. However, Ekinci et al., [29] similarly reported that Aflatoxin, patulin, and ergosterol contents in hazelnuts had a linear correlation with different degradation rates. In a study, high levels of AOH and TA (>50 mg/kg) have been reported in tomatoes showing typical rot due to *Alternaria* decay [47].

The relationship between ERG and *Alternaria* mycotoxins (TenA, AOH, and AME) concentrations in TPU samples, with different surface decay proportions

ERG and *Alternaria* mycotoxins concentrations in the TPU samples were significantly ($p<0.05$) affected by the SDP (Table 3). There is also a positive correlation between the ERG and *Alternaria* mycotoxins concentrations in TPU samples and the TSD proportions.

Table 3. Relationship between ERG and Alternaria mycotoxins (TenA, AOH, and AME) concentrations in TPU samples, with different surface decay proportions.

TSD proportions (%)	ERG (mg/kg)^x	*Alternaria* Mycotoxins TenA (µg/kg)^x	AOH (µg/kg)^x	AME(µg/kg)^x
0	0.12^{a*}	2^{a*}	3^{a*}	0^{a*}
25	3.82^b	1545^b	1780^b	682^b
50	12.23^c	16314^c	18912^c	9672^c
75	19.80^d	18356^d	22768^d	12230^d
100	30.54^e	21890^e	25789^e	14680^e

*Values within a column followed by the different letters are significant ($p<0.05$). ^{x} Values are the mean of ten determinations in two replicates.

The concentration of ERG in TPU, ranged from 0.12 mg/kg to a value of 30.54 mg/kg from sound to 100% TSD, while for the *Alternaria* mycotoxins (TenA, AOH, and AME), have reached 21890, 25789, and 14680 µg/kg concentrations from 2, 3 and 0 µg/kg. Fliszár-Nyúl *et al.* [48] reported that AOH ranged from 6.1 to 25 µg/kg in tomato products. It was similar to the results obtained in TPU samples obtained from tomatoes with a 0% TSD rate. In different studies conducted, the highest AOH and AME were reported in tomato purees, while the highest TenA was detected in tomato products [49]. Ergosterol has been used as a microbiological quality indicator in tomatoes and tomato products in recent years. It is reported that there is a limit value of 15 mg/kg for tomatoes and tomato products [28]. It is observed that TPU samples obtained from tomatoes with 75% and 100% TSD exceed the limit level of 15 mg/kg ergosterol. EFSA reports that the average value for TA is a threshold of toxicological concern of 1500 ng/kg bw/day. AME and AOH in tomatoes have been reported to cause weak acute toxic effects in mice at 400 mg/kg (body weight) [50].

The relationship between some quality parameters of the TPU samples, with different surface decay proportions

The quality parameters (Table 4) observed in TPU samples were pH, °Bx, TA, and Hunter Lab color values, which were prepared from sound at 25, 50, 75, and 100% TSD. As it is presented in Table 4, there is a slight increase ($p<0.05$) in pH and TA values of TPU samples produced using sound, 25, 50, 75, and 100% TSD.

The changes in the ERG and *Alternaria* mycotoxins (TenA, AOH, and AME) concentrations in TPU and TPO samples, depending on different TSD proportions

The changes in the ERG and *Alternaria* mycotoxins (TenA, AOH, and AME) concentrations in TPU and TPO samples, obtained from different TSD proportions, are expressed by trendlines and the coefficient of determination (R^2), which are displayed in Fig. 1 and Fig. 2, respectively.

Table 4. Some quality parameters of the TPU samples, prepared from sound and 25, 50, 75, and 100% TSD.

TSD proportions (%)	pH^x	TA (g/L)^x	ºBx^x	Hunter L^x	a^x	b^x
0	4.20^{a*}	0.368^{a*}	4.88^{a*}	27.42^{a*}	13.56^{a*}	8.22^{a*}
25	4.37^b	0.352^b	5,15^b	27.78^a	13.50^a	8.18^a
50	4.35^b	0.364^a	5.32^c	29.42^b	13.48^a	8.60^b
75	4.35^b	0.375^c	5,16^b	30.26^c	13.60^a	8.90^{cd}
100	4.30^c	0.384^d	4.90^a	31.56^d	13.98^b	9.141^d

* Values within the column with different letters are statistically significant ($p<0.05$). ^{x} Average of ten determinations with two replicates.

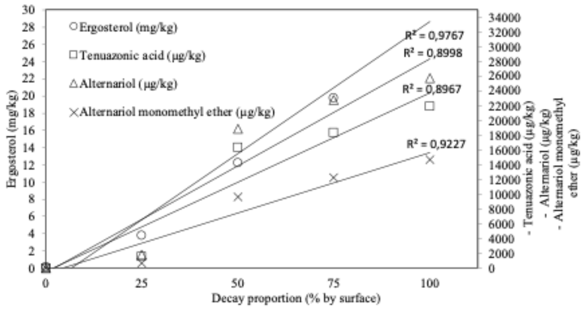

Figure 1. Changes in the concentrations of ERG and Alternaria mycotoxins (TenA, AOH, and AME) of TPU samples with different TSD proportions, expressed by the trendlines and the coefficient of determination (R^2).

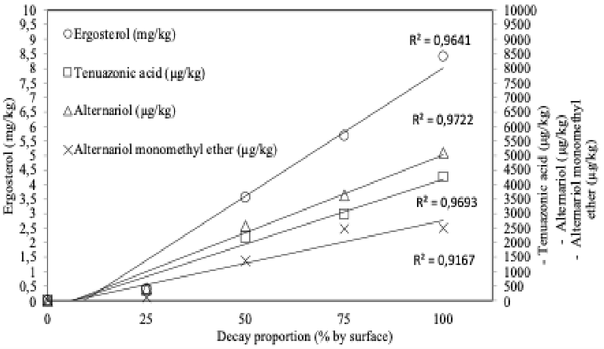

Figure 2. Changes in the concentrations of ERG and Alternaria mycotoxins (TenA, AOH, and AME) in TPO samples, with different TSD proportions, expressed by trendlines and the coefficient of determination (R^2).

It is noted that the amounts of ERG and *Alternaria* mycotoxins (TenA, AOH, and AME) in TPO samples are lower than in TPU samples. The data obtained at different TSD proportions reveal that these substances are transferred more during tomato processing in the TPU samples compared to the TPO samples. Furthermore, this transfer has shown an increasing trend, depending on the proportion of TSD.

The changes in the concentrations of *Alternaria* mycotoxins (TenA, AOH, and AME) depending on ERG concentrations in TPU and TPO samples

The changes in the concentrations of *Alternaria* mycotoxins (TenA, AOH, and AME) depending on ERG concentrations in TPU and TPO samples are displayed in Figures 3 and 4. They are expressed by trendlines and coefficient of determination (R^2) values.

The correlations and significance levels between the TSD proportions, the ERG concentration, the *Alternaria* mycotoxins concentrations, and some quality parameters of TPU and TPO samples

In this study, the correlation method is used to examine the relationship status between variables and to determine how the other variable explains many variations within one variable. As shown in Figures 1–4, the coefficient of determination value is calculated from the correlation value. Table 5 presents the computed data for correlations between the TSD proportions, the ERG concentration, and the *Alternaria* mycotoxins (TenA, AOH, and AME) concentrations and some quality parameters (such as pH, TA, °Bx, and Hunter L*, a*, b* color values) for TPU and TPO samples and the significance levels. Results show that between all variables a positive relationship exists. The following results emerge according to the coefficient of determination of variables.

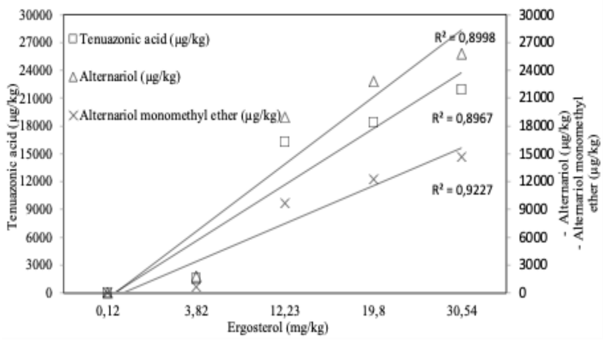

Figure 3. The changes in the concentrations of Alternaria mycotoxins (TenA, AOH, and AME) with different ERG concentrations in TPU samples, expressed by trendlines and the coefficient of determination (R^2).

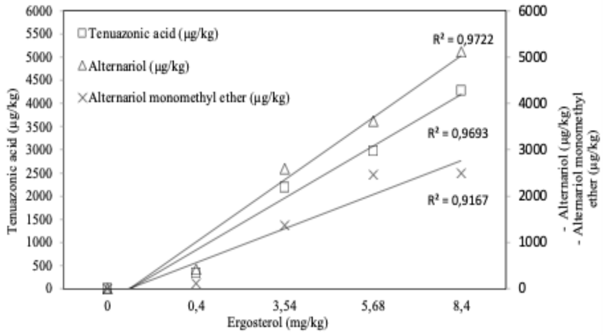

Figure 4. Changes in the concentrations of Alternaria mycotoxins (TenA, AOH, and AME) with different ERG concentrations of TPO samples are given by trend lines, and the coefficient of determination (R^2).

The correlation of the TSD proportions between ERG concentration in TPU, and TPO samples has no significant effects on the pH, TA, °Bx, Hunter L*, and a* color values. These findings are consistent with those of Kadakal *et al.* [40] study, except for Hunter b* color values, for which the significances are at the 0.01 level. The variations within TSD proportions in the TPU samples are explained by 93.3% for Hunter b* color values. The variations within ERG concentration in the TPU and TPO samples for Hunter b* color values are explained, respectively, by 96.6% and 99.0%.

The correlations of the TSD proportions are significant at the 0.01 level with ERG concentration, and AME is significant at the 0.05 level with TenA and

AOH concentration in TPU samples. Variations within TSD proportions are explained by 97.6% for the concentration of ERG, and by 89.7% of TenA, 90.1% for AOH, and 92.4% of AME in TPU samples. The relationship between TSD proportions is significant with concentrations of ERG, TenA, and AOH at the 0.01 level, and AME at the 0.05 level in TPO samples. ERG concentration explains 96.4% of the changes in TSD rates. In TPO samples, 97.0% of TenA is accounted for by 97.2% of AOH and 91.6% of AME concentration. Graselli *et al.* [51] stated essential correlations between ERG concentration and TSD.

It is noted that the concentrations of ERG and *Alternaria* mycotoxins in the TPU samples are related at the 0.05 significance level. The concentrations of 87.2% TenA, 87.2% AOH, and 91.0% AME in TPU samples are explained by the changes in ERG concentration in TPU. The concentrations of ERG and *Alternaria* mycotoxins in the TPO are related too. The relationship between the ERG concentration in the TPU samples is significant at the 0.01 level with TenA, and AOH, and at the 0.05 level with the AME concentration in TPO. Variations in ERG concentration of TPU samples are explained by 99.2% of ERG, 98.0% of TenA, 98.2% of AOH, and 89.9% of AME in TPO samples. In the TPO samples, the concentrations of ERG and *Alternaria* mycotoxins are related at the 0.01 significance level. The variations within ERG concentration are explained, respectively, by 99.2% of TenA concentration, 99.4% of AOH concentration, and 92.9% of AME concentration in the TPO samples. Nizamlıoğlu [26], investigated the relationship between ergosterol and three important mycotoxins (alternariol, alternariol monomethyl ether, and tenuazonic acid) in tomato paste and tomato juice. The results revealed that AOH and TA toxins were associated with ergosterol in tomato paste and tomato juice.

Table 5. Correlations and significance levels between the TSD proportions, the concentrations of ERG and Alternaria mycotoxins, and some quality parameters of TPU and TPO samples.

		TPU										TPO			
		pH	TA	ºBx	Hunter L	Hunter a	Hunter b	ERG	TenA	AOH	AME	ERG	TenA	AOH	AME
TSD (%)	R	0.414	0.725	0.042	-0.352	0.726	0.966**	0.988**	0.947*	0.949*	0.961**	0.982**	0.985**	0.986**	0.957*
	p	0.489	0.166	0.946	0.561	0.165	0.007	0.002	0.015	0.014	0.009	0.003	0.002	0.002	0.010
	R^2	0.171	0.526	0.002	0.124	0.527	0.933	0.976	0.897	0.901	0.924	0.964	0.970	0.972	0.916
TPU ERG	R	0.274	0.810	-0.094	-0.430	0.810	0.983**		0.934*	0.934*	0.954*	0.996**	0.990**	0.991**	0.948*
	p	0.655	0.097	0.881	0.470	0.096	0.003		0.020	0.020	0.012	0.000	0.001	0.001	0.014
	R^2	0.075	0.656	0.009	0.185	0.656	0.966		0.872	0.872	0.910	0.992	0.980	0.982	0.899
TPO ERG	R	0.242	0.837	-0.081	-0.503	0.788	0.995**						0.996**	0.997**	0.964**
	p	0.695	0.077	0.897	0.388	0.113	0.000						0.000	0.000	0.008
	R^2	0.059	0.701	0.007	0.253	0.622	0.990						0.992	0.994	0.929

R: correlation; R^2: coefficient of determination; p: significance; °Bx: Brix; TA: Titratable acidity. **Correlation is significant at the 0.01 level (2-tailed). *Correlation is significant at the 0.05 level (2-tailed).

CONCLUSION

This study examines ERG and Alternaria mycotoxin concentrations in TPO and TPU samples with varying decay proportions and TSD levels. Alternaria mycotoxins (AOH, AME, TenA) were detected in moldy tomato samples, aligning with previous findings. SDP significantly impacted ERG and Alternaria mycotoxin concentrations in TPU samples ($p<0.05$). HPLC analysis revealed a positive correlation between TSD proportions and ERG concentrations in TPO samples, similarly observed for Alternaria mycotoxins. As TSD proportions increased to 100%, ERG and Alternaria mycotoxin concentrations in TPO rose. Notably, concentrations were lower in TPO due to high heat treatment during tomato paste production. Transfer of substances during tomato processing was higher in TPU samples, increasing with TSD proportions. Positive correlations existed among TSD proportions, ERG, and Alternaria mycotoxin concentrations, as well as quality parameters (pH, TA, °Bx, Hunter L*, a*, b* color values) in both sample types. These findings support EFSA's need for defining performance criteria for Alternaria toxin analysis in foods and feeds. Strong correlations suggest these parameters could serve as quality indicators for defect evaluation in the tomato processing industry, warranting further research.

ACKNOWLEDGMENT

The authors would like to acknowledge the Honaz Tomato Paste Factory, for funding this research and providing the samples.

REFERENCES

[1] S. Dagnas, J.M Membré, J. Food Prot. 76(3) (2013) 538–551. https://doi.org/10.4315/0362-028X.JFP-12-349.

[2] J.L. Richard, Int. J. Food Microbiol. 119(1–2) (2007) 3–10.

https://doi.org/10.1016/j.ijfoodmicro.2007.07.019

[3] R. Barkai-Golan, in Mycotoxins in fruits and vegetables, R. Barkai-Golan, N. Paster Ed., Elsevier Inc, Amsterdam (2008) 185–204. https://doi.org/10.1016/B978-0-12-374126-4.X0001-0.

[4] R.A. Marc, in Mycotoxins and Food Safety-Recent Advances, R.A. Marci Ed., IntechOpen, Romania (2022) p. 149. https://doi.org/10.5772/intechopen.95720.

[5] J.I Pitt, M.H. Taniwaki, M.B. Cole, Food Control, 32(1) (2013) 205–215. https://doi.org/10.1016/j.foodcont.2012.11.023.

[6] S.D. Motta, L.M. Valente-Soares, Food Addit. Contam. 18(7) (2001) 630–634. https://doi.org/10.1080/02652030117707.

[7] V.E.F. Pinto, A. Patriarca, in Mycotoxigenic Fungi: Methods and Protocols, M. Antonio, S. Antonio Ed., Humana Press, New Jersey (2017) p. 394. https://doi.org/10.1007/978-1-4939-6707-0_1.

[8] EFSA, EFSA on Contaminants in the Food Chain, EFSA J. 9 (10) (2011) 2407. https://doi.org/10.2903/j.efsa.2011.2407.

[9] L.S. Jackson, F. Al-Taher, in Mycotoxins in fruits and vegetables, R. Barkai-Golan, N. Paster Ed., Elsevier Inc. Amsterdam (2008) 75–104. https://doi.org/10.1016/B978-0-12-374126-4.X0001-0.

[10] L. Escrivá, S. Oueslati, G. Font, L. Manyes, J. Food Qual. 32(1) (2017) 205–215. https://doi.org/10.1016/j.foodcont.2012.11.023.

[11] M. Solfrizzo, Curr. Opin. Food Sci. 17 (2017) 57–61. https://doi.org/10.1016/j.cofs.2017.09.012.

[12] Y. Ackermann, V. Curtui, R. Dietrich, M. Gross, H. Latif, E. Märtlbauer, E. Usleber, J. Agric. Food Chem. 59(12) (2011) 6360–6368. https://doi.org/10.1021/jf201516f.

[13] J. Noser, P. Schneider, M. Rother, H. Schmutz, Mycotoxin Res. 27(4) (2011) 265–271. https://doi.org/10.1007/s12550-011-0103-x.

[14] N. Jiand, Z. Li, L. Wang, H. Li, X. Zhu, X. Feng, M. Wang, Int. J. Food. Microbiol. 311 (2019) 108333. https://doi.org/10.1016/j.ijfoodmicro.2019.108333.

[15] V. Ostry, World Mycotoxin J. 1(2) (2008) 175–188. https://doi.org/10.3920/WMJ2008.x013.

[16] C. Juan, L. Covarelli, G. Beccari, V. Colasante, J. Mañes, Food Control, 62 (2016) 322–329. https://doi.org/10.1016/j.foodcont.2015.10.032.

[17] K. Sivagnanam, E. Komatsu, C. Rampitsch, H. Perreault, T. Gräfenhan, J. Sci. Food Agric. 97(1) (2017) 357–361. https://doi.org/10.1002/jsfa.7703.

[18] M. Zachariasova, Z. Dzuman, Z. Veprikova, K. Hojkova, M. Jiru, M. Vaclavikova, A. Zachariasova, M. Pospichalova, M. Florian, J. Hajslova, Anim. Feed Sci. Technol. 193 (2014) 124–140. https://doi.org/10.1016/j.anifeedsci.2014.02.007.

[19] W. Jia, X. Chu, Y. Ling, J. Huang, J. Chang, J. Chromatogr. A. 1345 (2014) 107–114. https://doi.org/10.1016/j.chroma.2014.04.021.

[20] W.A. Abia, B. Warth, M. Sulyok, R. Kriska, A.N. Tchana, P.B. Njobeh, M.F. Dutton, P.F. Moundipa, Food Control, 31(2) (2013) 438–453. https://doi.org/10.1016/j.foodcont.2012.10.006.

[21] P. López, D. Venema, T. Rijk, A. Kok, J.M. Scholten, H.G.J. Mol, M. Nijs, Food Control, 60 (2016) 196–204. https://doi.org/10.1016/j.foodcont.2015.07.032.

[22] S. Hickert, M. Bergmann, S. Ersen, B. Cramer, H.U. Humpf, Mycotoxin Res. 32(1) (2016) 7–18. https://doi.org/10.1007/s12550-015-0233-7.

[23] V.M. Scussel, J.M. Scholten, P.M. Rensen, M.C. Spanjer, B.N.E. Giordano, G.D. Savi, Int. J. Food Sci. Technol. 48(1) (2013) 96–102. https://doi.org/10.1111/j.1365-2621.2012.03163.x.

[24] A. Logrieco, A. Moretti, M. Solfrizzo, World Mycotoxin J. 2(2) (2009) 129–140. https://doi.org/10.3920/WMJ2009.1145.

[25] M. Meena, A. Zehra, P. Swapnil, M.K. Dubey, C.B. Patel, R.S. Upadhyay, Arch. Phytopathol. Plant Prot. 50(7–8) (2017) 317–329. https://doi.org/10.1080/03235408.2017.1312769.

[26] N.M. Nizamlıoğlu, J. Food Process. Preserv. 46 (11) (2022) e16937. https://doi.org/10.1111/jfpp.16937.

[27] M. Eskola, A. Altieri, J.J.W.M.J. Galobart, World Mycotoxin J. 11(2) (2018) 277–289. https://doi.org/10.3920/WMJ2017.2270.

[28] Ç. Kadakal, T.K. Tepe, Food Rev. Int. 35 (2) (2019) 155–165. https://doi.org/10.1080/87559129.2018.1482495.

[29] R. Ekinci, Ç. Kadakal, M. Otağ, J. Food Prot. 77 (3) (2014) 499–503. https://doi.org/10.4315/0362-028X.JFP-13-215.

[30] Ç. Kadakal, PhD Thesis, Ankara University, Institute of Science, Ankara, (2003) Turkey.

[31] Ç. Kadakal, N. Artık, Crit. Rev. Food Sci. Nutr. 44 (5) (2004) 349–351. https://doi.org/10.1080/10408690490489233.

[32] Ç. Kadakal, S. Nas, R. Ekinci, Food Chem. 90 (2005) 95–100. https://doi.org/10.1016/j.foodchem.2004.03.030.

[33] S. Marin, D. Cuevas, A.J. Ramos, V. Sanchis, Int. J. Food Microbiol. 121 (2008) 139–149. https://doi.org/10.1016/j.ijfoodmicro.2007.08.030.

[34] M.H. Taniwaki, A.D. Hocking, J.I. Pitt, G.H. Fleet, Int. J. Food Microbiol. 68 (2001) 125–133. https://doi.org/10.1016/S0168-1605(01)00487-1.

[35] S. Bermingham, L. Maltby, R.C. Cooke, Mycol. Res. 99 (1995) 479–484. https://doi.org/10.1016/S0953-7562(09)80650-3.

[36] H. Gourama, L.B. Bullerman, J. Food Prot. 558 12 (1995) 1395–1404. https://doi.org/10.4315/0362-028X-58.12.1395.

[37] Ç. Kadakal, S. Nas, R. Ekinci, Food Chem. 90 (2005) 95–100. https://doi.org/10.1016/j.foodchem.2004.03.030.

[38] Ç. Kadakal, M.N. Nizamlıoğlu, T.K. Tepe, S. Arısoy, B. Tepe. H.S. Batu, Turk. J. Agric. Food Sci. Tech. 8 (4) (2020). https://doi.org/10.24925/turjaf.v8i4.895-900.3071.

[39] M.R. Zill, J.E. Ehgelhardt, P.R. Wallnofer, Zeitschrift fur Lebensmittel-untersuchung und -forschung, 15 (1988) 20–22. https://doi.org/10.1007/bf01043094.

[40] Ç. Kadakal, Ş. Taği, N. Artık, J. Food Qual. 27 (4) (2004) 255–263. https://doi.org/10.1111/j.1745-4557.2004.00631.x.

[41] AOAC, Methods, Assoc. Off. Anal. Chem, 15th Ed., Arlington (1990) p. 910. ISBN 0-935584-40.

https://law.resource.org/pub/us/cfr/ibr/002/aoac.methods.1.1990.pdf.

[42] L.J. Mauer, R.L. Bradley, in Food Analysis, S.S. Nielsen Ed., Springer, New York (2017) 257–286. https://doi.org/10.1007/978-3-319-45776-5_15.

[43] C. Tyl, G.D. Sadler, in Food Analysis, S.S. Nielsen Ed., Springer, New York (2017) 389–406. https://doi.org/10.1007/978-3-319-45776-5_22.

[44] R.E. Wrolstad, D.E. Smith, in Food Analysis, S.S. Nielsen Ed., Springer, New York (2017) 545–555. https://doi.org/10.1007/978-3-319-45776-5_31.

[45] L. Terminiello, A. Patriarca, G. Pose, V.F. Pinto, Mycol. Res. 22 (4) (2006) 236–240. https://doi.org/10.1007/BF02946748.

[46] H.A. Hasan, Acta Microbiol. Immunol. Hung. 43 (2–3) (1996) 125–133. https://doi.org/10.1007/BF01103101.

[47] J. Walravens, H. Mikula, M. Rychlik, S. Asam, T. Devos, E.E. Njumbe, D.D. Mavungu, J. Jacxsens, L. Van, A. Landschoot, L. Vanhaecke, S. Saeger, J. Agric. Food Chem. 64(24) (2016) 5101–5109. https://doi.org/10.1021/acs.jafc.6b01029.

[48] E. Fliszár-Nyúl, Á. Szabó, L. Szente, M. Poór, J. Mol. Liq. 319 (2020) 114180. https://doi.org/10.1016/j.molliq.2020.114180.

[49] J.D. Ioi, PhD Thesis, The University of Guelph, Department of Food Science, Ontario, (2017) Canada.

[50] S.D. Motta, L.M.V. Soares, Braz. J. Microbiol. 31(4) (2000) 315–320. https://doi.org/10.1590/S1517-83822000000400015.

[51] C. Graselli, C. Leoni, C. Sandei, G. Mori, Ind. Conserve, 68 (1993) 1–10. http://pascal-francis.inist.fr/vibad/index.php?action=getRecordDetail&idt=4859569.

ÇETIN KADAKAL[1]
BILGE AKDENIZ[2]
AYTEN EKINCI[3]
LUZIANA HOXHA[4]
PINAR ŞENGÜN[1]

[1]Department of Food Engineering, Faculty of Engineering, University of Pamukkale, Kinikli-Denizli, Turkey

[2]Department of Food Engineering, Faculty of Engineering, University of Afyon Kocatepe, Erenler-Afyonkarahisar, Turkey

[3]Vocational School of Technical Sciences, University of Pamukkale, Kinikli-Denizli, Turkey

[4]Agricultural University of Tirana, Faculty of Biotechnology and Food, Str. Pajsi Vodica, Koder Kamez, Tirana, Albania

NAUČNI RAD

ODNOS IZMEĐU ERGOSTEROLA I *Alternaria* MIKOTOKSINA U PARADAJZU SA RAZLIČITIM POVRŠINSKIM PROPORCIJAMA

U ovom radu je istraživan odnos između koncentracija ergosterola (ERG) i mikotoksina alternarije (AOH, AME, TenA) u uzorcima paradajza sa različitim nivoima raspadanja. Koristeći paradajz Rio Grande, nivoi truljenja su se kretali od 89% do 99%. Uzorci su kategorisani na osnovu vidljive buđi, prerađeni u pulpu, pa su procenjeni parametri kvaliteta, kao što su rastvorljive čvrste materije, pH, kiselost i boja. HPLC-om su određeni nivoi ERG, TenA, AOH i AME korišćenjem standardne prave i definisanjem vrednosti granica detekcije, recovery i preciznosti. Analizirane su korelacije između stepena raspadanja i koncentracija toksina, da bi se razumeli promenljivi odnosi i implikacije kvaliteta za industriju paradajza. Rezultati ukazuju na značajne (p<0,05) uticaje nivoa raspadanja na koncentraciju toksina, što naglašava njihov značaj ovih za procenu kvaliteta paradajza. Jake korelacije među parametrima naglašavaju njihovu relevantnost za kontrolu kvaliteta u preradi paradajza. Ovaj rad doprinosi dragocenim uvidima za buduća istraživanja u ovoj oblasti.

Ključne reči: alternariol; alternariol monometil etar; raspadanje; ergosterol, tenuazonska kiselina; paradajz.

CI&CEQ
Chemical Industry & Chemical Engineering Quarterly

Available online at
Association of the Chemical Engineers of Serbia *AChE*
www.ache.org.rs/CICEQ

Chem. Ind. Chem. Eng. Q. 31 (2) 123–130 (2025) CI&CEQ

VENUGOPAL PALANISWAMY[1]
ANUSHA PEYYALA[2]
PRABHU PARAMASIVAM[3]
ITHA VEERANJANEYULU[4]

[1]Department of Mechanical Engineering, Muthayammal College of Engineering, Rasipuram, Namakkal (Dt), Tamil Nadu, India

[2]Department of Mechanical Engineering, P V P Siddhartha Institute of Technology, Vijayawada.India

[3]Centre of Research Impact and Outcome, Chitkara University, Rajpura, Punjab, India

[4]Department of Mechanical Engineering, Aditya University, Surampalem, India

SCIENTIFIC PAPER

UDC 621.9:544.6

PERFORMANCE ANALYSIS OF ELECTROCHEMICAL MICROMACHINING USING SIMPLE ADDITIVE WEIGHTING, CRITERIA IMPORTANCE THROUGH INTERCRITERIA CORRELATION, AND ARTIFICIAL NEURAL NETWORK METHODS

Article Highlights

- An aluminum scrap metal matrix material is fabricated, and machinability studies are performed
- ECMM performance is analyzed using (SAW), (CRITIC) and (ANN) techniques
- The best results show high MRR and low OC at 28 g/lit $NaNO_3$+0.05M HNO_3, 10 V, and 80% duty cycle
- The weight values of the performance metrics obtained using the SAW method are 0.549 and 0.45
- The optimal output performance predicted by ANN is MRR of 0.520 µm/sec and OC of 23.8 µm

Abstract

Electrochemical micromachining (ECMM) finds application in various industries, especially in surface finishing processes in aerospace industries. In this research, the workpiece made from aluminum scrap metal matrix reinforced with alumina is subjected to wear, surface profile, and machinability studies. To analyze the ECMM performance, simple additive weighting (SAW) CRiteria Importance Through Intercriteria Correlation (CRITIC) and Artificial Neural Network (ANN) were used. The wear studies show that at high loads the height wear loss is less and frictional force is more. The L_{18} mixed orthogonal array experiments were conducted and analysis of experiments shows that the most crucial parameter values for high MRR and low OC are 28g/lit $NaNO_3$+0.05M HNO_3, 10 V, and 80% duty cycle. The weight values of the performance metrics obtained using the SAW method are 0.549 and 0.45. The optimal output performance predicted by ANN is MRR of 0.520 µm/sec and OC of 23.8 µm.

Keywords: mixed electrolyte; sodium nitrate; nitric acid; duty cycle; optimization; overcut.

Electrochemical micromachining (ECMM) is the key machining process for machining burr-free micro features on the components. The ECMM is applied in diverse fields, such as biomedical, aerospace, and automobile. In ECMM, the cathode is the tool electrode and the anode is the workpiece which is the one to be machined. The electrodes are bridged by the electrolyte and while applying the voltage the material removal takes place. The removal of material in the range of 0-999µm from the anode is denoted as micromachining. From a manufacturing industry perspective, productivity, quality, and cost will go in holding hands and hence optimizations of the machining process were performed by many researchers [1]. Ganesan *et al.* [2] have optimized the

---

Correspondence: V. Palaniswamy, Department of Mechanical Engineering, Muthayammal College of Engineering, Rasipuram, Namakkal (Dt), Tamil Nadu, India-637 408.
E-mail: venunaveen73@yahoo.com
Paper received: 20 February, 2024
Paper revised: 13 May, 2024
Paper accepted: 23 May, 2024

https://doi.org/10.2298/CICEQ240220020P

laser parameter on dimple accuracy using principal-component-analysis-coupled grey relational grade. The optimal factor setting is 15 kHz (frequency), 12 W (average power), and 1500 ns (pulse duration). Sivashankar *et al.* [3] have optimized the ECMM parameters for machining magnesium alloy using TOPSIS and artificial neural networks (ANN). They reported that for obtaining a high material removal rate (MRR) the optimal combination is 13 V machining voltage, 75% duty cycle, and 30 g/L electrolyte concentration. Debkalpa Goswami *et al.* [4] have comparatively studied the ECMM performance using a differential search algorithm, genetic algorithm, and desirability function approach and proved that the differential search algorithm is a suitable method as a global optimization tool. Geethapriyan *et al.* [5] have optimized the ECMM variables using grey relational analysis with the Taguchi method. Based on the experimental study, it is evident that micro-tool feed speed is the most significant factor for sodium chloride electrolyte, and voltage is a significant factor for sodium nitrate electrolyte. Prakash *et al.* [6] have optimized the ECMM parameters using response surface methodology and Teaching-Learning-Based Optimization algorithm. When the results are examined, they agree with the RSM result when a target surface roughness value of 0.4 μm is taken into consideration. This confirms that the TLBO algorithm is better than the RSM approach. Rajan *et al.* [7] have optimized the ECMM characteristics for machining metal matrix composites using the TOPSIS method. The study reveals that the sodium nitrate electrolyte of 35 g/L concentration, the machining voltage of 11 V, and the 70% duty cycle are the optimal combination for higher MRR and lesser OC. Senthilkumar *et al.* [8] used the non-dominated sorting genetic algorithm II to optimize the electrochemical machining settings. The optimal value of surface roughness is found to be 2.172 μm and the related MRR is 0.413 g/min. Chandrasekhar *et al.* [9] have optimized the ECMM factors using the Entropy-VIKOR method for micro-drilling of AA6061-TiB_2. The electrolyte concentration of 2 mol, applied voltage of 16 V, and current of 4 A of current is the optimal parameter combination to minimize the overcut, and delamination, and to maximize the MRR. Nagarajan *et al.* [10] compared different multi-criteria decision-making algorithms such as grey wolf, moth-flame, and particle swarm methods. The study showed that the grey wolf and moth-flame algorithm shows the same result for machining Monel 400 alloys with ECM. Using the CRiteria Importance Through Intercriteria Correlation (CRITIC) -AHP technique, Venugopal *et al.* [11] optimized the ECMM parameters and found that the electrolyte concentration is the key component influencing conicity. Maniraj *et al.* [12] have applied three different weight evaluation methods for optimizing the ECMM parameters with the VIKOR method. Out of three weight evaluation methods, the analytic hierarchy process is found to produce the best result in ECMM. Manivannan *et al.* [13] have established the relationship between the ECMM process variables and output performance namely machining rate and OC They reported that the established is more efficient and accurate. Kaliappan *et al.* [14] have optimized the ECMM factors on machining rate, radial overcut, and delamination factor. They used the entropy method to determine the weights of the output performance. The grey relational grade is used to optimize the multi-performance and reported that 80 V,20 gm/lit, 50% duty cycle, and 40 °C electrolyte temperature is the optimal combination for achieving the higher machining rate, lower radial overcut, and lower delamination factor in metal matrix composites. Rajan *et al.* [15] have used TOPSIS and principal component analysis to optimize the ECMM factors on aluminum boron carbide composites. They found that the electrolyte concentration of level 35 g/L, the voltage at 11 V, and the duty cycle at 70% were the optimal combination for the machining rate, the diametric overcut, and the delamination factor, moreover ANOVA analysis shows that the duty cycle is the most significant factor. It is apparent that research on ECMM and process optimization were performed worldwide and the application of the multi-criteria decision-making (MCDM) method, namely Simple additive weighting (SAW) combined CRITIC in ECMM is sparse. Moreover, the results are predicted with the help of the ANN model. Hence in this research Nitric acid mixed sodium nitrate electrolyte is used and a mixed L_{18} orthogonal array (OA) experimental plan is used for the conduct of the experiments. The factors considered are the type of electrolyte, concentration of electrolyte, voltage, and duty cycle on MRR and OC.

Wear and surface estimation

The wear studies were performed on the sample with a constant track radius. The different load levels of 10 N, 20 N, and 30 N were applied on the specimen at constant speed and time of 380 rpm, 5 minutes 30 seconds respectively. The test results show that for a 10 N load, the height loss wear is 52 μ and the frictional force generated is 3.9 N. On further increase in load to 20 N and 30 N for the same speed and time condition the height loss wear and frictional force were 44 μ and 7.9 N & 34 μ and 13.2 N respectively. It is evident from the wear results that at low loads, the height loss wear is greater and the frictional force is less. It is due to the fact the poor distribution of reinforcement increases the height wear loss. At high loads, the height wear loss is less, and the frictional force is higher. The amalgamation of reinforcement attributes for more frictional force. The wear-investigated sample surface roughness depth profile is shown in Figure 1, where the values of *R*z, *R*t, and *R*a are 24.5 µm, 55.4 µm, and 3.04 µm, respectively.

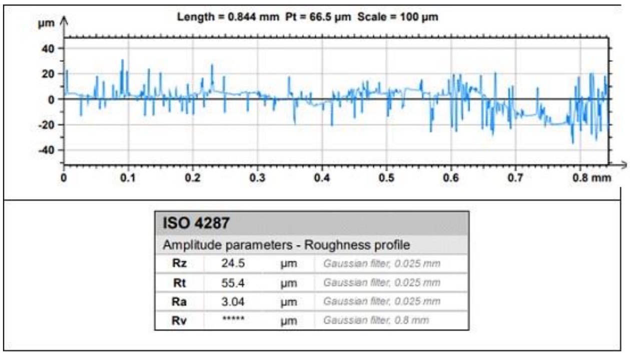

ISO 4287			
Amplitude parameters - Roughness profile			
Rz	24.5	µm	Gaussian filter, 0.025 mm
Rt	55.4	µm	Gaussian filter, 0.025 mm
Ra	3.04	µm	Gaussian filter, 0.025 mm
Rv	*****	µm	Gaussian filter, 0.8 mm

Figure 1. Surface roughness depth profile.

Experimental setup

The ECMM setup, which included a machining chamber, an electrolyte supply system, a pulsed power supply, and a tool advance mechanism, was used to conduct the experiments. The machining chamber housed the workpiece holder made up of Perspex material. The capacity of the machining chamber held 2 L of electrolyte. The electrolyte supply system consisted of a chemical pump, a filter to remove the debris, and an electrolyte supply pipe and nozzle. The pulse power supply unit with the specification of 0–30 V, current of 0–5 A, and frequency of 100 Hz was used for the experiments. The tool advance mechanism comprised the stepper motor, lead screw, and tool holder. The stepper motor was controlled by a microcontroller program. The tool holder was made up of a hollow copper tube and provided with a screw to fix the electrode. The tool electrode was isolated from the tool feeding arrangement. The workpiece was given with a positive power supply and the tool electrode was given with a negative power supply. The workpiece used for the experiment was the alloy wheel matrix composites of thickness of 300 µm. Figure 2 presents the optical microscope image of the workpiece sample which witnesses the presence of the silica. Figure 3 shows the EDAX image of the workpiece sample used for the machining. It shows the presence of aluminum, nickel, magnesium, carbon, oxide, chromium, iron, and silica. The tool electrode with a 600 µm diameter was coated with bonding liquid for insulation purposes to avoid stray current. The type, concentration, voltage, and duty cycle of the electrolyte were the parameters used in the studies. The performances were measured using MMR in µm/sec and OC in µm. The L_{18} mixed OA was considered and levels were identified based on past experiments and presented in Table 1. In this study, the total number of factors was four at three levels, hence the degrees of freedom was eight. Therefore, the OA selection should be more than eight, and hence, L_{18} was selected. Since there were two types of electrolytes, a mixed OA was considered for this study. The electrolyte sodium nitrate ($NaNO_3$) salt was mixed with 1 L of distilled water and stirred properly. Another type of mixed electrolyte, i.e., acidified $NaNO_3$ was prepared and used. To prepare 0.05 M of nitric acid, 3.20 mL of nitric acid was added to 1 L of distilled water, while $NaNO_3$ of varying grams was added to the mixed electrolyte [16].

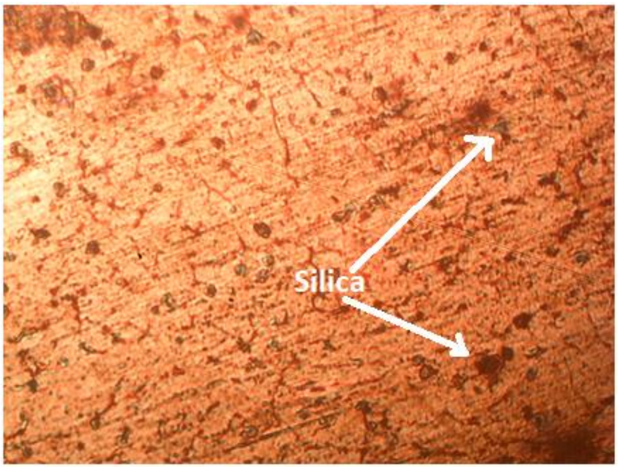

Figure 2. Optical image of the workpiece surface.

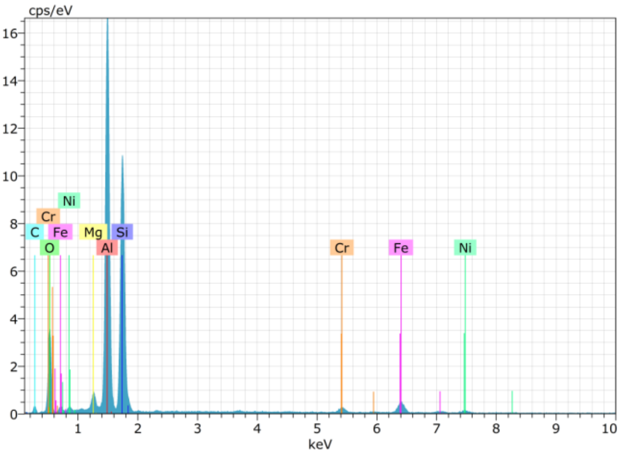

Figure 3. EDAX image of the sample workpiece.

RESULTS AND DISCUSSION

The MCDM approach uses the conflicting criteria to characterize the conflicting correlation between the decision criteria, or the alternatives that are taken into consideration in an MCDM problem. CRITIC method handles the multi-criteria problems more efficiently and at the same time it describes the weight and assists the decision maker in making a decision based on the importance of criteria, moreover it eliminates the non-

Table 1. L_{18} OA.

S.No	Electrolyte (*E*)	Electrolyte Concen-tration (*EC*), g/L	Voltage (*V*), V	Duty Cycle (*DC*), %	MRR, µm/sec	Overcut, µm
1	$NaNO_3$	20	8	70	0.208	140.17
2		20	9	80	0.250	86.98
3		20	10	90	0.217	60.49
4		24	8	70	0.156	90.67
5		24	9	80	0.217	206.23
6		24	10	90	0.238	222.02
7		28	8	80	0.278	119.49
8		28	9	90	0.263	176.77
9		28	10	70	0.208	131.25
10	$NaNO_3$+0.05M HNO_3	20	8	90	0.250	319.51
11		20	9	70	0.278	218.23
12		20	10	80	0.227	116.24
13		24	8	80	0.500	151.76
14		24	9	90	0.313	60.99
15		24	10	70	0.500	131.73
16		28	8	90	0.417	37.49
17		28	9	70	0.500	62.07
18		28	10	80	0.556	22.51

salient attributes. The multi-attribute process known as SAW is founded on the idea of a weighted summation. The method will attempt to find a weighted total of how well each alternative performed across all alternative criteria. The option with the highest score will be the best and will be suggested. The SAW method's fundamental idea, which is to determine the number of weighted performance ratings for each choice on all qualities, is useful. To use SAW, the decision matrix must be normalized to a scale that can be compared to all of the ratings of the available choices.

In this study, it was challenging to achieve lower OC and higher MRR at the same time. Greater MRR typically results in the acquisition of more reaction products and greater OC. When analyzing a contradictory correlation, the CRITIC approach uses the Pearson correlation coefficient, which ranges from -1 to 1 [17]. CRITIC was first envisioned by Diakoulaki *et al.* [18], this technique is based on the analysis of the assessment matrix to mine all the data included in the evaluation criteria. This method evaluates criterion weights by considering a criterion's standard deviation as well as its correlation with other criteria.

"*a*" is the number of alternatives, "*b*" denotes the number of criteria, and $A=[\phi_{ij}]_{a\times b}$, φ_{ij} is the performance measure of the i^th^ alternative with regard to the j^th^ criterion in an initial decision matrix.

Using the CRITIC approach, the initial decision matrix is normalized by using equation (1).

$$d_{ij}=\frac{\phi_{ij}-\phi_j^{\min}}{\phi_j^{\max^{\min}}} \quad (1)$$

where, $\phi_j^{\max}=\max\left(\varphi_{ij},i=1....,a\right)$

and $\phi_j^{\min}=\min\left(\varphi_{ij},i=1....,a\right)$.

The standard deviation of each criterion and its correlation with other criteria are taken into consideration when determining the weights assigned to them. Thus, it is possible to determine the weight of the j^th^ criterion w_j in the following way [11]:

$$\eta_j=\frac{w_j}{\sum_{i=1}^{m}w_i} \quad (2)$$

where w_j is the amount of information present in the j^{th} criterion and can be obtained as follows:

$$w_j=\sigma_j\sum_{i=1}^{m}\left(1-\rho_{ij}\right) \quad (3)$$

where is the correlation coefficient between the j^{th} and i^{th} criteria, and σ_j is the standard deviation of the j^{th} criterion.

Based on the weighted average, the SAW methodology is a simple multi-attribute decision-making method that was initially adopted by Churchman *et al.* [19]. The SAW method's steps are as follows:

- Create a decision matrix [X_{ij}] for different performance scenarios.
- Normalizing the value of i^{th} criterion for the j^{th} Alternative by using Eqs., (49) and (5):

$$\rho_{ij}=\frac{X_{ij}}{\max X_{ij}} \text{ if } j \text{ is a gain/MRR attribute} \quad (4)$$

$$\rho_{ij}=\frac{\min X_{ij}}{X_{ij}} \text{ if } j \text{ is a loss/OC attribute} \quad (5)$$

where ρ_{ij} is the normalized decision matrix.

Determine the SAW (S_i) value by using Eq. (6).

$$S_i=[\rho_{ij}][\eta_j] \quad (6)$$

Arrange the final results according to value, with the highest number being the best experimental combination for the highest performance metrics (MRR and OC). The normalized values for MRR and OC obtained using the CRITIC and SAW techniques are shown in Table 2. Using the normalized values obtained using CRITIC, the standard deviations for MRR and OC were computed, and they are, respectively, 0.3126 and 0.2566. Table 3 shows the correlation between the performance measures.

Table 2. Normalization of original values through CRITIC and SAW.

	Normalization - CRITIC		Normalization - SAW		S_i	Rank
Sl.No	MRR	OC	MRR	OC		
1	0.1304	0.6039	0.1476	0.2198	0.2781	16
2	0.2348	0.7829	0.1771	0.1364	0.3635	8
3	0.1531	0.8721	0.154	0.0948	0.3823	7
4	0	0.7705	0.1107	0.1422	0.2661	17
5	0.1531	0.3814	0.154	0.3234	0.2639	18
6	0.205	0.3282	0.1687	0.3481	0.2809	14
7	0.3043	0.6735	0.1968	0.1874	0.3593	9
8	0.2677	0.4806	0.1864	0.2772	0.3174	11
9	0.1304	0.6339	0.1476	0.2058	0.2831	13
10	0.2348	0	0.1771	0.501	0.2788	15
11	0.3043	0.341	0.1968	0.3422	0.3209	10
12	0.1779	0.6844	0.161	0.1823	0.3117	12
13	0.8609	0.5648	0.3542	0.2379	0.5609	5
14	0.3913	0.8705	0.2214	0.0956	0.4749	6
15	0.8609	0.6323	0.3542	0.2065	0.5710	4
16	0.6522	0.9496	0.2952	0.0588	0.6820	2
17	0.8609	0.8668	0.3542	0.0973	0.6573	3
18	1	1	0.3936	0.0353	0.9990	1

Table 3. Correlation between the performance measures.

Performance measures	MRR	OC	C_j	w_j
MRR	1	0.3683	-	-
OC	0.3683	1	-	-
MRR	0	0.63169	0.1975	0.5492
OC	0.63169	0	0.1621	0.4508

For MRR and OC, respectively, the weight values of the performance metrics obtained using Eqs. (4) and (5) are 0.549 and 0.45. The SAW method uses Eq. (6) to estimate the final S_i value by taking the computed weight values into account. The greatest value is ranked 1 and given the highest importance, with the remaining values being ranked in order of descent [20–21]. According to Table 2, the most crucial parameter values for high MRR and low OC are 28 g/L $NaNO_3$+0.05 M HNO_3, 10 V, and 80% duty cycle. The second-best set of parameters is 28 g/L $NaNO_3$+0.05M HNO_3, 8 V, and 90% duty cycle. It is evident from the optimized parameter combinations that acidified $NaNO_3$ is one of the factors that influence the output performance. Acidic electrolytes are utilized to improve the dissolution efficiency; nitric, hydrochloric, sulfuric, and perchloric acids are a few examples of acidic electrolytes. Since the ions and other reaction products are firmly dissolved in the electrolytic solution, there is a significant reduction in the inter-electrode gap. Additionally, this solves the clogging issue and enhances the machining efficacy in ECMM [22].

The SEM picture shown in Figure 4 was machined at 28 g/L $NaNO_3$+0.05 M HNO_3, 10 V, and 80% duty cycle, depicting a good circular micro-hole with an over-etched and corroded surface [23].

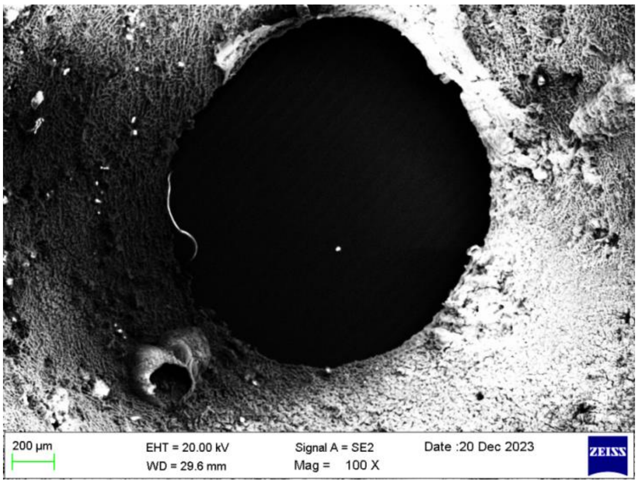

Figure 4. SEM picture of micro-hole.

ANN prediction

In recent research, the implementation of the advanced non-traditional method in optimization is highly required for accurate outcomes. Here ANN is implemented to predict the suitable inputs and outputs. Here developed ANN model will predict the accurate inputs and output parameters with the help of training and targets. MATLAB 15 software was utilized for architecture development. This architecture is developed with different layers as given in Figure 5. Here 4 inputs are used to carry out the experiments [24]. Hence ANN is developed to process 4 inputs with ten hidden layers. A hidden layer in ANN is used to process the input values while training. Output layers are generally predicting the processed output. For input and output processing, a random data revision type MATLAB inbuilt algorithm is used. ANN prediction consists of three important stages. Initially network development and followed by training. The final stage in ANN is output prediction [25]. Here all the experimental inputs are considered as training variables. For training, experimental outputs are considered target values. Totally 5000 iteration training is given to ANN and its parameters. Based on training and target variables, training is given with a total time limit of 1 minute and 23 seconds.

It is observed that the total ANN training has achieved 5000 iterations without any errors. The blue training line gradually reaches the target while training.

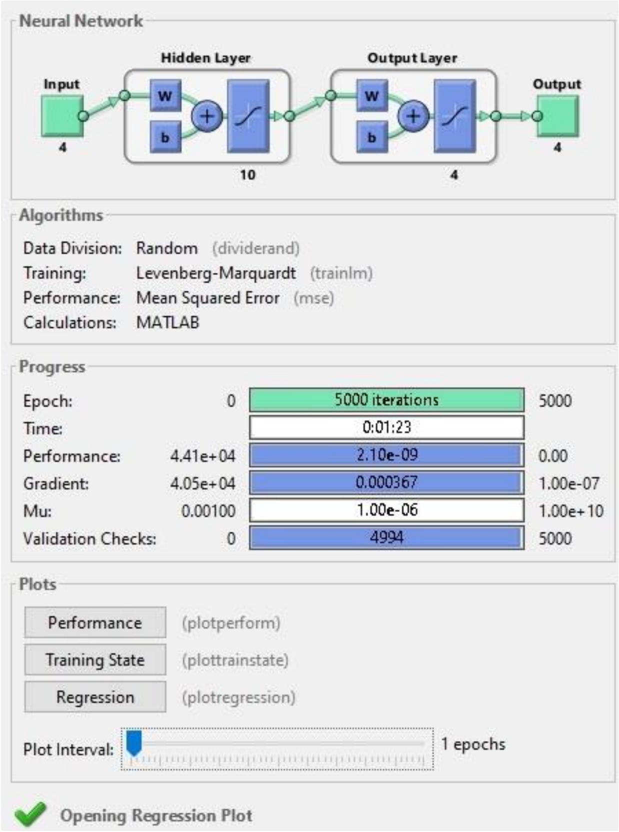

Algorithms

Data Division: Random (dividerand)
Training: Levenberg-Marquardt (trainlm)
Performance: Mean Squared Error (mse)
Calculations: MATLAB

Progress

Epoch:	0	5000 iterations	5000
Time:		0:01:23	
Performance:	4.41e+04	2.10e-09	0.00
Gradient:	4.05e+04	0.000367	1.00e-07
Mu:	0.00100	1.00e-06	1.00e+10
Validation Checks:	0	4994	5000

Performance (plotperform)
Training State (plottrainstate)
Regression (plotregression)
Plot Interval: 1 epochs

✓ Opening Regression Plot

Figure 5. Neural network with algorithm.

For better understanding, a narrow straight line in the gradient curve (Figure 6) reveals error-free training of ANN architecture. Totally 4994 iterations are verified by ANN which is 99.8% accuracy of developed architecture. As can be seen in Figure 6, it represents 99.9% of training with an overall performance of 97.9% [26-27]. With respect to training, ANN predicted time is 614 s of machining time with 0.520 MRR and 23.8 OC. ANN predictions present a similar trend to CRITIC and SAW. The predicted parameters and their levels are given in Table 4.

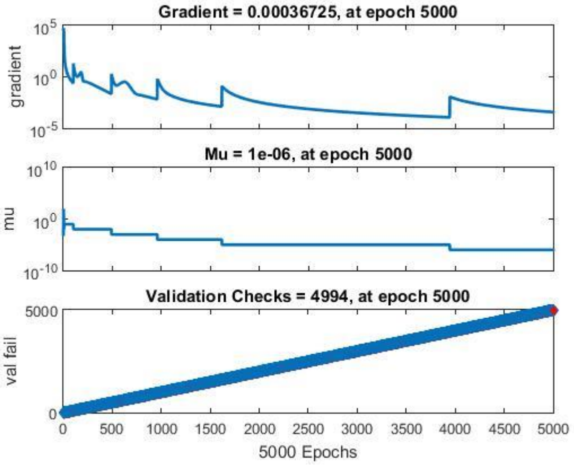

Figure 6. ANN gradient curve.

Table 4. Results of the ANN model.

Parameters	Optimal process parameters	
	CIRTIC and SAW	ANN Prediction
Levels	$E_2EC_3V_3D_2$	$E_2EC_3V_3D_2$
Time (min)	540	614
MRR (µm/s)	0.556	0.520
OC (µm)	22.51	23.8

CONCLUSION

1. A wear test was conducted on the fabricated metal matrix composites and on applying a 30 N load and a 380 rpm speed, the height loss wear was 34 µ, and the frictional force developed was 13.2 N.
2. The wear-investigated sample surface roughness depth profile showed the values of *Rz*, *Rt*, and *Ra* of 24.5 µm, 55.4 µm, and 3.04 µm, respectively.
3. The OA experiment was successfully conducted using $NaNO_3$ and $NaNO_3$ +HNO_3 electrolytes.
4. The most crucial parameter values for high MRR and low OC were 28 g/L $NaNO_3$+0.05M HNO_3, 10 V, and 80% duty cycle. The second-best set of parameters were 28 g/L $NaNO_3$+0.05M HNO_3, 8 V, and 90% duty cycle.
5. The performance measures acquired by the SAW approach had weight values of 0.549 and 0.45.
6. The optimal output performances predicted by ANN are MRR of 0.520 µm/s and OC of 23.8 µm. The expected values and the experimental values were reasonably close. Hence ANN was best suited for the ECMM performance prediction.

Based on ANN prediction, the best levels of parameters were 28 g/L of $NaNO_3$+0.05 M HNO_3 with 10 V and 80% duty cycle.

REFERENCES

[1] T.Masuzawa, CIRP Ann. 49 (2000) 473–488. https://doi.org/10.1016/S0007-8506(07)63451-9.

[2] S.K. Ganesan, T. Rajasekaran, J. Mech. Eng. 67 (2021) 525–533. https://doi.org/10.5545/sv-jme.2021.7246

[3] N. Sivashankar, R. Thanigaivelan, K.G. Saravanan, Bull. Chem. Soc. Ethiop.37 (2023)1263–1273. https://doi.org/10.4314/bcse.v37i5.17.

[4] D. Goswami, S. Chakraborty, Int. J. Ind. Eng. 5 (2014) 41–54. http://dx.doi.org/%2010.5267/j.ijiec.2013.08.003.

[5] T. Geethapriyan, K. Kalaichelvan, T. Muthuramalingam, Metall. Ital. 4 (2016) 13–19. https://www.aimnet.it/la_metallurgia_italiana/2016/aprile/Muthuramalingam.pdf.

[6] J. Prakash, S. Gopalakannan, Silicon 13 (2021) 409–432. https:// doi.org/ 10.1007/s12633-020-00434-0

[7] N. Rajan, M.N.S. Sri, P. Anusha, R. Thanigaivelan, S. Vijayakumar, Surf. Eng. Appl. Electrochem. 59 (2023) 719–727. https://doi.org/10.3103/S1068375523060157.

[8] C. Senthilkumar, G. Ganesan, R. Karthikeyan, Nonferrous Met. Soc. 21(2011) 2294–2300. https://doi.org/10.1016/S1003-6326(11)61010-8.

[9] S. Chandrasekhar, N.B.V. Prasad, Proc. Inst. Mech. Eng., Part B234 (2020) 1311–1322. https://doi.org/10.1177/0954405420911539.

[10] V. Nagarajan, A. Solaiyappan, S.K. Mahalingam, L. Nagarajan, S. Salunkhe, E.A Nasr, H. M.A.M. Hussein, Appl. Sci.12 (2022) 2793. https://doi.org/10.3390/app12062793.

[11] P. Venugopal, T.G. Arul, R. Thanigaivelan, Ionics 28 (2022) 4745–4753. https://doi.org/10.1007/s11581-022-04686-1.

[12] S. Maniraj, R. Thanigaivelan, K. Gunasekaran, K.G. Saravanan, Adv. Mater. Sci. Eng. 2023 (2023) 1366857. https://doi.org/10.1155/2023/1366857.

[13] R.Manivannan, T.Niranjan, S.Maniraj, R.Thanigaivelan, J-New Mat. Electr. Sys, 27 (1) (2024) 25–29. https://doi.org/10.14447/jnmes.v27i1.a04.

[14] S Kaliappan, P Pravin, KG Saravanan, Rajasekaran Thanigaivelan, High Temp. Mater. Process., 28(2) (2024) 33–43. https://doi.org/10.1615/HighTempMatProc.2023048114.

[15] N Rajan, M Naga Swapna Sri, P Anusha, R Thanigaivelan, S Vijayakumar, Surf. Eng. Appl. Electrochem. 59 (2023) 719–727. https://doi.org/10.3103/S1068375523060157.

[16] R. Thanigaivelan, R.M. Arunachalam, B. Karthikeyan, P. Loganathan, Procedia CIRP 6 (2013) 351–355. https://doi.org/10.1016/j.procir.2013.03.011.

[17] H. Taherdoost, J. Manage. Sci. 6 (2023) 21–24. https://doi.org/10.30564/jmser.v6i1.5400.

[18] D. Diakoulaki, G. Mavrotas, L. Papayannakis,Comput. Oper. Res. 22 (1995) 763–770. https://doi.org/10.1016/0305-0548(94)00059-H.

[19] C.W. Churchman, R.L.Ackoff, J. Oper. Res. Soc. Am. 2 (1954) 172–187. https://doi.org/10.1287/opre.2.2.172.

[20] S. Kunar, S. Karumuri, I.Veeranjaneyulu, G. Belachew, S.R. Medapati, Key Eng. Mater. 933 (2022) 107–115. https://doi.org/10.4028/p-6x55wh.

[21] S. Karumuri, B. Haldar, A. Pradeep, S.A.K. Karanam, M.N.S. Sri, P. Anusha,S. Vijayakumar, Int. J. Interact. Des. Manuf. (2023) https://doi.org/10.1007/s12008-023-01529-9.

[22] K. G. Saravanan, R. Prabu, A. R. Venkataramanan, E. T. Beyessa, Adv. Mater. Sci. Engi, 2021, http://dx.doi.org/10.1155/2021/1432300.

[23] V. Palaniswamy, K. Seeniappan, T. Rajasekaran, N.Lakshmaiya, Chem. Ind. Chem. Eng. Q. 29 (2023) 201–208. https://doi.org/10.2298/CICEQ220731027P.

[24] B.W.Min, J. Internet Things Converg. 9 (2023) 93–98. http://doi.org/10.20465/KIOTS.2023.9.3.061.

[25] S. Bellubbi, B. Mallick, A.S Hameed, P. Dutta, M.K. Sarkar, S.J. Nanjundaswamy, Adv. Manuf. 21(2022) 869–897. https://doi.org/10.1142/S0219686722500330.

[26] S.K. Tamang, P.D. Singh, B. Datta, J. Environ. Sci.6 (2020) 53–64. https://doi.org/10.22034/GJESM.2019.06.SI.06.

[27] M. Chandrasekaran, S. Tamang, J. Inst. Eng. (India): Ser. C98 (2017) 395–401. https://doi.org/10.1007/s40032-016-0276-3.

VENUGOPAL PALANISWAMY[1]
ANUSHA PEYYALA[2]
PRABHU PARAMASIVAM[3]
ITHA VEERANJANEYULU[4]

[1]Department of Mechanical Engineering, Muthayammal College of Engineering, Rasipuram, Namakkal (Dt), Tamil Nadu, India

[2]Department of Mechanical Engineering, P V P Siddhartha Institute of Technology, Vijayawada.India

[3]Centre of Research Impact and Outcome, Chitkara University, Rajpura, Punjab, India

[4]Department of Mechanical Engineering, Aditya University, Surampalem, India

NAUČNI RAD

ANALIZA PERFORMANSE ELEKTROHEMIJSKE MIKROMŠINSKE OBRADE KORIŠĆENJEM JEDNOSTAVNIH ADITIVNIH TEŽINA, VAŽNOSTI KRITERIJUMA METODAMA KORELACIJE MEĐUKRITERIJUMA I VEŠTAČKE NEURONSKE MREŽE

Elektrohemijska mikromašinska obrada (ECMM) nalazi primenu u različitim industrijama, posebno u procesima završne obrade površina u vazduhoplovnoj industriji. U ovom radu, radni komad napravljen od matrice starog aluminijumskog metala ojačanog glinicom je podvrgnut istraživanjima habanja, površinskog profila i obradivosti. Za analizu performansi ECMM-a, korišćene su jednostavne aditivne težine (SAV) važnosti kriterijuma kroz međukriterijumsku korelaciju (CRITIC) i veštačka neuronska mreža (ANN). Studije habanja pokazuju da je pri velikim opterećenjima gubitak habanja po visini manji, a sila trenja veća. Sprovedeni su eksperimenti sa mešovitim ortogonalnim nizom L_{18}*, koja je pokazala najvažnije vrednosti parametara za visok MRR i nizak OC: 28g/l* $NaNO_3$*+0,05 M* HNO_3*, 10 V i 80% radnog ciklusa. Vrednosti težine metrike performansi dobijene metodom SAV su 0,55 i 0,45. Optimalne izlazne performanse koje predviđa ANN je MRR od 0,52 µm/s i OC od 23,8 µm.*

Ključne reči: mešani elektrolit; natrijum-nitrat; azotna kiselina; radni ciklus; optimizacija; prekomerno sečenje.

CI&CEQ
Chemical Industry & Chemical Engineering Quarterly

Available online at
Association of the Chemical Engineers of Serbia *AChE*
www.ache.org.rs/CICEQ

Chem. Ind. Chem. Eng. Q. 31 (2) 131–138 (2025) CI&CEQ

JULIJA VOLMAJER VALH[1]
MATEJKA TUREL[2]
ANDREJ HOLOBAR[2]
MARJANA SIMONIČ[3]

[1]University of Maribor, Faculty of Mechanical Engineering, Institute of Engineering Materials and Design, Maribor, Slovenia

[2]ECHO Instruments d.o.o, Slovenske Konjice, Slovenia

[3]University of Maribor, Faculty of Chemistry and Chemical Engineering, Maribor, Slovenia

SCIENTIFIC PAPER

UDC 614.8:66.08:620:502.174.2

BIODEGRADATION OF PROTECTIVE MASKS (COVID-19) IN COMPOST AND AQUEOUS MEDIA

Article Highlights

- Self-made respirometer showed excellent performance characteristics
- Microcellulose reference material degrades at 58.4% in 75 days
- The linen/cotton mask degradation was at 67.1% in 75 days and is still increasing
- The hemp mask degrades at 59.6% in 75 days

Abstract

The study of biodegradation of facial masks made of natural and synthetic materials was performed. The experimental part was performed with a respirometer from the Slovenian manufacturer ECHO Instruments. We conducted a preliminary test to select the compost with the highest activity for further work. The rate of biodegradation of the materials was calculated based on measurements of the carbon dioxide produced in the reactors. The biodegradability results of the materials were verified using FTIR spectroscopy and microscope images. Masks made of linen and cotton particles performed the best biodegradation at 72%, while particles of masks made of polypropylene (PP) did not degrade. Since there are no studies on biodegradability in water, the second part of our study was to investigate the rate of degradation of the masks in wastewater. Based on the FTIR spectra obtained, the presence of new functional groups on the surface of the protective masks was confirmed as a result of the oxidation process. Humovit compost was chosen as the inoculum for the water medium. We determined the highest degree of biodegradation for the linen/cotton mask (67% in 75 days).

Keywords: protective masks; linen/cotton; Himalayan hemp; respirometry; FTIR.

During the COVID-19 pandemic, demand led to an unprecedented increase in the global production of disposable face masks made from polymeric materials [1]. The most commonly used material for the production of surgical masks is petroleum-based polypropylene (PP) [2]. Surgical (medical) masks consist of at least three layers [3]. The inner layer consists of an absorbent material that absorbs moisture from the user's breathing air. The middle layer consists of a nonwoven material that provides effective filtration. The outer layer is made of a non-woven waterproof material. Surgical masks are designed to prevent the ingress of larger droplets (> 100 µm) and help reduce the spread of saliva and exhaled air into the environment. The SARS-CoV-2 virus has a spherical shape with a diameter between 60 and 140 µm, which means that a surgical mask cannot fully protect the user from infection [4]. Due to the increasing plastic waste pollution worldwide and the accumulation of microplastics in ecosystems, we urgently need to seek alternative, more sustainable methods for waste disposal. One of the promising solutions is to replace masks made of plastic polymers with biodegradable and reusable materials [5]. The global problem of plastic accumulation in the environment encourages us to apply and develop more effective methods [6]. Over time, fragments of plastic pollution transform into

---

Correspondence: M. Simonič, University of Maribor, Faculty of Mechanical Engineering, Institute of Engineering Materials and Design, Smetanova 17, 2000 Maribor, Slovenia.
E-mail: marjana.simonic@um.si
Paper received: 21 September, 2023
Paper revised: 25 April, 2024
Paper accepted: 27 May, 2024

https://doi.org/10.2298/CICEQ230921021V

microplastics or nanoplastics [7]. Microplastics were also recently detected in hail that fell directly in Slovenia. It is the first case of its kind in the world and is definitely a cause for concern [8]. Researchers are currently focusing on acquiring knowledge in the field of aerobic and anaerobic biodegradation of (micro)plastics using microbial cultures and on the production of bioplastics [9].

Microorganisms belonging to the genus Pseudomonas are often the subject of research because they have a good ability to degrade hydrocarbons and hydrophobic polymers [10]. They found that the majority of naturally occurring isolated bacteria from the genus *Pseudomonas* is capable of at least partially degrading the most common representatives of synthetic polymers, such as polyethylene, polypropylene, polystyrene, and polyvinyl chloride. A novel consortium was studied for PP degradation [11]. The study provided evidence that thermophilic *Pseudomonas* spp., *Stenotrophomonas* spp., *Bacillus* spp., and *Paenibacillus* spp. Exhibited increased rates of low-density polyethylene LDPE and high-density polyethylene HDPE degradation when formulated as consortia of all four bacteria. The evaluation of respirometry-based control strategies for activated sludge processes was presented many years ago [12]. To date, a limited number of respirometric protocols is available in the scientific literature; however, most of them are related to long-term biodegradability evaluations (such as the measurement of biological oxygen demand BOD measurement). The advantages of using a respirometer are that no titration is required, the concentration of oxygen and/or carbon dioxide is continuously measured, and the simultaneous measurement of multiple samples to have the same experimental conditions for all samples throughout the experiment [13].

The biodegradation of commercial polyurethane formulations has been monitored by combining respirometry and Raman spectroscopy [14]. Respirometry tests on cheese showed a linear increase in oxygen consumption during respiration of polycaprolactone with α-tocopherol addition [15]. The respirometry results obtained support the potential of using oleaginous craft paper as a food packaging material [16].

Many factors, such as pH and temperature, as well as polymer properties (e.g., polarity, glass transition temperature, and morphology) influence the efficient degradation and breakdown of different mask materials under industrial composting conditions. Thus the aim of the article was the study of face mask biodegradation through model respirometry experiments. The study is divided into two sections: First, the polymeric material was degraded in compost; in the second section the polymeric material was degraded in aqueous media. Bio-based materials, such as gluten fiber, cellulose, polylactic acid, banana stem fiber, chitosan whiskers, and polyhydroxyalkanoates, have been widely used to create biodegradable face masks [3]. To the best of our knowledge, the degradation of face masks made from linen/cotton blend and Himalayan hemp has not been studied yet. Based on organic carbon content measurements under controlled conditions the produced CO_2 was calculated. The microcrystalline cellulose was selected as a reference material according to ISO standards [17,18]. The biodegradation rate was calculated based on the measurements of produced CO_2. The results of the material after the respirometric measurements were verified using FTIR spectroscopy and microscope images.

MATERIAL AND METHODS

Materials

Initially, 4 different types of compost were studied first to determine their maximum activity. Compost used: Humovit univerzal, composition: white and black peat, coconut fiber, organic foam, quartz sand, and Hygromull; Substratica Compact mix, made of humic acids, white and black peat, perlite, stone flour; Bioplantella, made of white and black peat; Substral premium, made of peat, compost from plant residues, wood fiber, composted bark, and fertilizer. The chemical composition is presented in Table 1.

Table 1. Chemical composition of tested types of compost.

Content Element	Hummovit	Substratica	Bioplantella	Substral
Organic matter (%)	35–50	-	-	20
P_2O_5 (mg/100 g)	100–200	200–500	150–250	-
K_2O (mg/100 g)	150–250	200–500	200–300	-
Total N (mg/100 g)	600–1200	20–50	130–180	-
pH	6.5–7.2	6.5–7.2	6.2–6.8	5.2–6.8

The degradation of several different protective masks was tested. All were commercially available: made of polypropylene (PP); made of Himalayan hemp fibers (HK); made of linen and cotton mixed fibers (LB), two layers: the inner layer was made from 100% cotton and the outer from 50% linen and 50% cotton; made of blown cellulose (PC); microcrystalline cellulose (MC) served as control (Reference material, Ref), Sigma-Aldrich, mass was 32 g per reactor. The masks were cut into particles with an area between 0.5 cm^2 and 2 cm^2.

Respirometry measurements

Mask polymer degradation was determined by carbon dioxide (CO_2) evolution and monitored using an ECHO Instruments respirometer (Slovenske Konjice, Slovenia). Each experimental set was carried out in a 12-channel respirometer for measurements in compost and in a 6-channel respirometer for measurements in aqueous media. Data handling in each reactor was automatic. An airflow of 50 mL min^{-1} was pumped into each reactor, and the composition of exhausted gas was analyzed using the built-in gas sensors. All samples were performed in duplicate for two and a half months and compared against microcrystalline cellulose as the positive control at constant conditions. The mass of produced CO_2 for each tested sample (in g) was calculated in approx. 2 hours intervals by the difference in mass of produced CO_2 in each sample and mass of produced CO_2 in blanks, as described by Eq. (1):

$$m_p = m_{r,s} - m_b \quad (1)$$

where, m_p is the mass of produced CO_2 (g) derived from the tested sample (or reference), $m_{r,s}$ is the mass of produced CO_2 from the reference or the tested sample, and m_b is the mass of produced CO_2 from the blanks.

Biodegradability was determined by following Eq. (2):

$$w_d = \frac{m_p}{m_m \cdot TOC \cdot r_M} \cdot 100 \quad (2)$$

where w_d is the biodegradability (%), m_m is the mask mass (g), TOC is the total organic carbon (%), and r_M is the ratio of molar masses CO_2 to C.

Compost activity w_a is calculated according to Eq. (3):

$$w_a = \frac{m_p}{m_{vS}} \quad (3)$$

where m_p is the mass of produced CO_2 in the compost after 10 days (in mg) and m_{vs} is the mass of volatile solids (in g).

The mass of volatile solids is calculated according to Eq. (4):

$$m_{vS} = m_{compost} \cdot \frac{d_m}{100} \cdot \frac{vs}{100} \quad (4)$$

where $m_{compost}$ is the mass of compost (in g), d_m is the dry matter (in %) and vs is the volatile matter (in %).

Respirometry experiments in compost

The sample composition in individual reactors is seen in the next paragraph.

Reactor number	Content	Denotation
1 and 2	Compost	K
3 and 4	Compost + microcrystalline cellulose	KMC
5 and 6	Compost + polypropylene	KPP
7 and 8	Compost + linen/cotton	KLB
9 and 10	Compost + blown cellulose	KPC
11 and 12	Compost + Himalayan hemp	KHK

Two replicate measurements were performed.

Respirometry experiments in an aqueous medium

The aqueous medium was prepared according to the instructions in the standard (ISO 14852), which describes the preparation from four mineral solutions (B, C, D, and E) and the compost inoculum.

Solution B: 1.10 g of $MgSO_4$ was dissolved in a 100 mL volumetric flask.

Solution C: 2.75 g of $CaCl_2$ was dissolved in a 100 mL volumetric flask.

Solution D: 0.125 g of $FeCl\,.H_2O$ was dissolved in a 0.5 L volumetric flask. Solution D must always be prepared fresh or a drop of concentrated HCl.

Solution E: 37.5 g of KH_2PO_4, 69.6 g of Na_2HPO_4, and 2 g of NH_4Cl were dissolved in a 1 L volumetric flask with deionized water. In the case of difficult solubility, the flask was placed in an ultrasonic bath for a few minutes. Other solutions can be stored for up to 6 months in a dark place. Test medium, which is a mixture of the previously listed solutions in a certain ratio, was prepared: 800 mL of deionized water, 100 mL of solution E in 1 mL of solution B, C, and D were mixed. The pH of the test medium was then adjusted to 7.0 ± 0.2.

Inoculum: 10 g of compost was suspended in 100 mL of the test medium by mixing well. After 30 min the solution was filtered through a 2 mm, followed by a 1 mm sieve and a 0.2 mm sieve. Finally, a 5% compost solution in the aqueous medium was prepared. The Blank was prepared without plastic material. Microcrystalline cellulose served as reference control material. PP, HK, LB, and PC were tested for degradation with a mass of 2 g per 0.5 L solution. The respirometric experiments were performed in the same manner as described in the section Respirometic measurements at 303.15 K.

FTIR spectroscopy

The samples were analyzed with the spectrometer ATR FTIR Perkin Elmer Spectrum GX (Perkin Elmer FTIR, Omega, Ljubljana, Slovenia). The ATR accessory (supplied by Specac Ltd., Orpington, Kent, UK) contained a diamond crystal. A total of 16 scans were taken of each sample with a resolution of 4 cm^{-1}. All spectra were recorded at ambient temperature over a wavenumber range between 4000 and 650 cm^{-1}.

Microscopy

Microscope BRESSER Science Infinity 57-60700, equipped with camera BRESSER MikroCam SP 5.0 was used to perform microscopic images in a magnification range of 40-1000x.

RESULTS AND DISCUSSION

A preliminary test with all compost types was performed first to determine the activity of all compost samples according to ISO 14855. The pH was maintained between 7 and 8. The results are shown in Fig. 1. The condition for compost application is its activity between 50 and 150 mg/g reached in about 10 days. From Fig.1 it is seen that the highest activity was obtained using Humovit. The results are in agreement with the measurement of dry residue lost, which was the lowest with Humovit.

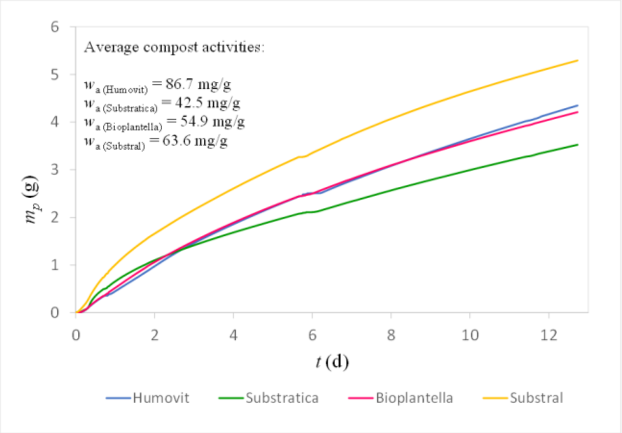

Figure 1. (a) Average values of produced CO_2 (mp) in 12 days and calculated average activity values for the tested compost samples.

The activities were calculated according to Eq. 3. Compost activities were calculated the highest for Humovit 86.7 ± 4.9%, followed by Substral 63.6 ± 0.4%, Bioplantella 54.9 ± 2.7%, and Substratica 42.5 ± 3.3%.

Further, pH remained within demanded values until the end of the experiment, between pH 7 and pH 8, whereas Substratica and Bioplantella composts showed values between pH 5.6 and 6.6, respectively, - this is out of the demanded pH range. Therefore, Humovit was chosen for further experiments. Throughout the time interval of samples' incubation in the compost, we carefully monitored the activity of microorganisms. The functioning of microorganisms is also reflected in the consumption of oxygen, which microorganisms need for cellular respiration. Regarding aerobic cell respiration (reaction 4), the moles of consumed O_2 are linear to moles of produced CO_2. Based on this assumption, the produced CO_2 could be calculated from the reaction in Eq. (5):

$$C_6H_{12}O_6 + 6O_2 \rightarrow 6CO_2 + 6H_2O + ATP \tag{5}$$

Fig. 2a shows the final measurement values of produced CO_2 for the two parallel samples of each tested polymer versus blank samples. We noticed that the produced CO_2 value is the highest for samples with added microcrystalline cellulose, which we used for reference. Very close values are reached with the LB mixture, a little lower with PC, and even lower with HK, while PP showed the m_p values comparable with the blank as reported by others [19,20,21].

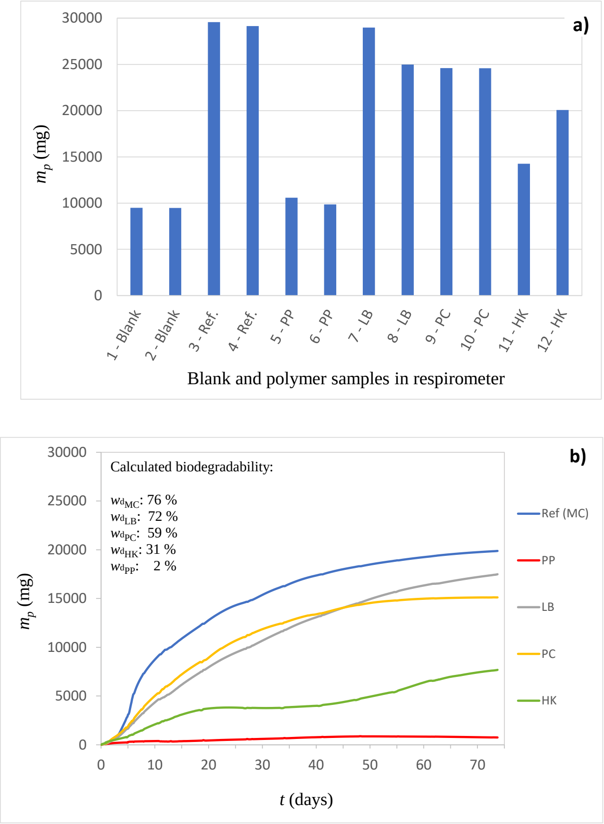

Figure 2. (a) Final production of CO_2 for all tested samples in the respirometer; (b) Production of CO_2 deducted for blank samples for MC, LB, PC, HK, and PP, respectively; each graph represents the mean values of 2 replicates. All samples in (a) and (b) are measured in Humovit compost during 73 days of respirometric measurements.

Fig. 2b presents the average cumulative CO_2 production (in mg) for the tested samples deducted for blank samples during the whole respirometric test in compost, where the produced CO_2 in compost was considered. The calculated biodegradability was the highest in the case of reference MC, about 76%, followed by LB and PC, which reached 72% and 59% biodegradation rates, respectively. High biodegradability was confirmed with LB. The disintegration of linen fabric under composting conditions was reported at a lower value of 55% [22]. Similar results were achieved in the present study and this could be explained by enzyme attack of the cellulose chain and break-down of the cellulose internal bands. The main difference is between the shape of the LB and PC curves. LB seemed to still degrade, while PC reached a plateau. Similar results were obtained by others – In this period after the 50th day, the disintegration of linen can still proceed [22]. Validity of the test or measurement according to the standard was also achieved, as the percentage of biodegradation for microcrystalline cellulose was above 70% in 45 days [17]. TOC represents the nutrients for microorganisms; however, carbon could be unavailable for biodegradation. The results showed the highest share of TOC in PP (almost 79%), while in PC, LB, and HK the values were similar, between 42 and 44 %. Many compostable materials need extended periods above 45 days for composting [23]. The HK was shown as not readily biodegradable, reaching only a 31% rate. According to Himalayan hemp amorph structure, it could result in being more biodegradable, but on the other hand, HK is known for its high mechanical strength [24], which presumably slows down the biodegradation process.

A comparison between the PP degradation with pretreatment methods showed similar non-degradability as in our study. The degradation of polypropylene was previously investigated in several studies, where it was exposed to several types of microbial cultures under different conditions. The degradation of PP was not improved by using *Lysinibacilus*, while only 3% dry residue loss was observed [25]. Similarly, Flexus did not improve PP degradation after 365 days, as only 1.95% and 1.45% degradation were measured [20, 21]. If the PP was pre-treated by the UV, the results were much better only in one study, where more than 60% of PP was degraded.

Microscopy results

Pieces of protective masks were recorded under a microscope with 40x magnification. The micrographs were used to visually compare the mask material after the composting experiment and observe possible changes on the surface of the sample (fibrillation).

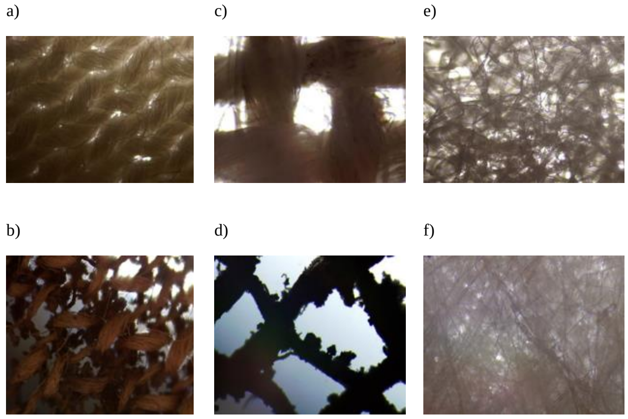

Figure 3. Micrographs of linen/cotton, hemp, and polypropylene before LB (a), HK (c), PP (e), and after respirometric measurements in Humovit compost LB (b), HK (d), PP (f) recorded at 40-times magnitude.

All materials showed some increased pore size after composting. Among them the difference was most obvious in the LB material, as shown in Fig. 3a and 3b (before and after composting, respectively). Comparing the micrographs of HK (Fig. 3c and 3d), we also noticed some fibrillation of the fibers after composting (Fig. 3d), as well as an increase in pore size compared with raw fibers. Minimal changes in pore size were observed at PP (Fig. 3f) compared to PP before composting (Fig. 3e). Also, the pore size was the smallest in the PP sample (Fig. 3e).

FTIR spectroscopy results

There were no observed major differences in the spectra of PP, HK, and PC. Small differences were seen from FTIR spectra for LB. The broad signal at the wavenumber of 3333 cm^{-1} is an indication of the existence of a hydrogen bond in the molecule and the longitudinal valence fluctuations of the OH-bond. The stretching vibration of the CH-bond appears as a medium-strong signal at a wave number of 2900 cm^{-1}. According to our predictions, the signal at 1630 cm^{-1} is the result of bending vibrations of the OH-bond of adsorbed water. At the wavenumber of 1315 cm^{-1}, a smaller signal is observed, which is the result of vibration due to the bending of the CO bond. The vibration of CO- and OH-bonds is the cause of the most intensely expressed signal at the wave number of 1030 cm^{-1} [26]. Another study describes the degradation of linen by composting and similar spectra before and after the biodegradation experiment were obtained [22].

Results of experiments in aqueous media

Fig. 4 represents the production of CO_2 (in mg) for LB, HK, and PP, comparably with the reference MC. MC was set as reference material in two replicates. The produced CO_2 was above 2000 mg in 70 days. It did not reach the plateau and was still increasing after 70 days. The tests should be prolonged to achieve the final degradation rate.

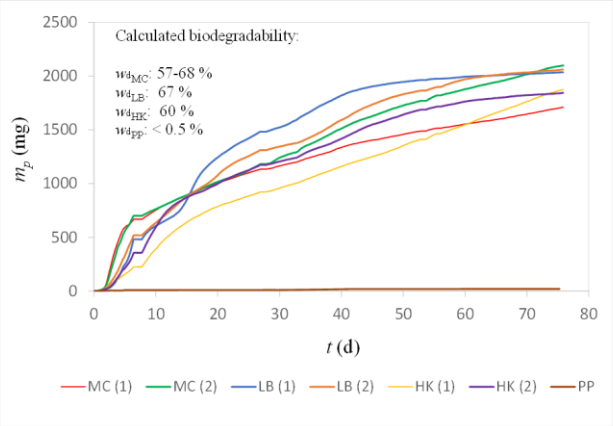

Figure 4. Production of CO_2 during two months of respirometric measurements for MC, LB, HK, and PP, respectively, in water media; each graph represents the mean values of 2 replicates.

LB blend seemed to reach the plateau after 60 days of respirometric measurements, which means the degradation rate slowed down. The biodegradability was calculated at 67%. The results showed slightly lower biodegradation as reported for cotton, 89% [27]. In our case, the result might suggest that some chemical additions to mask material to improve the mask strength might interfere with the degradation process.

The protective mask made of HK was degrading somehow similarly and reached about 60% biodegradation after 70 days; however, from the recorded graphs it is seen that prolonged time could be able to contribute to a further increase in CO_2 production. The protective mask made of PP was not biodegradable, with calculated biodegradation below 0.5%, which is in accordance with the literature [28]. As seen from Fig. 4 the prolonged time might contribute to a further increase in CO_2 production.

Fig. 5 presents the microscopic graphs of LB and HK at 40 times magnitude. The woven linen/cotton structure is seen in Fig. 5a (before starting the respirometric test), whereas in Fig. 5b (after finishing the test) it is seen as the disintegrated material, as fibers are not visible anymore. Similar was observed with HK as seen in Fig. 5c and 5d.

FTIR spectroscopy results

Fig. 6 shows the FTIR spectra for a PP medical mask before and after the experiment according to ISO 14852. Spectra a) and c) represent the outer layer of the mask before and after the experiment, while spectra b) and d) represent the inner layer of the medical mask, which is slightly thinner and more transparent. The spectra of the outer and inner layers (6a and 6b)

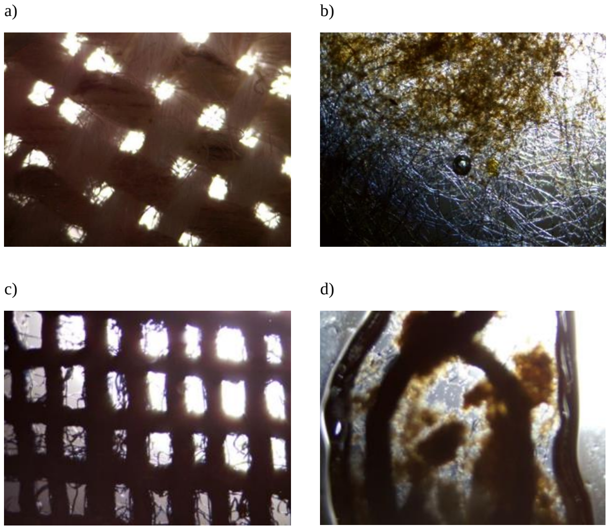

Figure 5. Micrographs of linen/cotton and hemp before LB (a), HK (c), and after respirometric measurements in aqueous media LB (b), HK (d) recorded at 40-times magnitude.

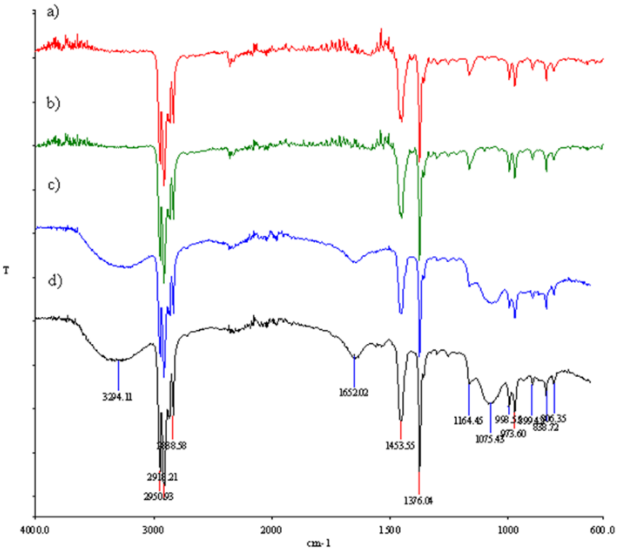

Figure 6. FTIR spectra for a polypropylene medical surgical mask: (a) outer layer before respirometric measurements in compost/aqueous media; (b) inner layer, layer before the experiment; (c) outer layer after the experiment; (d) inner layer after the experiment.

showed the following signals: multiple signals in the wavenumber range from 3000 to 2800 cm^{-1} and two large signals in the range from 1456 to 1375 cm^{-1}. The signals in the range from 3000 to 2800 cm^{-1} were attributable to asymmetric and symmetric stretching vibrations of CH_2 groups, while the signals at 2950 and 2850 cm^{-1} were due to the asymmetric and symmetric stretching vibrations of CH_3. The signal at 1456 cm^{-1} indicates the asymmetric CH_3 vibrations or CH_2 scissor vibrations, while the signal at 1375 cm^{-1} was the result of the symmetric CH_3 deformation. All mentioned signals represent typical signals for PP materials. We found from the spectra that there is no difference between the materials of the outer layer and the inner layer, but the inner layer is made of finer fibers to serve as a filter. The same spectrum for PP was also recorded by other authors [29], who investigated the release of microplastics from medical masks in seawater. The FTIR spectra of the outer and inner layer after the experiment (6c and 6d) show new signals around 3300 cm^{-1}, 1650 cm^{-1}, and 1007 cm^{-1}. Listed signals at corresponding wavenumbers are typical for O-H, C=O, C-O, etc. vibrations. The latter indicates that PP undergoes oxidation/degradation reactions.

Even with the linen/cotton mask, we did an FTIR analysis of two parts of the mask, i.e. the inner one, which is supposed to be made of 100% cotton, and the outer one, which is composed of 50% linen and 50% cotton. FTIR spectra are identical, since both linen and cotton, as natural polymers, are mostly composed of cellulose. The spectra are also unsurprisingly similar to the spectra of blown cellulose and Himalayan hemp (not presented here). The FTIR spectra of the light layer of the linen/cotton mask before and after the experiment were compared, but there were no differences between them. For the FTIR analysis of the state of the bright layer of the linen/cotton mask after the experiment, a slightly more preserved piece of string was used, which could be the reason for the unchanged spectrum result compared to the spectrum of the material before the experiment.

CONCLUSION

Protective face masks made of linen/cotton met our expectations regarding biodegradation in compost media. The masks made of Himalayan hemp fibers were not as biodegradable as expected, reaching only 31% degradation. From the results, we can conclude that longer monitoring time is required, since the biodegradation rate began to increase significantly only after 1 month. Validity of the test or measurement according to ISO 14855 standard was achieved, since the biodegradation percentage of 70% for microcellulose was achieved in 45 days.

From the results in aqueous media, we can summarize the findings that protective face masks were readily biodegradable, while the medical mask made of polypropylene was not. Reference material degradation was measured between 57% and 68%. Thus, it was proven that the large-scale use of linen/cotton face masks would reduce the consumption of non-renewable resources, thus reducing the emission of greenhouse gases and other toxic pollutants, as well as conventional plastic pollution.

ACKNOWLEDGMENTS

The authors thank Žiga Šrot and Jernej Jelenko for performing the laboratory experiments. This work was supported by the Slovenian Research Agency under the research program P2-0118 Textile Chemistry and P2-0032 Process Systems Engineering and Sustainable Development.

REFERENCES

[1] O.O. Fadare, E.D. Okoffo, Sci. Total. Environ. 1 (737) (2020) 140279. https://doi:10.1016/j.scitotenv.2020.140279.

[2] A. Brochocka, A.Nowak, K.Majchrzycka, M. Puchalski, S. Sztajnowski, Materials 13(3) (2020) 712. https://doi.org/10.3390/ma13030712.

[3] X. Wang, D. Huang , J.H. Ji, C. Völker, F. Wurm, Adv. Sci. 8(1) (2021) 2001121. https://doi.org/10.1002/advs.202001121.

[4] S. Adanur, A. Jayswal, J. Ind. Text. 51(3) (2022) 3683S–3717S. https://doi.org/10.1177/1528083720980169.

[5] N. A.Hasan, R.D. Heal, A. Bashar, M.M. Haque, Environ. Challenges 4 (2021) 100126. https://doi.org/10.1016/j.envc.2021.100126.

[6] S.K. Kale, A.G. Deshmukh, M.S Dudhare, V.B. Patil, J. Biochem. Technol. 6(2) (2015) 952–961. https://doi.org/10.31838/ijpr/2021.13.01.245.

[7] Y.K Song, S.H. Hong, M. Jang, G.M. Han, S.W. Jung, W.J. Shim, Environ. Sci. Technol. 51 (2017) 4368–4376. https://doi.org/10.1021/acs.est.6b06155.

[8] M. Kozjek, D. Vengust, T. Radošević, G. Žitko, S. Koren, N. Toplak, I. Jerman, M. Butala, M. Podlogar, M.K. Viršek, Sci. Total. Environ. 856(1) (2023) 158786. https://doi.org/10.1016/j.scitotenv.2022.158786.

[9] S. Miri, R. Saini, S.M. Davoodi, R. Pulicharla, S.K. Brar, S. Magdouli, Chemosphere 286 (1) (2022) 131670. https://doi.org/10.1016/j.chemosphere.2021.131670.

[10] S. Muenmee, W. Chiemchaisri, C. Chiemchaisri, Int. Biodeter. Biodegr. 113 (2016) 244–255. https://doi.org/10.1016/j.ibiod.2016.03.016.

[11] S. Skariyachan, A.S. Setlur, S.Y. Naik, A.A. Naik, M. Usharani, K.S. Vasist, Environ. Sci. Pollut. Res. Int. 24(9) (2017) 8443–8457. https://doi.org/10.1007/s11356-017-8537-0.

[12] H. Spanjers, P. Vanrolleghem, G. Olsson, P. Doldt, Water Sci. Technol. 34 (3-4) (1996) 117–126. https://doi.org/10.1016/0273-1223(96)84211-9.

[13] M.S. Rahman, M.A. Islam, Appl. Water Sci. 5 (2014) 241–252. https://doi.org/10.1007/s13201-014-0185-7.

[14] U. Strotmann, G. Thouand, U. Pagga, S. Gartiser, H. Heipieper, Appl. Microbiol. Biotechnol. 107 (2023) 2073–2095. https://doi.org/10.1007/s00253-023-12406-6.

[15] R.P. Dumitriu, E.Stoleru, G.R. Mitchell, C. Vasile, M. Brebu, Molecules 26 (2021) 5498. https://doi.org/10.3390/molecules26185498.

[16] A. Irimia, E. Stoleru, C. Vasile, A. Bele, M Brebu, Coatings 11(10) (2021) 1211. https://doi.org/10.3390/coatings11101211.

[17] ISO 14855-2 (2018) Determination of the ultimative aerobic biodegradability of plastic materials under

controlled composting conditions - Method by analysis of evolved carbon dioxide - Part 2: Gravimetric measurement of carbon dioxide evolved in a laboratory-scale test, Geneva, Switzerland.

[18] ISO 14852 (2021) Determination of the ultimate aerobic biodegradability of plastic materials in an aqueous medium – Method by analysis of evolved carbon dioxide, Geneva, Switzerland.

[19] S. Skariyachan, A.A. Patil, A. Shankar, M. Manjunath, N. Bachappanavar, S. Kiran, Polym. Degrad. Stab. 149 (2018) 52–68. https://doi.org/10.1016/J.POLYMDEGRADSTAB.2018.01.018.

[20] J.M. Jeon, S.J. Park, T.R. Choi, J.H. Park, Y.H. Yang, J.J. Yoon, Polym. Degrad. Stab. 191 (2021) 109662. https://doi.org/10.1016/j.polymdegradstab.2021.109662.

[21] H.S. Auta, C.U. Emenike, B. Jayanthi, S.H. Fauziah, Mar. Pollut. Bull. 127 (2018) 15–21. https://doi.org/10.1016/j.marpolbul.2017.11.036.

[22] M. Esmaeilzadeh, A. Rashidi, Environ. Sci Pollut. Res. 25(29) (2018) 29070-29077. https://doi.org/10.1007/s11356-018-2917-y.

[23] L. Reisman, A. Siehr, J. Horn, D.C. Batiste, H. Kim, G.X. De Hoe, J. Ellison, W. Shen, E.M. White, MA. Hillmyer, ACS Sustain. Chem. Eng. 9 (2021) 2736–2744. https://doi.org/10.1021/acssuschemeng.0c08026.

[24] A. Karimah, M.R. Ridho, S.S. Munawar, D.S. Adi, I. Notowiharjo, R. Damayanti, B. Subiyanto, W. Fatriasari, A. Fudholi, J Mater. Res. Technol. 13 (10) (2021) 2442–2458. https://doi.org/10.1016/j.jmrt.2021.06.014.

[25] S. Skariyachan, N. Taskeen, A.P. Kishore, B.V. Krishna, G. Naidu, J. Environ. Manage. 284 (9) (2021) 112030. https://doi.org/10.1016/j.jenvman.2021.112030.

[26] E.H. Portella, D. Romanzini, C. Angrizani, S.C. Amico, A.J. Zattera, Mater. Res. 19 (3) (2016) https://doi.org/10.1590/1980-5373-MR-2016-0058.

[27] M.C. Zambrano, J.J. Pawlak, J. Daystar, M Ankeny, C.C. Goller, R.A. Venditti, Mar. Pollut. Bull. 151 (2020) 110826. https://doi.org/10.1016/j.marpolbul.2019.110826.

[28] P. Luthra, V.K. Kottiyath, V. Goel, R. Singh, G.S. Kapur, SN Appl. Sci. 2 (2020) 512. https://link.springer.com/article/10.1007/s42452-020-2287-1.

[29] S. Francesco, V. Maurizio, R. Clarissa, B. Davide. G. Paolo, L. Marina, Environ. Adv. 4 (2021) 100042. https://doi.org/10.1016/j.envadv.2021.100042.

JULIJA VOLMAJER VALH[1]
MATEJKA TUREL[2]
ANDREJ HOLOBAR[2]
MARJANA SIMONIČ[3]

[1]University of Maribor, Faculty of Mechanical Engineering, Institute of Engineering Materials and Design, Maribor, Slovenia

[2]ECHO Instruments d.o.o, Slovenske Konjice, Slovenia

[3]University of Maribor, Faculty of Chemistry and Chemical Engineering, Maribor, Slovenia

NAUČNI RAD

BIORAZGRADNJA ZAŠTITNIH MASKI (COVID-19) U KOMPOSTU I VODENIM MEDIJIMA

Izvršena su istraživanja biorazgradnje maski za lice od prirodnih i sintetičkih materijala. Eksperimentalni deo je izveden sa respirometrom slovenačkog proizvođača ECHO Instruments. Izvršili je preliminarni test za odabir komposta sa najvećom aktivnošću za dalji rad. Brzina biorazgradnje materijala izračunata je na osnovu merenja ugljen(IV)-oksida proizvedenog u reaktorima. Rezultati biorazgradljivosti materijala su verifikovani korišćenjem FTIR spektroskopije i mikroskopskih slika. Maske napravljene od čestica lana i pamuka imale su najbolju biorazgradnju od 72%, dok čestice maski od polipropilena (PP) nisu degradirale. Budući da ne postoje studije o biorazgradivosti u vodi, drugi deo istraživanja odnosio se na brzina razgradnje maski u otpadnoj vodi. Na osnovu dobijenih FTIR spektara, potvrđeno je prisustvo novih funkcionalnih grupa na površini zaštitnih maski kao rezultat procesa oksidacije. Kompost Humovit je izabran kao inokulum za vodeni medijum. Najveći stepen biorazgradnje je utvrđen za masku od lana I pamuka (67% za 75 dana).

Ključne reči: zaštitne maske; lan/pamuk; himalajska konoplja; respirometrija; FTIR.

CI&CEQ
Chemical Industry & Chemical Engineering Quarterly

Available online at
Association of the Chemical Engineers of Serbia *AChE*
www.ache.org.rs/CICEQ

Chem. Ind. Chem. Eng. Q. 31 (2) 139–149 (2025) CI&CEQ

MAHA ABDELILEH[1,2]
MANEL BEN TICHA[3]
NIZAR MEKSI[1,2]
HATEM DHAOUADI[1]

[1]University of Monastir, Faculty of Sciences of Monastir, Research Laboratory of Environmental Chemistry and Clean Processes, Monastir, Tunisia

[2]University of Monastir, National Engineering School of Monastir, Department of Textile, Monastir, Tunisia

[3]Department of Early Childhood, University College of Turabah, Taif University, Taif, Saudi Arabia

SCIENTIFIC PAPER

UDC 667:667.2:546.72.06

AN ENVIRONMENTALLY FRIENDLY INDIGO DYEING PROCESS USING IRON (II) GLUCONATE AS A REDUCING AGENT

Article Highlights

- An ecological indigo dyeing process using iron (II) gluconate as a reducing agent was studied
- Iron (II) gluconate molecule is very stable with high hardness, and a large energy gap
- A comparable dyeing quality to that of the conventional process has been achieved
- Cleaner wastewater was obtained by this dyeing process

Abstract

This research paper aims to replace the ecologically harmful sodium dithionite traditionally used in the indigo dyeing process with the iron (II) gluconate reducing agent. The density functional theory (DFT) method using the B3LYP 6-311 G(d,p) basis set was used to determine the optimized structures of iron(II) gluconate and indigo. The highest occupied molecular orbital (HOMO) energy and the lowest unoccupied molecular orbital (LUMO) energy were calculated, and the electronic properties dependent on HOMO-LUMO energies were determined. Furthermore, an ecological dyeing process using this reducing agent was studied. The influences of alkalinity, reduction temperature, and iron(II) gluconate concentration on the fulfillment of the dyeing process were inspected by measuring the obtained redox potential and the color strength of the dyed samples. A full factorial experiment was performed for statistical analysis and optimization of the dyeing process. The results revealed that the developed method is highly effective and capable of generating redox potential and dyeing quality comparable to those obtained with the conventional process employing sodium dithionite. Finally, the substitution of sodium dithionite with iron (II) gluconate reduced the wastewater load generated by the conventional dyeing process.

Keywords: indigo dyeing; density functional theory; ecological process; iron(II) gluconate; process optimization.

With annual sales of over 5 billion blue jeans worldwide, the production of denim fabric is considered one of the most important sectors of the clothing industry [1]. As economic progress and living standards improve, the importance of indigo, the dye used in denim production, continues to grow within the dyeing sector for blue jeans [2].

In the continuous dyeing process, this initially insoluble dye needs to be converted into its leuco-soluble form, which exhibits a low affinity for cellulosic fibers. During dyeing, cotton yarns are submerged in a dye bath containing the reduced form of indigo (leuco indigo), squeezed, and subsequently exposed to air, to convert the leuco dye back to its original insoluble form. To achieve the necessary dye fixation, the immersion and oxidation steps must be repeated multiple times. Nowadays, most indigo dyeing processes rely on the utilization of sodium dithionite ($Na_2S_2O_4$) as a reducing agent to obtain the soluble leuco form of the dye. The reduction reaction of indigo with conventional sodium dithionite in an alkaline medium is represented by

---

Correspondence: M. Abdelileh, University of Monastir, Faculty of Sciences of Monastir, Research Laboratory of Environmental Chemistry and Clean Processes, 5000Monastir, Tunisia.
E-mail: maha.abdelileh@gmail.com
Paper received: 6 January, 2024
Paper revised: 3 June, 2024
Paper accepted: 10 june, 2024

https://doi.org/10.2298/CICEQ240106022A

Reaction 1:

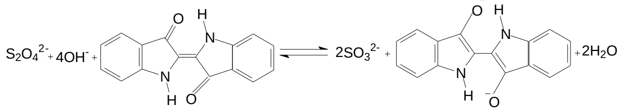

Nevertheless, the use of this reductant has been attacked for the formation of by-products such as sulfides, sulfites, sulfates, thiosulfates, and toxic sulfur. These by-products have a hazardous impact on the environment when released into sewage due to their toxicity. Furthermore, the release of large amounts of sodium dithionite into wastewater increases the wastewater treatment burden [3]. Therefore, many initiatives have been developed to substitute sodium dithionite with more environmentally friendly alternatives, such as the electrochemical reduction of indigo [4]. This method uses a regenerable redox system in the dye bath, which is constantly regenerated by cathodic reduction [5,6].

Several mediator solutions, including anthraquinonoid compounds [7] and iron (II) complexes with various ligands such as iron(II)-sodium gluconate-Abal B [1] and iron-triethanolamine-calcium gluconate [8] have been used to reduce indigo. These mediator solutions have demonstrated comparable dyeing performance to the standard indigo dyeing process utilizing sodium dithionite. Furthermore, Changhai *et al.*'s patent describes an indirect electrochemical reduction using gluconic acid and iron triethanolamine as a regenerable redox system to generate a synergistic effect [9]. This method enhances current efficiency, leading to a significant reduction in energy consumption, thus making it cost-effective. Also, the utilization of a divalent copper ion complex combined with electrochemical technology for reducing indigo using sodium borohydride at room temperature has been investigated by *Xiaoyan* and his team [10]. Through the optimization of experimental conditions, they achieved a redox potential of -968mV and a K/S value of 11.92, comparable to that of the conventional reduction process with sodium dithionite. Indirect electrochemical reduction technology not only reduces chemical usage but also enables the control of dye reduction conditions using electrochemical techniques. While direct recycling of the mediator solution and water is possible, it comes with significant energy demands and necessitates a sizable electrode surface. Moreover, there is an additional expense associated with mediator filtration.

Besides, the use of organic reductants as greener alternatives to sodium dithionite such as sodium borohydride [11,12] and α-hydroxyacetones [13] are widely used. These reducing agents can make the grades of efficiency and biodegradability. Ferrous salts have been extensively used to reduce indigo. Indeed the use of iron (II) sulfate complexed with various ligands such as tartaric, citric, and gluconic acids for indigo reduction and dyeing in the presence of NaOH was studied [14–16]. This method enhances the solubility of iron (II) hydroxide in the dye bath responsible for the indigo reduction and gives an acceptable dyeing quality and cleaner effluents. Subsequent removal of gluconic acid is achieved by neutralization with a small amount of alkali in the wastewater tank.

This paper reports the application of iron (II) gluconate for indigo reduction and dyeing. This ferrous compound is generally used as a food additive and dietary supplement. The ionization energy, electron affinity, and global reactivity descriptors of iron (II) gluconate and indigo were calculated using the DFT method. Similarly, the nucleophilic and electrophilic sites of iron (II) gluconate were determined by molecular electrostatic potential (MEP). An environmentally friendly process was developed for dyeing cotton with indigo using iron (II) gluconate as a reducing agent. The influence of experimental parameters (sodium hydroxide concentration, reduction temperature, and iron (II) gluconate concentration) on redox potential and dyeing performance was studied. During the dyeing process, this reducing agent is converted after aeration to a ferric compound that acts as a flocculant and will be removed during wastewater treatment [16]. For statistical analysis, a full factorial experiment was performed to obtain the optimal experimental conditions for indigo reduction. The residual dye bath of the process using ferrous gluconate as a reducing agent was evaluated and compared to the process using sodium dithionite.

MATERIAL AND METHODS

Materials

The chemicals used were of analytical grade: Sodium hydroxide (NaOH, ≥ 99%, Loba Chemie, Germany), iron (II) gluconate dihydrate ($C_{12}H_{22}FeO_{14}$, Sigma-Aldrich, USA), sodium dithionite ($Na_2S_2O_4$, BASF, Germany), ammonium iron (II) sulfate ($(NH_4)Fe(SO_4)_2(H_2O)_6 \geq$ 99%, Sigma-Aldrich, USA), potassium dichromate ($K_2Cr_2O_7 \geq$ 99%, Sigma-Aldrich, USA), mercury(II) sulfate ($HgSO_4$, Chemsolute, Germany), sulfuric acid ($H_2SO_4 \geq$ 95%, Scharlau, Spain), silver sulfate ($Ag_2SO_4 \geq$ 99%, Sigma-Aldrich, USA).

Indigo powder ($C_{16}H_{10}N_2O_2$, Benzema, Switzerland) was used for dyeing cotton samples. For dyeing experiments, a bleached cotton fabric (100% cotton) was used with the following specifications: plain weave, mass per area 173 g/m², warp count of

25 yarns/cm, and weft count of 31 yarns/cm.

Computational details

The DFT calculations were carried out using Gaussian program package 09, while Gauss View 5 was used for visualization of the structure and simulation of the vibrational spectra. In this study, the B3LYP 6-311 G(d,p) basis set was employed to obtain the optimized structures with minimum energy of iron (II) gluconate and indigo. The ionization Energy (IE), electron affinity (EA), and global reactivity descriptors such as chemical potential, hardness, softness, electronegativity, and electrophilicity index of iron (II) gluconate and indigo molecules have been evaluated from the highest occupied molecular orbital (HOMO) and lowest unoccupied molecular orbital (LUMO) frontier molecular (FMO) energy values. The global reactivity descriptors using Koopman's theorem [17] are given by the following equations:

The chemical potential: $$\mu = \frac{-(IE+EA)}{2} \tag{1}$$

The hardness: $$\eta = \frac{(IE-EA)}{2} \tag{2}$$

The softness: $$S = \frac{1}{2\eta} \tag{3}$$

The electronegativity: $$\chi = \frac{(IE+EA)}{2} \tag{4}$$

Global electrophilicity index: $$\omega = \frac{\mu^2}{2\eta} \tag{5}$$

where the ionization energy, *IE = -EHOMO* and the electron affinity, *EA = -ELUMO*.

Indigo reduction processes

A solution containing 2 g·L^{-1} of indigo, sodium hydroxide ranging from 5 to 30 g·L^{-1}, and iron (II) gluconate ranging from 2 to 25 g·L^{-1}, was heated to a temperature between 50 °C and 90 °C for 2 hours. The indigo reduction was executed in an AHIBA dyeing machine, and redox potential measurements were performed at the end of the process using a pH meter (pHM210) equipped with a platinum electrode and a reference electrode (Ag/AgCl, 3KCl). Iron (II) gluconate, in an alkaline medium, generates iron (II) hydroxide which is a reducing agent known for its ability to reduce vat dyes, especially indigo [18] (Reaction 2).

$$C_{12}H_{22}FeO_{14} + 2\ NaOH \rightleftharpoons Fe\,(OH)_2 + 2C_6H_{11}NaO_7$$

The reduction reaction of indigo with iron(II) gluconate is represented by Reaction 3. The reduced bath was then used for dyeing experiments using the (6dip-6nip) method, elucidated thoroughly in the subsequent section.

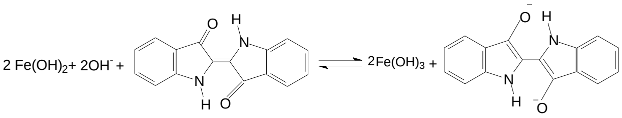

To compare the dyeing results achieved with iron (II) gluconate as a reducing agent with those of conventional methods, a series of tests employing sodium dithionite as a reducing agent were conducted. These tests adhered to the guidelines of the traditional process used at an industrial scale. Typically, the dye bath contains 2 g·L^{-1} of indigo, 4 g·L^{-1} of sodium hydroxide, and 4 g·L^{-1} of sodium dithionite, maintained at a temperature of 50 °C for 2 hours [19].

Dyeing process

Cotton samples were dyed by impregnation. After dipping the samples in the dye bath for 1 min, they were exposed to air for approximately 2 min, to complete a cycle (1 dip-1 nip). This step was repeated 6 times. Afterward, the samples were cold rinsed and dried at ambient temperature.

Color strength measurement

The dyeings were assessed by measuring the color strength (K/S) at 660 nm using a spectra flash 600+ spectrophotometer (Datacolor international, USA, illuminant: D 65, geometry: d/10°). The presented results were calculated as the mean of three values. The color strength value (K/S) was calculated according to the following equation [20]:

$$\frac{K}{S} = \frac{(1-R)^2}{2R} - \frac{(1-R_0)^2}{2R_0} \tag{6}$$

where R is the decimal fraction of the reflectance of the dyed sample, R_0 is the decimal fraction of the reflectance of the undyed sample, K is the absorption coefficient, and S is the scattering coefficient.

Bath exhaustion measurement

A volume of 1 mL was extracted from the dyeing bath. Subsequently, it was oxidized in 100 mL of distilled water under vigorous stirring for a few minutes. The absorbance of the oxidized leuco-indigo bath before and after dyeing was measured using a UV-visible spectrophotometer (Shimadzu, Japan). The bath exhaustion percentage (E %) was calculated using the following equation [21]:

$$E(\%) = \frac{(A_0 - A_r)}{A_0} \cdot 100 \tag{7}$$

where, A_0 and A_r represent the absorbance of the oxidized leuco-indigo bath before and after dyeing, respectively.

Evaluation of dyeing fastnesses

The dyeing fastness to washing, rubbing, and light of the various samples dyed with indigo was evaluated according to the following ISO standards respectively: ISO 105- C06, ISO 105- X12, and ISO 105-B02.

Environmental evaluation of the residual dyeing baths

The residual dyeing bath was assessed by measuring the chemical oxygen demand (COD), the biological oxygen demand (BOD), and the pH of the dyeing bath. The (COD) in the dyebath after dyeing was assessed conforming to the method described by *Harrelkas* [22]. This method involves the chemical oxidation of the reducing substances in water using an excess of potassium dichromate $K_2Cr_2O_7$ in a sulfuric medium. The (*COD*) measurement implies titrating the excess potassium dichromate with a reducing agent, ammonium iron(II) sulfate. Initially, 2.5mL of the sample under analysis was introduced into a digestion tube following agitation. Subsequently, 1.5 mL of digestion solution (consisting of 12.25 $g \cdot L^{-1}$ potassium dichromate dried for 2 hours at 105°C, 33.3 $g \cdot L^{-1}$ mercury sulfate, and 167 mL sulfuric acid in 1L distilled water) and 3.5mL catalyst solution (8.8 $g \cdot L^{-1}$ silver sulfate in 1L sulfuric acid) are added to the digestion tube. The sealed tubes were then subjected to a temperature of 148 °C in a reactor for 2 hours. Following cooling, the contents of the tubes were poured into a 50 mL Erlenmeyer flask and the volume was made up to 25 mL. A few drops of feroin (color indicator) were added, and titration was carried out using 0.12M Mohr's salt solution. Additionally, a blank was prepared using 2.5 mL of distilled water following the same procedure. The *COD* of the analyzed samples is expressed in mg O_2/ L and it is equal to:

$$COD = 8000 \cdot CX \frac{(VB - VE)}{V} \tag{8}$$

where *VB* is the volume of Mohr's salt poured to determine the blank solution; *VE* is the volume of Mohr's Salt poured to determine the sample, C=0.12M, and V is the volume of the sample [23].

To determine the biological oxygen demand (BOD)$_5$, dissolved oxygen (*DO*) was measured before and after 5 days of culture in a *BOD* incubator at 26 °C. Oxygen consumption was followed for 5 days. This parameter is transformed by the atmospheric pressure drop. The (BOD)$_5$ is thus equal to:

$$(BOD)_5 = (P_0 - P_5) \cdot F \tag{9}$$

P_0: is the O_2 concentration in the solution at the beginning of the assay; P_5 is the O_2 concentration in the solution at the end of the assay (after 5 days); and F=10 is the dilution factor.

Statistical analysis and process optimization

A full-factorial experimental design with three factors and three levels was implemented to model and optimize the dyeing process. This experimental design allows us to study the influence of the experimental parameters (iron (II) gluconate concentration, reduction temperature, and alkali concentration) and to optimize the dyeing process. The input parameters and their levels are represented in Table S1 (Supplementary material). All reduction experiments were performed using 2 $g \cdot L^{-1}$ of indigo for 2h. Analysis of variance (ANOVA) was performed, and the P-value was used to demonstrate the significance of each parameter [24]. The analyzed responses are the redox potential and color strength (*K/S*) of the dyed samples. The experimental design, along with different experiments and responses, is displayed in Table S2.

RESULTS AND DISCUSSION

DFT study of iron(II) gluconate and indigo

Prediction of global reactivity descriptors for iron(II) gluconate and indigo

According to the frontier molecular orbital theory (FMO) of chemical reactivity, the transition of an electron occurs through the interaction between the highest occupied molecular orbital (HOMO) and the lowest unoccupied molecular orbital (LUMO) of the reacting species [25]. The HOMO and LUMO energies of both iron (II) gluconate and indigo were calculated by the functional/standard basis set B3LYP/6-311G(d,p). Global reactivity descriptors of iron (II) gluconate and indigo such as ionization energy (*IE*), electron affinity (*EA*), electronegativity (χ), chemical hardness (η), chemical softness (S), chemical potential values (μ) and electrophilicity index (ω) were determined based on gas-phase optimization. These numerical parameters, which are mainly calculated from HOMO and LUMO energies, are summarized in Table 1.

Table 1. The optimized calculations of global reactivity descriptors for iron (II) gluconate and indigo at B3LYP/6-311G(d,p) (level of theory).

Reactivity descriptors (eV)	Iron (II) gluconate	Indigo
E_{HOMO}	-6.19	-5.52
E_{LUMO}	-1.73	-3.21
Ionization energy (IE)	6.19	5.52
Electron affinity (EA)	1.73	3.21
Electronegativity (χ)	-3.96	- 4.37
energy gap	4.45	2.31
Hardness (η)	2.23	1.16
Softness (S)	0.224	0.58
Chemical potential (μ)	3.96	4.37
Electrophilicity index (ω)	3.52	8.25

E_{HOMO}, a quantum chemical parameter, is commonly linked to the electron-donating capability of a molecule. The high-value E_{HOMO} value suggests that the molecule is more inclined to donate electrons to a suitable acceptor molecule of low empty molecular orbital [26]. Referring to Table 1, it can be noted that iron(II) gluconate has a higher E_{HOMO} absolute value compared to the E_{LUMO} absolute value of indigo indicating a favorable energy difference for electron transfer from iron(II) gluconate to indigo. This result highlights the capacity of iron(II) gluconate to donate electrons to indigo.

The global properties that are very useful in evaluating molecular stability and reactivity are hardness and softness. A molecule is considered hard when it possesses a large energy gap, whereas a soft molecule is characterized by a smaller energy gap [27]. The molecule iron (II) gluconate has a very high hardness of 2.23 (ev) and a very low softness of 0.224 (ev) due to the high energy gap. Consequently, the molecule is demonstrated to be extremely stable, displaying low chemical reactivity and high kinetic stability.

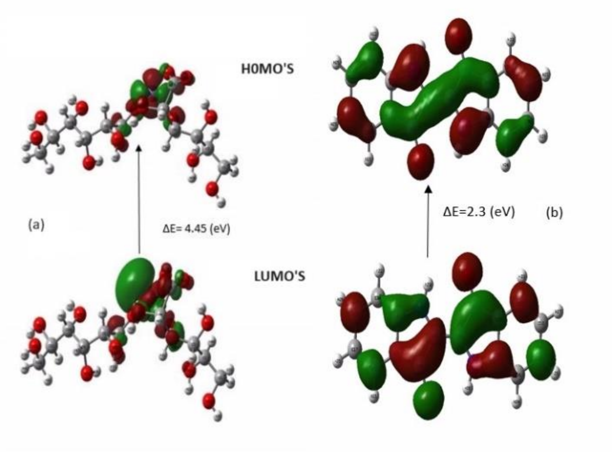

Figure 1. LUMO-HOMO energy gap at B3LYP/6-311 (level of theory) for (a) iron (II) gluconate and (b) indigo.

Local chemical activity calculations: Molecular Electrostatic Potential (MEP)

Electrophilic nature, nucleophilic reactions, and hydrogen bond interactions can be elucidated through the molecular electrostatic potential, which is associated with electron density. Molecular electrostatic potential surfaces are visually depicted using color codes, where red signifies the most negative regions indicative of electrophilic reactions. Conversely, blue and green indicate the most positive regions, representing nucleophilic dominant regions [28–30]. The total electron density surface of iron (II) gluconate is given in Figure 2. This figure illustrates that in iron(II) gluconate, most positive charges are concentrated around the iron atom, defining potential nucleophilic reactions, while the most negative charges are localized around the oxygen atoms. These regions indicate a higher electron density, suggesting that they are more likely to donate electrons. Thus, iron(II) gluconate may act as a potential reducing agent for indigo.

Study of the dyeing process

Effect of the reduction temperature

The evolution of the redox potential and color strength of the dyed samples as a function of reduction temperature is presented in Figure 3a. This figure shows that increasing the temperature from 50 to 75 °C improves the reducing power and color strength. This result can be attributed to the fact that increasing the temperature promotes molecular agitation and leads to a better reduction of the dye. Therefore, a higher concentration of leuco-indigo is adsorbed on the fabric. Above this temperature, a slight decrease in the reducing power and color strength is observed. This result could be explained by the fact that higher temperatures may reduce the yield of indigo reduction while simultaneously increasing the hydrolysis reaction, which can negatively impact the dyeing process [11].

Effect of iron (II) gluconate concentration

The concentration of iron (II) gluconate varied from 2 to 25 $g \cdot L^{-1}$, and the evolution of redox potential and color strength were studied. As shown in Figure 3b for concentrations below 18 $g \cdot L^{-1}$, the redox potential gradually decreases, reaching a minimum value of -745 mV and color strength increases to a maximum value of 19.2. This result can be attributed to the fact that increasing the leuco-indigo concentration leads to an increase in the absorption into the fiber. While exceeding a concentration of 18 $g \cdot L^{-1}$, the redox potential and color strength remained almost constant, indicating that the maximum concentration of leuco-indigo was probably reached.

Effect of sodium hydroxide concentration

The influence of sodium hydroxide concentration on the redox potential and color strength of the dyed samples is presented in Figure 3c. The obtained curves show that at a sodium hydroxide concentration of 20 $g \cdot L^{-1}$, the redox potential decreases until it reaches a value of -671 mV and color strength increases to reach a value of 13.5. This result can be accounted for by the fact that raising the sodium hydroxide concentration in the medium promotes the leuco-indigo formation, generates more negative redox potential values, and increases the dye uptake by the fibers. Above a concentration of 20 $g \cdot L^{-1}$, an increase in the

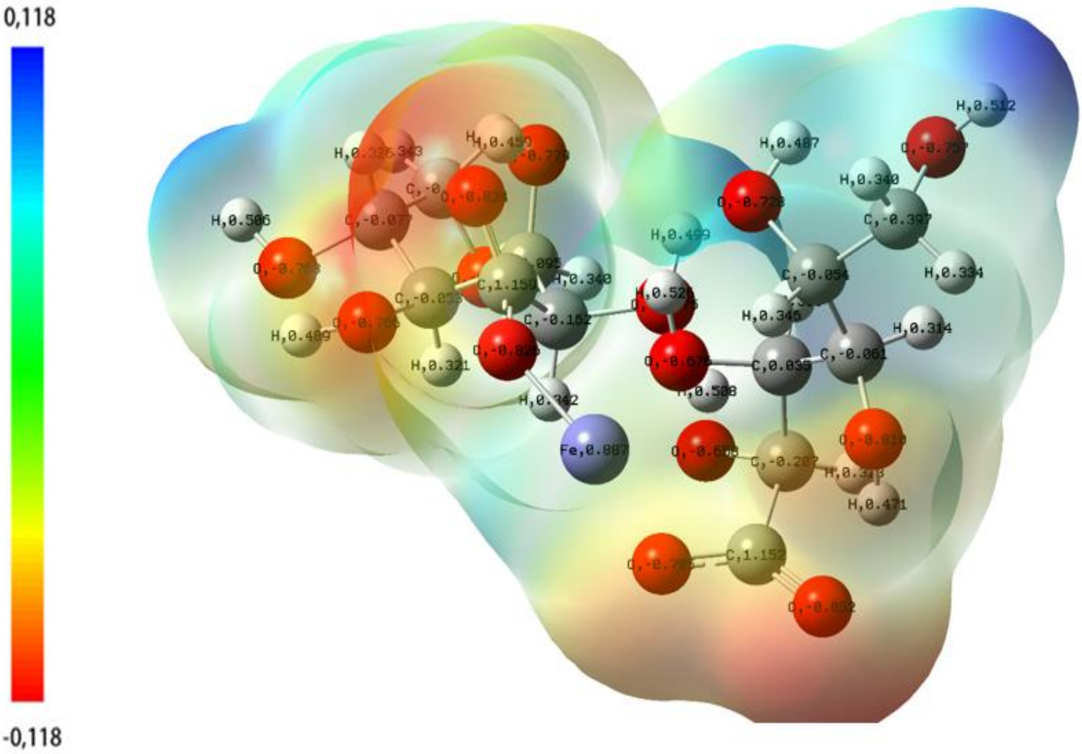

Figure 2. The total electron density surface of iron (II) gluconate.

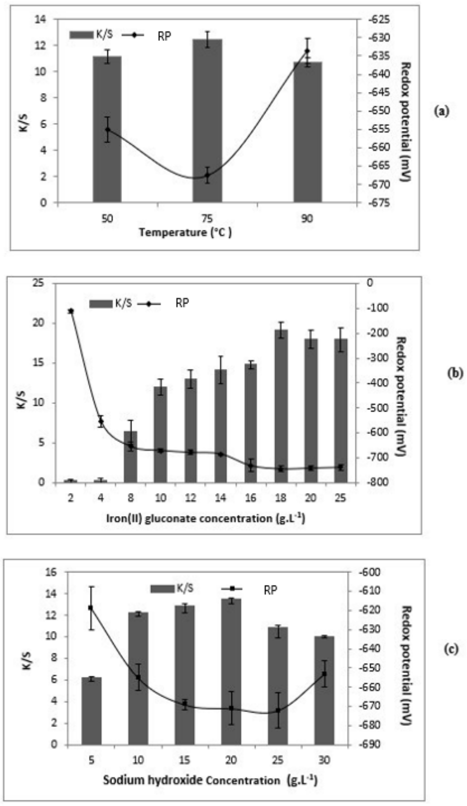

Figure 3. Evolution of the redox potential RP(mV) and color strength K/S as a function of (a) reduction temperature, (b) iron (II) gluconate concentration, and (c) alkali concentration. (RP and K/S values given as mean and standard deviation of three measurements).

redox potential and a drop in the color strength are observed. This result is probably due to an over-reduction of indigo. Therefore, a sodium hydroxide concentration between 15 and 20 g·L^{-1} is sufficient to achieve the optimum dyeing quality.

Optimization of the dyeing process

Statistical analysis and optimization of the experimental data were carried out using the software (Minitab Ver. 17.0, USA). The determination of the regression model, the main effects, and the interactions between factors were performed.

Establishment of models

An analysis of the regression equation determines the relationship between the responses and the various factors. By taking into account the detected effects (linear, quadratic) and interactions, this feature allows the adjustment of the model. The experimental analysis leads to the regression coefficients for the redox potential and color strength (Tables S3 and S4). The assessment was based on the *P*-value (Fisher coefficient) of each parameter. This coefficient is used to identify the significance of each parameter. In general, a factor is considered significant if it has a *P* value <0.05. The quadratic analysis of the two responses leads to the following regression equations.

$$\begin{aligned} PR &= -422.674 - 4.0313 \cdot S(g/L) - 7.13304 \cdot \mathrm{Red}(g/L) \\ &+ 0.1564 \cdot S^2(g/L) - 0.2456 \cdot S(g/L) \cdot \mathrm{Red}(g/L) \end{aligned} \quad (11)$$

with R^2=93.4%.

$$\begin{aligned} K/S &= -34.3275 + 0.7764 \cdot S(g/L) + 3.1859 \cdot \mathrm{Red}(g/L) \\ &- 0.0258 \cdot S^2(g/L) \end{aligned} \quad (12)$$

with R^2=94.1%.

For both redox potential and color strength, high determination coefficients R^2 were obtained. Therefore the models correctly estimated the geometrical deviations according to the three selected factors and their interactions.

Principal effects of the experimental parameters

The influence of the factors on the color strength and redox potential was determined using main effect diagrams (Figure 4a). Based on this figure, it can be noted that the reducing agent concentration and the sodium hydroxide concentration have the highest effect on both the redox potential and color strength. It can also be noted that a reduction in temperature has a less important effect on both responses. The optimal reduction temperature is 75° C. If the temperature exceeds this level, the color strength decreases rapidly.

Analysis of interaction graphs

Figure 4b represents the interaction plots between the studied parameters (iron (II) gluconate concentration, reduction temperature, and sodium hydroxide concentration). This figure shows that there is no interaction between the different studied factors for color strength. The plot for the redox potential shows an interaction between the iron (II) gluconate concentration and the alkali concentration. This relation can be interpreted by the fact that the indigo reduction requires the formation of a certain amount of iron (II) hydroxide, resulting from the reaction of sodium hydroxide with iron (II) gluconate. In addition, this graph indicates that there is no interaction between the reducing agent concentration and temperature, and between the alkali concentration and temperature.

Contour plots analysis

Contour graphs give an idea about the zones that can maximize the response value when combining two input parameters. Contour plots of color strength and redox potential are given in Figure 4c. This figure reveals the regions of maximum color strength (*K/S*>15). These areas are shown in dark green. As shown in Figure 4c, the lowest redox potential values (between -660 mV and -680 mV) were obtained at high reducing agent and sodium hydroxide concentrations.

Optimization of the reduction process

The optimum reduction conditions are shown in Table 2. To confirm the theoretical value reported by the Minitab software, the dyeing experiment under these optimum conditions was repeated three times. An average value of 20.1± 0.36 was obtained. Hence, the validation of the optimal conditions.

Table 2. Optimal conditions proposed by the Box-Benken design.

Red(g·L^{-1})	S (g·L^{-1})	T(C°)	K/S (theoretical)
20	20	75	20

Evaluation of the dyeing performance

To evaluate the potential use of the optimized process using iron (II) gluconate as a replacement for the conventional process using sodium dithionite, a comparative analysis involving the measurement of redox potential, color strength of the indigo dyed samples, dyeing fastness and bath exhaustion percentage was conducted. The results are shown in Table 3, with each value in the table representing the mean value of three experiments. This table reveals that iron (II) gluconate exhibits a redox potential slightly higher than that obtained with sodium dithionite. Moreover, despite its higher redox potential, the

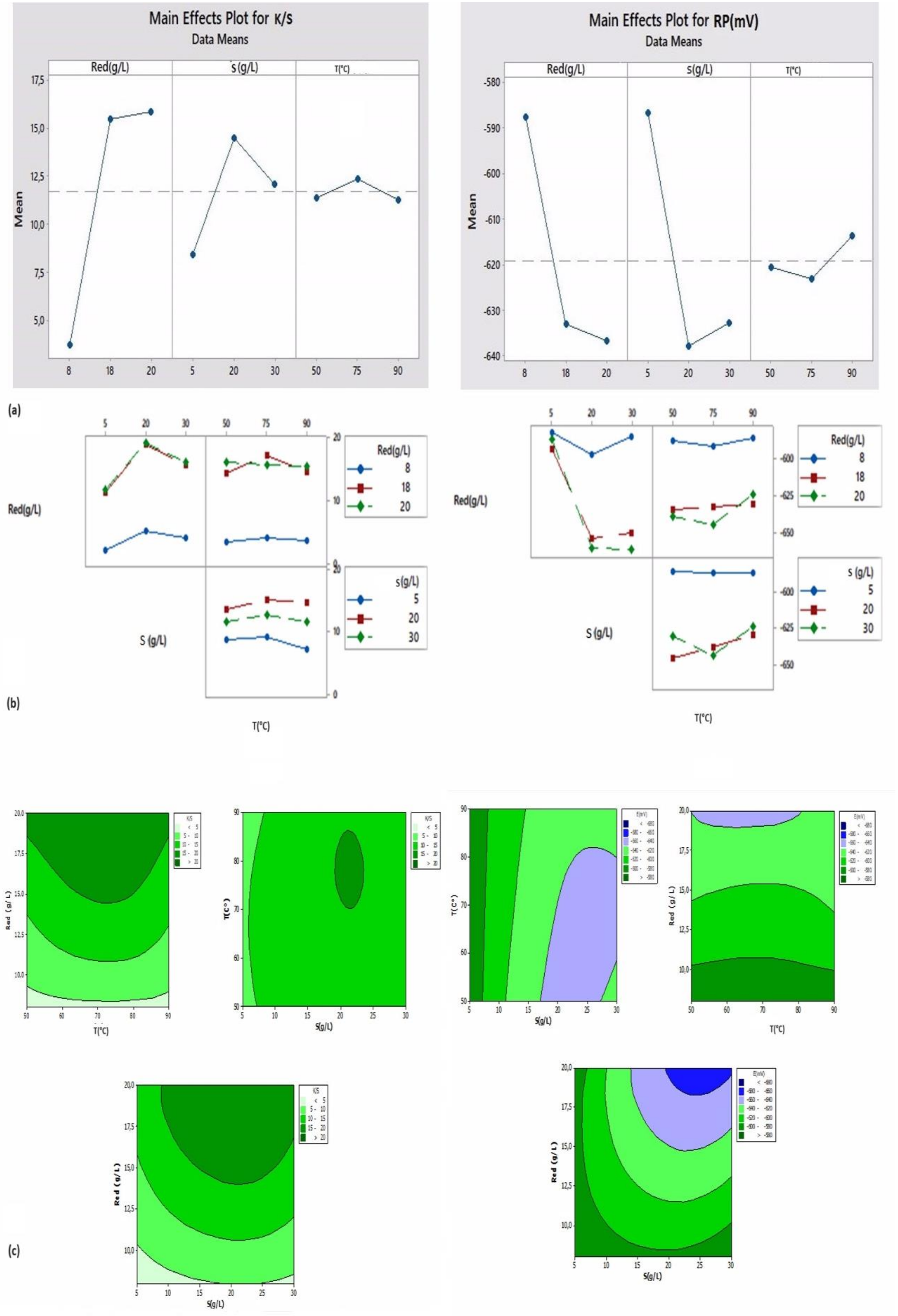

Figure 4. (a) Main effects plots, (b) Interaction diagrams, and (c) Contour graphs for the color strength of the indigo-dyed samples and the redox potential.

process using iron (II) gluconate as a reducing agent demonstrates superior performance in dyeing processes compared to the reference dyeings with sodium dithionite. Notably, it yields higher color strength, exhaustion percentage, and dyeing fastness indicating its effectiveness in the dyeing process. This result could be explained by the presence of iron (II) in the dye bath, which acts as a mordant that establishes chemical bonds between the fiber and the dye via the metal, subsequently darkening the shades and improving dyeing fastness.

Table 3. Comparison of dyeing performance of the processes using sodium dithionite and iron (II) gluconate.

Systems	Fastness properties			Light	RP(mV)	K/S	E(%)
	Washing	Rubbing					
		Dry	Wet				
Iron (II) gluconate	4	5	4	7	-730	20	23.7
Sodium dithionite	4	4	1-2	5	-780	17	18

Environmental assessment of residual dye baths

The residual bath of the indigo dyeing process using iron (II) gluconate as a reductant was evaluated. The indigo reduction was carried out under optimum conditions. The effluent quality was compared to that of the standard process using sodium dithionite. Table 4 summarizes the parameters measured for the residual bath in both processes. The obtained results show that the effluent from the conventional process presents a COD/BOD_5 ratio of about 6, which indicates that this effluent is highly polluting and hardly biodegradable. On the other hand, the substitution of sodium dithionite by iron (II) gluconate allows the reduction of this ratio and therefore reduces the wastewater pollution generated by the classical process. These effluents will then be subjected to wastewater treatment. In the case of reduced indigo by iron (II) gluconate, the free iron(II) hydroxide is transformed by oxidation into $Fe(OH)_3$, which behaves as a flocculant and leads to a reduction of the chemical oxygen demand (*COD*).

Table 4 Environmental evaluation of the dyeing processes.

Reducing agents	pH	COD ($mgO_2.L^{-1}$)	BOD $_5$ ($mgO_2.L^{-1}$)	COD/BOD_5
Sodium dithionite	12.17	12462	2036	6.12
Iron (II) Gluconate	12.23	5120	2300	2.22

CONCLUSION

This research work reports the usage of iron (II) gluconate as a reductant in the indigo dyeing process. A brief examination of the electron donor-acceptor character and the polarizability of iron(II) gluconate and indigo was carried out using the DFT/B3LYP under a 6-311 G(d,p) basis set. The global reactivity descriptors prove that the iron (II) gluconate molecule is very stable with high hardness, low softness, and a large energy gap. A full factorial experimental design revealed that an iron (II) gluconate concentration of 20 g·L^{-1}, a sodium hydroxide concentration of 20 g·L^{-1}, and a temperature of 75 °C were the optimal dyeing parameters to attain maximal color strength. The evaluation of residual dyeing baths confirmed the potential of the process using iron (II) gluconate to reduce wastewater pollution. Furthermore, following the reduction process, iron (II) gluconate will be transformed into its ferric form, offering the additional benefit of being applicable as coagulants in subsequent waste treatment procedures. Finally, the dyeing process proposed in this study offers denim fabric manufacturers the opportunity to reduce the environmental impact of denim dyeing while attaining satisfactory dyeing performance at reasonable costs.

REFERENCES

[1] L. Xiaoyan, K. Wang, M. Wang, W. Zhang, J. Yao, S. Komarneni, J. Clean. Prod. 276 (2020) 123251. https://doi.org/10.1016/j.jclepro.2020.123251.

[2] T. M. Hsu, D.H. Welner, Z.N. Russ, B. Cervantes, R. L. Prathuri, P. D. Adams, J. E. Dueber, Nat. Chem. Biol. 24 (2018) 256–261. https://doi.org/10.1038/nchembio.2552.

[3] X.Y. Wang, S.C. Sevov, Chem. Mater. 19 (2007) 4906–4912. https://doi.org/10.1021/cm071480x.

[4] M. Abdelileh, A.P. Manian, D. Rhomberg, M. Ben Ticha, N. Meksi, N. Aguiló-Aguayo, T. Bechtold, J. Clean. Prod. 266 (2020) 121753. https://doi.org/10.1016/j.jclepro.2020.121753.

[5] T. Bechtold, E. Burtscher, A. Turcanu, O. Bobleter, Text. Res. J. 67 (1997) 635–642. https://doi.org/10.1177/004051759706700902.

[6] T. Bechtold, A. Turcanu, J. Appl. Electrochem. 34 (2004) 1221–1227. https://doi.org/10.1007/s10800-004-1707-z.

[7] A. Turcanu, C. Fitz-Binder, T. Bechtold, J. Electroanal. Chem. 654 (2011) 29–37. https://doi.org/10.1016/j.jelechem.2011.01.040.

[8] C. Yi, X. Tan, B. Bie, H. Ma, H. Yi, Sci. Rep. 10 (2020) 4927–4928. https://doi.org/10.1038/s41598-020-61795-5de.

[9] Y. Changhai, T. Xiaodong, Z. Yang, X. Jie, Z. Hantao, L. Xueding, Z. Danying, H.Ping, Z. Jin, (Wuhan Textile University), CN201710044213.8A (2017).

[10] L. Xiaoyan, W. MengQian, W. Gang, Y. Jiming, Pigm.

Resin. Technol, 50 (2021) 185–193. http://dx.doi.org/10.1108/PRT-04-2020-0035.

[11] N. Meksi, M. Kechida, F. Mhenni, Chem. Eng. J. 131 (2007) 187–193. https://doi.org/10.1016/j.cej.2007.01.001.

[12] N. Meksi, M. Ben Ticha, M. Kechida, M.F. Mhenni, Chem. Res. 49 (2010) 12333–12338. https://doi.org/10.1021/ie100974.

[13] N. Meksi, M. Ben Ticha, M. Kechida, M.F. Mhenni, J. Clean. Prod. 24 (2012) 149–158. https://doi.org/10.1016/j.jclepro.2011.11.062.

[14] J.N. Chakraborty, R.B. Chavan, AATCC Rev. 4 (2004) 17–20. https://www.researchgate.net/publication/290277788_Dyeing_of_cotton_with_vat_dyes_using_ironII_salt_complexes.

[15] J.N. Chakraborty, M. Das, R.B. Chavan, Melliand Int. 12 (2005) 319–323. https://www.researchgate.net/publication/290652040_Kinetics_of_dyeing_and_properties_of_ironII_salt_complexes_for_reduction_of_vat_dyes.

[16] R.B. Chavan, J.N. Chakraborty, Color. Technol. 117 (2001) 88–94. https://doi.org/10.1111/j.1478-4408.2001.tb00340.x.

[17] T. Koopmans, Physica 1 (1933) 104–113. https://doi.org/10.1016/S0031-8914(34)90011-2.

[18] V.C. Mudnoor, J.N. Chakraborty, Fibers Polym. 21 (2020) 1061–1070. https://doi.org/10.1007/s12221-020-9247-7.

[19] J.H. Xin, C.L. Chong, T. Tu, Color. Technol. 116 (2000) 260–265. https://doi.org/10.1111/j.1478-4408.2000.tb00044.x.

[20] P. Kubelka, F. Munk, Zh. Tekh. Fiz. 12 (1931) 593–601. https://www.graphics.cornell.edu/~westin/pubs/kubelka.pdf.

[21] M. Ben Ticha, N. Meksi, N. Drira, M. Kechida, M.F. Mhenni, Ind. Crops. Prod. 46 (2013) 350–358. https://doi.org/10.1016/j.indcrop.2013.02.009.

[22] F. Harrlekas, Doctoral thesis, Institut National Polytechnique de Lorraine (2008). https://hal.univ-lorraine.fr/tel-01752986/document.

[23] J. Rodier, C. Bazin, J. Broutin, P. Chambon, H. Champsaur, L. Rodi, L'analyse de l'eau: Eaux naturelles eaux résiduaires eaux de mer, Dunod, Paris (1996), p.1384. ISBN: 978-2-10-002416-2.

[24] M.E.R. Carmona, M.A.P. Da Silva, S.G.F. Leite, Process Biochem. 40 (2005) 779–788. http://doi.org/10.1016/j.procbio.2004.02.024.

[25] A.Y. Musa, A.H. Kadhum, A.B. Mohamad, A.A. Rahoma, H. Mesmari, J. Mol. Struct. 969 (2010) 233–237. http://doi.org/10.1016/j.molstruc.2010.02.051.

[26] G. Gece, S. Bilgic, Corros. Sci. 51 (2009) 1876–1878. https://doi.org/10.1016/j.corsci.2009.04.003.

[27] I.B. Obot, N.O. Obi-Egbedi, S.A. Umoren, Int. J. Electrochem. Sci. 4 (2009) 863–877. https://www.researchgate.net/publication/261725755_Adsorption_Characteristics_and_Corrosion_Inhibitive_Properties_of_Clotrimazole_for_Aluminium_Corrosion_in_Hydrochloric_Acid.

[28] K. Sayin, D. Karakaş, N. Karakuş, T.A. Sayin, Z. Zaim, S.E. Kariper, Polyhedron 90 (2015) 139–146. https://doi.org/10.1016/j.poly.2015.01.047.

[29] K. Fukui, Science 218 (1982) 747–754. https://www.science.org/doi/10.1126/science.218.4574.747.

[30] T. Karakurt, M. Dinçer, A. Çukurovalı, I. Yılmaz, J. Mol. Struct. 991 (2011) 186–201. https://doi.org/10.1016/j.molstruc.2012.05.022.

MAHA ABDELILEH[1,2]
MANEL BEN TICHA[3]
NIZAR MEKSI[1,2]
HATEM DHAOUADI[1]

[1]University of Monastir, Faculty of Sciences of Monastir, Research Laboratory of Environmental Chemistry and Clean Processes, Monastir, Tunisia

[2]University of Monastir, National Engineering School of Monastir, Department of Textile, Monastir, Tunisia

[3]Department of Early Childhood, University College of Turabah, Taif University, Taif, Saudi Arabia

NAUČNI RAD

EKOLOŠKI PRIHVATLJIV PROCES BOJENJA INDIGOM SA GVOŽĐE(II)-GLUKONATOM KAO REDUKCIONIM SREDSTVOM

Cilj ovog rada je zamena ekološki štetnog natrijum-ditionita, koji se tradicionalno koristi u procesu bojenja indigom, redukujućim agensom gvožđa(II)-glukonata. Za određivanje optimizovanih struktura gvožđe(II)-glukonata i indiga korišćena je teorija funkcionalne gustine (DFT) sa osnovnim skupom B3LIP 6-311 G. Izračunate su energije najveće zauzeta i najniže nezauzeta molekulskeorbitale i određena su elektronska svojstva zavisna od njih. Dalje, proučavan je ekološki proces bojenja korišćenjem ovog redukcionog sredstva. Merenjem dobijenog redoks potencijala i jačine boje obojenih uzoraka ispitan je uticaj alkalnosti, temperature redukcije i koncentracije gvožđe(II)-glukonata na ispunjenje procesa bojenja. Za statističku analizu i optimizaciju procesa bojenja izveden je pun faktorijalni eksperiment. Rezultati su otkrili da je razvijena metoda visoko efikasna i sposobna da generiše redoks potencijal i kvalitet bojenja uporediv sa onima dobijenim konvencionalnim postupkom koji koristi natrijum-ditionit. Konačno, zamena natrijum ditionita za gvožđe(II)-glukonat smanjila je opterećenje otpadne vode koje nastaje konvencionalnim procesom bojenja.

Ključne reči: indigo bojenje; teorija funkcionalne gustine; ekološki proces; gvožđe (II) glukonat; optimizacija procesa.

CI&CEQ
Chemical Industry & Chemical Engineering Quarterly

Available online at
Association of the Chemical Engineers of Serbia *AChE*
www.ache.org.rs/CICEQ

Chem. Ind. Chem. Eng. Q. 31 (2) 151–161 (2025) CI&CEQ

NAGARAJAN GNANAVEL[1]
SUNDARRAJ MARIADOSS[1]
VENKATESAN JAYAVELU[2]
VENKATA MOHANREDDY POLAKA[3]
MUTHUCUMARASWAMY RAJAMANICKAM[4]

[1]Department of Mathematics, Panimalar Engineering College, Poonamallee, Chennai, Tamil Nadu, India

[2]Department of Mathematics, Rajalakshmi Engineering College, Thandalam, Chennai, Tamil Nadu, India

[3]Department of Mathematics, Saveetha School of Engineering, Saveetha Institute of Medical and Technical Sciences, Saveetha University, Chennai, Tamil Nadu, India

[4]Department of Applied Mathematics, Sri Venkateswara College of Engineering, Sriperumbudur, Tamil Nadu, India

SCIENTIFIC PAPER

UDC 66:66.021.3:542.9:544

CHEMICAL PROCESS EFFECTS ON A SLOPED SURFACE WITH CHANGING MASS AND CONSISTENT TEMPERATURE

Article Highlights

- Velocity escalates during generative reactions but diminishes during destructive reactions
- Chemical reaction parameter decrease correlated with increased velocity
- Variables relate to local skin friction, impacting frictional forces over time
- Sherwood number ties to material transmission, shaping dynamics over time
- The dimensionless governing equations were tackled using the Laplace transform method

Abstract

The research extensively investigated the turbulent flow patterns surrounding an unbounded inclined plate under the conditions of uniform temperature and variable mass dispersion. Throughout this analysis, the study thoroughly considered the impact of chemical reactions within the system. Focusing on the harmonic inclination of the plate within its plane, the study employed the Laplace Transform approach to accurately solve the non-dimensional governing equations. In scrutinizing various profiles, the investigation examined the impact of several crucial physical factors: chemical response variable, Schmidt number, thermal Grashof number, mass Grashof number, and duration. This study delves into the intricate influence of various factors on the complex flow dynamics surrounding inclined plates, specifically focusing on heat and mass transfer phenomena. By examining these relationships, the research provides crucial insights into improving the efficiency of thermal and mass transmission processes within systems that incorporate tilted surfaces. Moreover, this knowledge can potentially contribute to advancements in various fields, from renewable energy systems to manufacturing processes, where heat and mass transfer play pivotal roles.

Keywords: tilted surface; thermal transfer; mass transmission; chemical reaction; Laplace transform method.

In numerous industrial and engineering contexts, the utilization of synthetic response impacts on a continuously propelled inclined surface characterized by variable material dispersion and uniform temperature can be advantageous. Chemical Vapor Deposition (CVD) is extensively used in semiconductor manufacturing whose process involves the deposition of thin films on substrates. By comprehending the synthetic response influences on an inclined surface characterized by varying material dispersion, the CVD process can be optimized to produce films of higher quality and greater uniformity. In the pharmaceutical industry and drug manufacturing, certain reactions require precise control of temperature and mass

---

Correspondence: M. Sundar Raj, Department of Mathematics, Panimalar Engineering College, Poonamallee, Chennai 600123, Tamil Nadu, India.
E-mail: sundarrajkani@gmail.com
Paper received: 12 December, 2023
Paper revised: 30 May, 2024
Paper accepted: 13 june, 2024

https://doi.org/10.2298/CICEQ231212023G

diffusion. The study of chemical reactions on an inclined plate can contribute to optimizing reaction conditions for pharmaceutical synthesis. The design of chemical reactors involves controlling temperature gradients and mass diffusion for efficient chemical transformations. Chemical reactions occurring on a slanted surface with changeable material dispersion may yield information that can be utilized to improve reactor design. In surface coating processes industries such as automotive or aerospace, the coating processes are crucial. Understanding how chemical reactions affect the coating on a linearly accelerated inclined plate can enhance the quality and durability of the coatings.

The environmental engineering studies of chemical reactions on an inclined plate have many applications, particularly in processes related to air and water purification. This knowledge can aid in designing efficient systems for pollutant removal. Food processing applications involving certain processing techniques involve chemical reactions. For example, understanding the effects of an inclined plate can contribute to optimizing processes like drying or frying in the food industry. Chemical reactions occur at the electrode surfaces in energy storage systems in the development of batteries or fuel cells. Research on inclined plates can provide insights into optimizing reaction conditions for improved energy storage and conversion efficiency. Understanding the chemical reactions on an inclined plate is relevant to material synthesis. This knowledge can be applied to develop advanced materials with tailored properties for specific applications, such as in the aerospace or electronics industry. The study of chemical reactions on inclined plates can have applications in areas such as drug delivery systems or bioengineering processes in biomedical applications and medical research. Also, the chemical reactions on inclined plates can be relevant in designing systems for treating industrial waste and optimizing the removal of pollutants through controlled reactions.

Bég *et al.* [1] examined numerical methods that accounted for the Soret and Dufour influences in mixed convective conditions while investigating heat and mass transfer in dynamically reactive flows along angled as well as perpendicular surfaces. Using magnetohydrodynamics (MHD), Orhan Aydm and Ahmet Kaya [2] examined the combined convection thermal flow surrounding an angled surface. The influence of magnetohydrodynamics (MHD) on a vertically oscillating plate during a 1st level synthetic response was investigated by Muthucumaraswamy *et al.* [3]. In a study by Muthucumaraswamy [4], the examination focused on the impacts of chemical reactions on fluid flow over a vertical plate that oscillates while maintaining uniform mass diffusion at different temperature levels. Bisht *et al.* [5] examined the impact of elemental responses and varying heat conductance on the outer region movement of constant combined convective flows, which involved thermal as well as material transmission inside a tapered shape and was propelled by an area basin. The investigation carried out by Sundar Raj *et al.* [6] analyzed magnetohydrodynamic convective flow around an accelerated, isothermal vertical plate featuring variable mass diffusion. Makinde [7] conducted an in-depth investigation into the vacillating circulation of radiating liquid undergoing chemical reactions and subjected to hydromagnetic influences. The study focused on the fluid dynamics around a perpendicular exterior with consistent thermal fluctuation. Puneet Rana *et al.* [8] examined a mathematical model for the combined convective barrier layered movement of a minuscule level liquid across a permeable intermediate-positioned slanted surface. The investigation probed the intricacies of heat and mass transfer phenomena. Mohammad Shah Alam *et al.* [9] conducted an extensive study on the HMT phenomena in magnetohydrodynamic unrestricted convection circulation across a tilted surface, incorporating the influence of Hall current. The research aimed to unravel the intricacies of the thermal and mass transport characteristics in this specific configuration. Muthucumaraswamy and Jeyanthi [10] conducted an extensive study on the Hall effects influencing the magnetohydrodynamic (MHD) flow over an infinite vertical plate. This investigation involved a rotating fluid with variable temperature and mass diffusion, along with the inclusion of a first-order chemical reaction.

Narahari *et al.* [11] explored the intricate dynamics of unsteady magnetohydrodynamic unrestricted convective circulation across a boundless tilted surface. The investigation considered the impact of sloped circumstances and incorporated emission, thermal origins, and synthetic responses. The research aimed to provide a comprehensive understanding of the total influences of these parameters on the circulation factors and HMT phenomena. Mondal *et al.* [12] delved into the intricate aspects of magnetohydrodynamic combined convective material transmission across a tilted surface. Inconsistent thermal factors and the impact of synthetic responses were taken into consideration in the study. The primary objective of the study was to attain an in-depth knowledge of the intricate relationship among these phenomena and how they impact the processes of material transmission across the tilted surface. Farjana *et al.* [13] presented a numerical investigation of boundary layer mass transfer flow over an inclined plate, considering the effects of chemical reaction and thermal diffusion. An analysis of unsteady MHD free convection flow oriented heat and mass transfer past an exponentially accelerated inclined plate embedded in a saturated porous medium with uniform permeability, variable temperature, and concentration has been studied by Rani Pattnaik *et al.*[14]

Khalid *et al.* [15] conducted an investigation into the merged influences of buoyancy along with synthetic responses on the magnetohydrodynamic flow of Casson liquids across a permeable context. The study focused on the flow dynamics induced by a porous shrinking sheet. The research enabled an understanding of the interactions between buoyancy, chemical reactions, and the unique characteristics of Casson fluids near a permeable shrinking sheet. Sailaja *et al.* [16] analyzed the influence of twin divergent influences in magnetohydrodynamic combined convective flow across a perpendicular tilted surface. The study considered the existence of a permeable environment and incorporated the Biot number as a parameter. The research employed a finite element technique to analyze the complex interactions within this system. The aim was to gain a comprehensive understanding of the impact of double diffusive effects on the flow dynamics of specific liquids near a permeable environment and a vertically inclined plate considering numerous factors.

Dhal *et al.* [17] explored the impacts of HMT on magnetohydrodynamic unrestricted convective circulation across a tilted and numerically expedited surface fixed in a permeable environment having a thermal intake. The study aimed to understand the complex interactions between HMT phenomena near MHD effects, an inclined plate, exponential acceleration, and a permeable environment with a heat source. Rajput and Gaurav Kumar [18] investigated the influence of element responses on the unstable magnetohydrodynamic circulation across a uniform expedited tilted surface. The study considered varying degrees, material dispersion, etc. The research aimed to comprehensively understand the influence of chemical reactions on the circulation dynamics amidst varying temperatures, mass diffusion, and Hall current. Suman Agarwalla and Nazibuddin Ahmed [19] conducted a study on the magnetohydrodynamic material transmission circulation across a tilted surface having varying temperatures as well as surface pace. The investigation considered the plate to be fixed in a permeable environment. The research aimed to gain insights into the complex interactions of MHD effects, mass transfer, variable temperature, plate velocity, and the impact of a permeable environment on the circulation characteristics around the inclined plate. Hiranmoy Mondal *et al.* [20] initiated a comprehensive investigation on the influence of thermal parameters in a magnetohydrodynamic mixed convective material transmission across a tilted surface. The research incorporated inconsistent thermal impacts and considered the influence of chemical reactions. The study aimed to provide a comprehensive understanding of the intricate interplay between thermophoresis, and Soret-Dufour effects on the material transmission parameters over the inclined plate. Ahmad *et al.* [21] conducted a proportional investigation of the unrestricted convective circulation of magnetohydrodynamic liquid. The investigation considered a heat source and a 1st level synthetic response. The research aimed to comprehensively analyze and compare the dynamics of natural convection in non-Newtonian fluids influenced by MHD effects and heat sources.

Sandhya *et al.* [22] analyzed the influences of HMT on magnetohydrodynamic circulation across a tilted permeable surface amidst synthetic responses. The investigation evaluated the mixed influences of MHD, HMT, and chemical reactions on the circulation parameters near an inclined porous plate. Oyekunle and Agunbiade [23] conducted a study on the influences of various parameters near an inclined magnetic field, on the magnetohydrodynamic circulation across a perforated perpendicular surface. The research evaluated the interplay of these factors on the dynamics of the unpredictable MHD slippage circulation across a perforated perpendicular surface, particularly considering the inclined magnetic field. Thamizh Suganya *et al.* [24] examined the sensitivity of factors in magnetohydrodynamic unconstrained turbulent circulation across an angled surface through a statistical analysis. The objective of the research was to conduct a thorough analysis and discourse on the mechanics of unconstrained convective circulation in MHD, with a particular focus on sloped surfaces. Sensitivity analyses were also performed on a range of influential parameters. Idowu and Falodun [25] explored the effects of thermophoresis and Soret-Dufour on the heat and mass transfer flow of magnetohydrodynamics non-Newtonian nanofluids over an inclined plate. The study explored the impact of these phenomena on the HMT parameters in the presence of magnetohydrodynamics and, an inclined plate. Riaz *et al.* [26] examined the unconstrained convective circulation of magnetohydrodynamics over an upward surface, taking into account scaled thermal levels, synthetic responses, and particle factors. The investigation evaluated the interplay of these factors on the circulation characteristics over a perpendicular surface.

A probability investigation was performed by Praveen Kumar Dadheech *et al.* [27] on radiative inclined magnetohydrodynamic slip circulation with a thermal origin in a permeable environment, taking into account 2 distinct liquids. The research explored entropy variations in the context of radiative inclined MHD slip flow with a heat source, particularly for two distinct fluids within a porous medium. The convective movement of fluid over an angled surface was investigated by Azhar Ali Zafar *et al.* [28] in the presence of thermal along with matter movement. The study evaluated the dynamics of free-convection flow influenced by magnetohydrodynamics. Utilizing mathematical techniques, Darapuneni Purna Chandra Rao *et al.* [29] examined the features of liquid circulation. The research was centered on the Darcy-Forchheimer movement of a Ree-Eyring liquid throughout an angled surface, with organic processes factored into consideration. Raghunath *et al.* [30] investigated the dynamics of magnetohydrodynamic fluid flow. The study focused on an inclined vertical porous plate under unsteady conditions, considering the impact of various parameters. The influence of HMT on the velocity of a magnetohydrodynamic Casson solution was examined by Vijayaragavan *et al.* [31]. The study specifically considered the presence of an inclined plate. The influence of heat dispersion and an angled magnetic environment on the unimpeded convective circulation of Casson liquid was examined by Pavan Kumar *et al.* [32]. The research explored the interaction of different variables with an angled surface within an electrical environment. The impact of emission, diffusive heat, organic responses, and erratic spontaneous convection around an angled perpendicular surface was investigated by Suresh Babu *et al.* [33], with a specific focus on the consequences of oriented magnetization. Raghunath Kodi and Obulesu Mopuri [34] analyzed the unsteady hydrodynamic flow over an inclined plate embedded in a porous medium, considering a Soret-aligned magnetic field and chemical reaction.

Using the Galerkin FEM, Shankar Goud Bejawada *et al.* [35] examined the movement characteristics of a magnetized tiny liquid with molecular reaction and inertial dispersion. An investigation was conducted by Husna Izzati Osman *et al.* [36] regarding unconstrained vortex movement in the vicinity of an infinitely slanted surface. In their investigation, Tad and Ahmed [37] examined the unimpeded convective circulation of MHD across a slanted permeable surface. They took into account various factors including the thermal origin, Soret impact, organic response, sticky dissolution, as well as electromagnetic warming. The influence of heat diversification on circulation within an angled rapid segmented surface with uninterrupted material dispersion was examined by Nagarajan *et al.* [38].

Bang Chuol Nhial *et al.* [39] investigated the effects of material transmission and radioactivity on magnetohydrodynamic (MHD) unconstrained circulation across an angled surface. The mechanics of unstable magnetohydrodynamic liquid circulation over a tilted orthogonal perforated surface were investigated by Kodi Raghunath *et al.* [40]. In addition to emission, synthesized reactions, and synchronized electromagnetic areas, the investigation examined the possibility of Soret impacts. Mohana Ramana *et al.* [41] examined the effects of an oriented magnetic environment as well as organic processes on the erratic MHD Kuvshinski liquid circulation across an angled perforated surface. The investigation also analyzed the existence of emissions and other influences. Nasir Shehzad *et al.* [42] examined the impact of magnetohydrodynamics movement on multiple layers within a permeable slanted rotational conduit employing conventional as well as unconventional liquids. Ali Raza and colleagues [43] researched magnetohydrodynamics in the context of an inclined face. The introduction of nanofluids through conventional heat methods was crucial to their research. An investigation was undertaken by Sivakumar and Muthucumaraswamy [44] to examine the impact of emissions on the conical circulation encircling a perpendicular infinitely homogeneous surface. Additionally, chemical reaction influences and progressively enhanced material dispersion were accounted for in the investigation. The mechanics of erratic magnetohydrodynamic cyclical Casson liquid circulation across an angled perpendicular permeable surface were explored by Raghunath and Mopuri [45]. The study included considerations for chemical reactions, heat absorption, and Soret effects. Sundar Raj *et al.* [46] examined the impact of chemical reactions on an inclined isothermal vertical plate. The study delved into the velocity profile under various conditions of T_H, T_G, and S_C. Nur Syahirah Wahid *et al.* [47] examined the behavior of a magnetohydrodynamic combination of tiny liquids by combined flow over a decreasing porous slanted surface, taking into account the impact of heat emission. Huang [48] investigated the heat and mass transfer in a fluid undergoing convective flow along an inclined plate through a porous medium, considering the effects of chemical reaction and activation energy. Prabhakar Reddy *et al.* [49] conducted a finite difference computational study to evaluate the influence of thermal diffusion and chemical reaction on unsteady free convective radiative magnetohydrodynamic flow past an exponentially accelerated inclined permeable plate. This study considered a plate embedded in a saturated porous medium of uniform permeability with variable temperature and concentration. Raju *et al.* [50] examined the unsteady MHD flow of an incompressible water-based Jeffrey nanofluid (containing Cu and TiO_2) across a stretched sheet in a transverse magnetic field, taking into account thermal radiation and Soret effects. Rajaraman and Muthucumaraswamy [51] have investigated the impact of chemical reactions, viscous dissipation, and thermal radiation on MHD flow past an oscillating plate.

No experts have yet offered a quantitative exploration into how chemical reactions impact an unsteady linearly accelerated inclined plate with uniform temperature and variable mass diffusion. Consequently, this present study aims to examine the influence of chemical reactions on such a scenario of a linearly accelerated inclined plate with uniform temperature and variable mass diffusion. The study used the Laplace transform approach to precisely solve the non-dimensional governing equations.

Analysis

When examining the irregular motion of a viscous fluid as it passes over a surface that is constantly inclined in a straight line and protrudes at an offset to the vertical plane. While the x-orientation axis is aligned transverse to the straight surface, the y-orientation is aligned parallel to it. While $t_3^* \le 0$ the surface as well as liquid subsist at consistent temperatures F_∞^*. While $t_3^* > 0$ the surface is accelerated $u = u_0\, t_3^*$ inside its surface, its degree is elevated N_w^*. The material is moved from the surface to the fluid. Successive compositions employing traditional Boussinesq's assumption thus govern the irregular movement. The geometrical model of the problem is shown below.

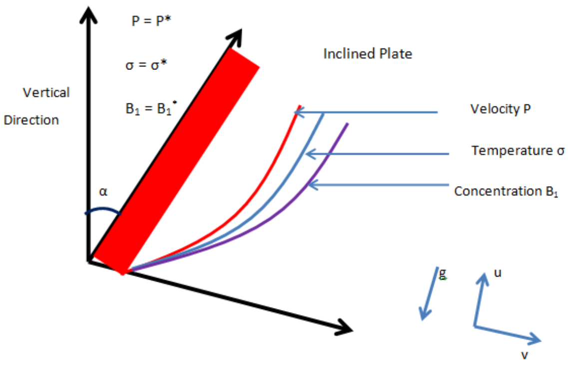

Physical Model

$$\frac{\partial u}{\partial t_3^*} = g\cos\alpha^*(F^* - F_\infty^*)\beta_2 + g\cos\alpha^*(N^* - N_\infty^*)\beta_2^* + \nu\frac{\partial^2 u}{\partial y^2}$$

$$\begin{aligned}\rho C_p \frac{\partial F^*}{\partial t_3^*} &= k\frac{\partial^2 F^*}{\partial y^2}\\ \frac{\partial N^*}{\partial t_3^*} &= D\frac{\partial^2 N^*}{\partial y^2} - K_l N^*\end{aligned} \tag{1}$$

At initial as well as circumferential circumstances:

$$\begin{array}{llllll} & u = 0, & F^* = F_\infty^*, & N^* = N_\infty^* & forall & y, t_3^* \le 0\\ t_3^* > 0: & u = u_0 t_3^*, & F^* = F_w^*, & N^* = N_w^* & at & y = 0\\ & u \to 0 & F^* \to F_\infty^*, & N^* \to N_\infty^* & as & y \to \infty\end{array} \tag{2}$$

Here, $A = \left(\frac{u_0^2}{\nu}\right)^{\frac{1}{3}}$

Upon the presentation of the pertinent devoid of dimension factors:

$$\begin{aligned}&P_2^* = \frac{u}{(\nu u_0)^{\frac{1}{3}}}, t = t_3^*\left(\frac{u_0^2}{\nu}\right)^{\frac{1}{3}}, Y = y\left(\frac{u_0}{\nu^2}\right)^{\frac{1}{3}},\ K_2^* = K_l\left(\frac{\nu}{u_0^2}\right)^{\frac{1}{3}},\\ &\sigma^* = \frac{F^* - F_\infty^*}{F_w^* - F_\infty^*}, Gr = \frac{g\beta_2(F_w^* - F_\infty^*)}{u_0}, B_1^* = \frac{N_\infty^* - N_\infty^*}{N_w^* - N_\infty^*},\\ &Gc = \frac{g\beta_2^*(N_w^* - N_\infty^*)}{u_0}, Pr = \frac{\mu C_p}{k}, sc = \frac{\nu}{D}\end{aligned} \tag{3}$$

Eqs. (1) and (4), results in:

$$\begin{aligned}\frac{\partial P^*}{\partial t} &= \sigma^*\ Gr\cos\alpha^* + B_1^*\ Gc\cos\alpha^* + \frac{\partial^2 P_2^*}{\partial Y^2}\\ \frac{\partial \sigma^*}{\partial t} &= \frac{1}{Pr}\frac{\partial^2 \sigma^*}{\partial Y^2}\\ \frac{\partial B_1^*}{\partial t} &= \frac{1}{sc}\frac{\partial^2 B_1^*}{\partial Y^2} - K_2^*\, B_1^*\end{aligned} \tag{4}$$

Regarding non-dimensional factors, the initial and final restrictions were

$$\begin{array}{llllll} & P_2^* = 0, & \sigma^* = 0, & B_1^* = 0 & forall & Y, t \le 0\\ t > 0: & P_2^* = t, & \sigma^* = 1, & B_1^* = t & at & Y = 0\\ & P_2^* \to 0, & \sigma^* \to 0, & B_1^* \to 0 & as & Y \to \infty\end{array} \tag{5}$$

Solution

We apply the Laplace transform to both sides of the dimensionless arithmetic statements in Eq. (4), ensuring they comply with the threshold requirement specified in Eq. (5)

$$\sigma^* = erfc\left(Z_2^*\sqrt{\Pr}\right) \tag{6}$$

$$\begin{aligned}B_1^* = \frac{t}{2}\Big[&\exp(2Z_2^*\sqrt{K_2^*\, t\, sc})\, erfc(Z_2^*\sqrt{sc} + \sqrt{K_2^*\, t}\,)\\ &+ \exp(-2Z_2^*\sqrt{K_2^*\, t\, sc})\, erfc(Z_2^*\sqrt{sc} - \sqrt{K_2^*\, t}\,)\Big]\\ -\frac{z_2^*\sqrt{sc}\ t}{2\sqrt{K^*}}\Big[&\exp(-2Z_2^*\sqrt{K_2^*\, t\, sc})\, erfc(Z_2^*\sqrt{sc} - \sqrt{K_2^*\, t}\,)\\ &- \exp(2Z_2^*\sqrt{K_2^*\, t\, sc})\, erfc(Z_2^*\sqrt{sc} + \sqrt{K_2^*\, t}\,)\Big]\end{aligned} \tag{7}$$

$$P_2^* = \left(1 - d - \frac{b}{c(1 - sc)}\right) t\left[\left(1 + 2Z_2^{*2}\,\Pr\right) erfc\left(Z_2^*\right) - \frac{2Z_2^*}{\sqrt{\pi}}e^{-Z_2^{*2}}\right] - \frac{b}{c^2(1 - sc)}$$

$$
\begin{aligned}
&-\frac{b\,e^{ct}}{2c^2(1-sc)}\left[\exp(2Z_2^*\sqrt{ct})\,erfc(Z_2^*+\sqrt{ct}) + \exp(-2Z_2^*\sqrt{ct})\,erfc(Z_2^*-\sqrt{ct})\right]\\
&+d\;t\left[\left(1+2Z_2^{*2}\Pr\right) erfc\left(Z_2^*\sqrt{\Pr}\right)-\frac{2Z_2^*\sqrt{\Pr}}{\sqrt{\pi}}e^{-Z_2^{*2}\Pr}\right]\\
&-\frac{b}{2c^2(1-sc)}\Big[\exp(2Z_2^*\sqrt{K_2^*t\,sc})\,erfc(Z_2^*\sqrt{sc}+\sqrt{K_2^*t})\\
&\qquad\qquad + \exp(-2Z_2^*\sqrt{K_2^*tsc})\,erfc(Z_2^*\sqrt{sc}-\sqrt{K_2^*t})\Big]\\
&-\frac{b\,t}{2c(1-sc)}\Big[\exp(2Z_2^*\sqrt{K_2^*tsc})\,erfc(Z_2^*\sqrt{sc}+\sqrt{K_2^*t})\\
&\qquad\qquad + \exp(-2Z_2^*\sqrt{K_2^*tsc})\,erfc(Z_2^*\sqrt{sc}-\sqrt{K_2^*t})\Big]\\
&+\frac{bz_1^*\sqrt{t\,sc}}{2c\sqrt{K^*}(1-sc)}\Big[\exp(2Z_2^*\sqrt{K_2^*t\,sc})\,erfc(Z_2^*\sqrt{sc}+\sqrt{K_2^*t})\\
&\qquad\qquad + \exp(-2Z_2^*\sqrt{K_2^*t\,sc})\,erfc(Z_2^*\sqrt{sc}-\sqrt{K_2^*t})\Big]\\
&+\frac{d\,t^2}{6}\left[\left(3+12Z_2^{*2}\Pr+4Z_2^{*4}\Pr^2\right)erfc(Z_2^*\sqrt{\Pr})-\frac{Z_2^*\sqrt{\Pr}}{\sqrt{\pi}}\left(10+4Z_2^{*2}\Pr\right)e^{-Z_2^{*2}\Pr}\right]\\
&+e_1\frac{e^{ct}}{2}\Big[\exp(2Z_2^*\sqrt{sc(K_2^*+c)t})\,erfc(Z_2^*\sqrt{sc}+\sqrt{(K_2^*+c)t})\\
&\qquad\qquad + \exp(-2Z_2^*\sqrt{sc(K_2^*+c)t})\,erfc(Z_2^*\sqrt{sc}-\sqrt{(K_2^*+c)t})\Big]\\
&-\frac{e_1}{2}\left[\exp(2Z_2^*\sqrt{K_2^*tsc})\,erfc(Z_2^*\sqrt{sc}+\sqrt{K_2^*t}) + \exp(-2Z_2^*\sqrt{K_2^*tsc})\,erfc(Z_2^*\sqrt{sc}-\sqrt{K_2^*t})\right]\\
&-\frac{b\,e^{ct}}{2c^2(1-sc)}\Big[\exp(2Z_2^*\sqrt{(K_2^*+c)t\,sc})\,erfc(Z_2^*\sqrt{sc}+\sqrt{(K_2^*+c)t})\\
&\qquad\qquad + \exp(-2Z_2^*\sqrt{(K_2^*+c)tsc})\,erfc(Z_2^*\sqrt{sc}-\sqrt{(K_2^*+c)t})\Big]
\end{aligned}
\tag{8}
$$

where, $a = Gr\cos\alpha^*$, $b = Gc\cos\alpha^*$, $c = \dfrac{K_2^*sc}{1-sc}$, $d = \dfrac{a}{1-\Pr}$, , $Z_2^* = \eta = \dfrac{Y}{2\sqrt{t}}$.

Skin friction

The non-dimensional plate friction factor seems to be:

$$
\begin{aligned}
&\tau=-\left(\frac{\partial P_2^*}{\partial y}\right)_{y=0}\\
&\tau=2(1-d+cbe_1+e_1)\sqrt{\frac{1}{\pi t}}+dt\left(-2\sqrt{\frac{pr}{\pi t}}\right)-\frac{e_1e^{ct}}{2}\left[\sqrt{c}\,erfc\left(\sqrt{ct}\right)-\frac{2e^{-ct}}{\sqrt{\pi t}}-\sqrt{c}\,erfc\left(\sqrt{ct}\right)\right]\\
&-\frac{e_1}{2}\left[-2\sqrt{\frac{sc}{\pi t}}e^{-K_2^*t}+\sqrt{k\,sc}\left(erfc\left(\sqrt{K_2^*t}\right)-erfc\left(-\sqrt{K_2^*t}\right)\right)\right]\\
&+\frac{e_1\sqrt{sc}}{4\sqrt{K_2^*}}\left(erfc\left(-\sqrt{K_2^*t}\right)-erfc\left(\sqrt{K_2^*t}\right)\right)\\
&-\frac{c\,e_1\sqrt{t}}{4}\left[-2\sqrt{\frac{sc}{\pi t}}e^{-K_2^*t}+\sqrt{K_2^*\,sc}\left(erfc\left(\sqrt{K_2^*t}\right)-erfc\left(-\sqrt{K_2^*t}\right)\right)\right]\\
&-\frac{e_1e^{ct}}{4\sqrt{t}}\left[-4\sqrt{\frac{sc}{\pi}}e^{-(K_2^*+c)t}+2\sqrt{sc(K_2^*+sc)t\left(\left(erfc\left(\sqrt{(K_2^*+c)t}\right)-erfc\left(-\sqrt{(K_2^*+c)t}\right)\right)\right)}\right]
\end{aligned}
\tag{9}
$$

where, $e_1 = \dfrac{b}{c^2(1-sc)}$.

Sherwood number (Sh)

Sh is given by:

$$
\begin{aligned}
&Sh=-\left(\frac{\partial B_1^*}{\partial y}\right)_{y=0}\\
&Sh=-\frac{\sqrt{t}}{4}\left[2\sqrt{K_2^*\,t\,sc}\;erfc\left(\sqrt{K_2^*t}\right)-\frac{2\sqrt{sc}}{\sqrt{\pi}}e^{-K_2^*t}-2\sqrt{K_2^*\,t\,sc}\;erfc\left(-\sqrt{K_2^*t}\right)-\frac{2\sqrt{sc}}{\sqrt{\pi}}e^{-K_2^*t}\right]\\
&\qquad+\frac{\sqrt{t\,sc}}{4\sqrt{K_2^*}}\left[erfc\left(-\sqrt{K_2^*t}\right)-erfc\left(\sqrt{K_2^*t}\right)\right]
\end{aligned}
\tag{10}
$$

Nusselt number (Nu)

Nu is given by

$$
\begin{aligned}
&Nu=-\left(\frac{\partial\sigma^*}{\partial y}\right)_{y=0}\\
&Nu=\sqrt{\frac{pr}{\pi t}}
\end{aligned}
\tag{11}
$$

RESULTS AND DISCUSSION

To attain a more comprehensive comprehension of the issue at hand, analytical formulas were used to examine the fluctuations in speed, heat, and composition. A variety of mathematical variables, including the slope direction, molecular response variable, heat and material differential values, Sc, Pr, and t, were utilized in these calculations. All of these variables significantly influence the characteristics of movement as well as transportation processes that occur inside an environment that incorporates water vapor as well as airflow.

The solutions derived through Laplace transforms are written concerning exponential functions and complementary error functions. These mathematical representations provide a framework to comprehend how these parameters intricately influence various parameters. They offer valuable insights into the collective impact of these parameters on the dynamics of flow and transport.

Figure 1 demonstrates how concentration profiles change over time for different values of the chemical reaction parameter K_2^*. The graph shows a decrease in wall concentration due to chemical reactions occurring within the system.

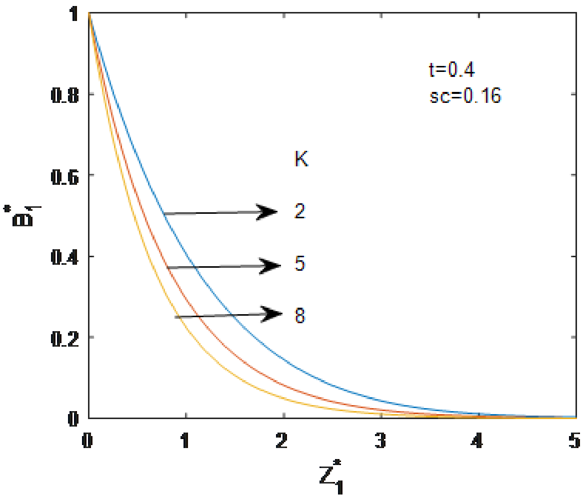

Figure 1. Concentration profile for 'K'.

Figure 2 illustrates how velocity profiles change over different time intervals, showing a consistent increase in velocity as time passes. This gradual acceleration in velocity suggests a dynamic shift within the system, with velocities steadily rising over time. These observations provide valuable insights into how the system evolves temporally, shedding light on how flow dynamics change with time. This trend underscores the system's responsiveness, demonstrating how velocities evolve and potentially escalate as the study progresses. Recognizing the connection between velocity and time is crucial for grasping the system's transient nature and understanding how flow dynamics evolve.

This progressive increment in velocity over time signifies an evolving dynamic within the system. Such insights into the temporal evolution of velocity profiles are crucial for understanding the system's behavior and the change of flow dynamics concerning time. This trend highlights the system's response, showcasing how velocities evolve and potentially intensify as the temporal aspect of the study progresses. Understanding this relationship between velocity and time is essential for comprehending the system's transient behavior and the temporal evolution of flow dynamics.

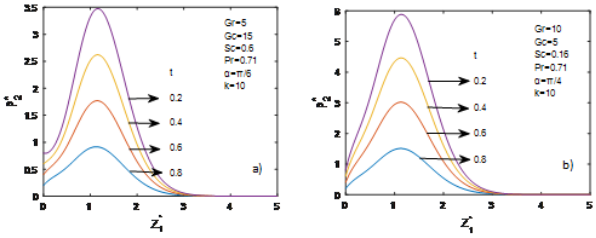

Figure 2. Velocity profiles for different values of 't':(a) α=π/3, k=10, Pr=0.71, Sc=0.6, Gr=5, Gc=15; (b) α = π/4, k=10, Pr=0.71, Sc=0.16, Gr=10, Gc=5.

In Figure 3, the visualization illustrates the influence of velocity across various contexts. The diagram demonstrates a trend where velocity increases as the CRP (Chemical Reaction Parameter) decreases. This observed relationship highlights an essential aspect of the system's behavior, suggesting that lower reaction parameter values are associated with higher velocities. This indicates a possible inverse relationship between the chemical reactions occurring in the system and the resulting flow dynamics. Understanding this trend offers valuable insights into how changes in the reaction parameter distinctly affect and potentially control the speed patterns within the studied environment.

This observed relationship between the velocity and the reaction parameter signifies a crucial aspect of the system's behavior. It suggests that lower values of the reaction parameter correspond to heightened velocities, indicating a potentially inverse relationship between chemical reactions occurring in the system and the resulting flow dynamics. Understanding this trend provides valuable insights into how variations in the reaction parameter distinctly influence and potentially modulate the speed contours within the studied environment.

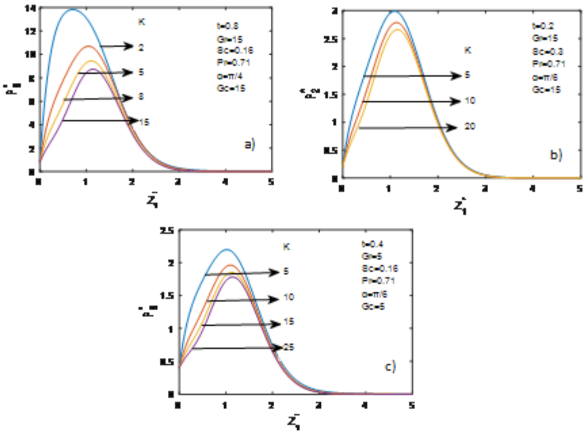

Figure 3. Velocity profiles for different values of 'K': (a) α=π/4, t=0.8, Pr=0.71, Sc=0.16, Gr=15, Gc=15; (b) α=π/6, t=0.2, Pr=0.71, Sc=0.3, Gr=15, Gc=15; c) α=π/6, t=0.4, Pr=0.71, Sc=0.16, Gr=5, Gc=5.

Figure 4 illustrates the velocity patterns for various Grashof numbers (Gr). In both figures, a clear trend is evident: as the Grashof number increases, the velocity within the system rises significantly. This pattern underscores the considerable impact of the Grashof number on flow dynamics across different inclinations. Grasping this correlation is vital for understanding how changes in the Grashof number distinctly influence and potentially control flow behaviors within diverse system configurations and inclinations.

This observed pattern underscores the substantial influence of Grashof numbers on flow dynamics across different inclinations. Understanding this correlation is essential for comprehending how variations in the Grashof number distinctly affect and potentially regulate flow behaviors within various system configurations and inclinations.

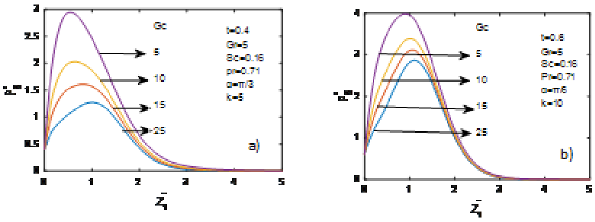

Figure 4. Velocity profiles for different values of 'Gc': (a) α=π/3, k=5, t=0.4, Pr=0.71, Sc=0.16, Gr=5; (b) α = π/6, k=10, t=0.6, Pr=0.71, Sc=0.16, Gr=5.

Figure 5 illustrates the impact of velocity (v) across a range of Grashof numbers at a 30° inclination.

The visualization reveals a direct relationship: as the Grashof number rises, velocity also increases proportionally. Both diagrams consistently show that higher Grashof numbers lead to increased velocity within the system. This pattern highlights the significant role of the Grashof number in affecting flow dynamics at various inclinations. Understanding this correlation is crucial for comprehending how variations in the Grashof number influence and potentially control flow behaviors in different system configurations and inclinations.

Both diagrams consistently demonstrate that as the Grashof number escalates, the velocity within the system also increases. This pattern emphasizes the significant influence of Grashof numbers on flow dynamics at varying inclinations. Understanding this correlation is pivotal for grasping how changes in the Grashof number impact and potentially govern flow behaviors within different system configurations and inclinations.

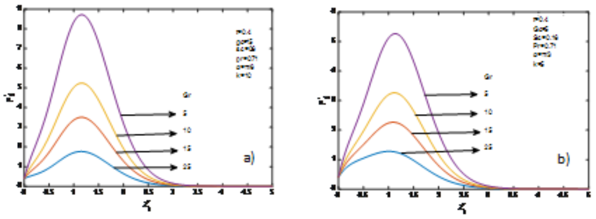

Figure 5. Velocity profiles for different values of 'Gr': (a) α=π/6, k=10, t=0.4, Pr=0.71, Sc=0.6, Gc=15; (b) α = π/3, k=5, t=0.4, Pr=0.71, Sc=0.16, Gc=5.

In Table 1, the relationship between various variables and their influence on local skin friction is outlined. It's observed that Pr, Sc, and inclination α are associated with an upward trend in skin friction, indicating that changes in these factors lead to an increase in frictional forces experienced. Conversely, Gr and Gc show a contrasting impact, suggesting that as time progresses, alterations in these parameters result in a reduction in local skin friction. This distinction highlights the diverse effects these variables have on friction over time, with some causing an escalation and others a decline in this specific physical phenomenon.

Table 1. Skin friction values for various parameters.

α (°)	t	Gr	Gc	sc	pr	K_1'	τ
30	0.6	2	2	0.16	7	2	5.9457
60	0.8	5	2	0.16	0.71	2	5.6004
60	0.6	5	5	0.3	0.71	2	5.4963
30	0.2	2	5	0.3	7	10	4.6919
45	0.2	2	5	0.6	0.71	5	4.5596
45	0.2	5	5	0.6	0.71	5	3.9786
60	0.2	5	10	0.3	7	5	2.5862
45	0.4	2	2	0.16	7	5	1.5473
60	0.4	5	2	0.16	0.71	5	0.1611
30	0.4	5	2	0.16	0.71	2	-3.3517

Table 2 illustrates the relationship between Sh and sc concerning time (t). As Sh increases, Sc exhibits proportional growth. Meanwhile, as material transmission escalates, there is a concurrent increase in K_1^*.

Expanding on this, Table 2 demonstrates that changes in Sh directly impact the behavior of Sc, K_1^* concerning time. As Sh values rise, there is a consistent and proportional increase Sc, which indicates a close relationship between these two parameters. Simultaneously, the increase in material transmission coincides with a noticeable rise in K_1^* suggesting a correlation between the two factors. This table emphasizes how alterations in Sh and material transmission distinctly influence the dynamics of Sc, K_1^* over time.

Table 2. Sherwood number for various parameters.

t	sc	K_2^*	Sh
0.2	0.6	10	0.5502
0.2	0.6	5	0.4396
0.4	0.16	5	0.4293
0.6	0.16	2	0.4866
0.8	0.3	10	1.4631
0.6	0.3	10	1.1066
0.8	2.01	5	2.8177
0.4	2.01	2	1.0824
0.6	2.01	5	2.1432
0.2	0.3	5	0.3244

CONCLUSION

The study examines the effects of a first-order chemical reaction on the linearly accelerated inclined isothermal plate, considering variable mass diffusion. The dimensionless equations are solved using the Laplace transform technique. The impact of velocity and concentration is analyzed for various physical parameters. The findings reveal that the velocity increases as the phase angle α^* and the chemical reaction parameter K_l decrease. Conversely, this trend is reversed with respect to time t. Additionally, it is observed that concentration increases as the chemical reaction parameter decreases. Skin friction increases with the Prandtl number (Pr) and the inclination angle, while it decreases over time with higher thermal and mass Grashof numbers (Gr and Gc). As the Sherwood number (Sh) rises, mass transfer increases proportionally.

ACKNOWLEDGEMENT

The authors express their gratitude to the leadership at Panimalar Engineering College, Chennai, for their unwavering support throughout the execution of this research endeavor. Our institution has not provided any financial assistance or seed money to carry out the research work.

NOMENCLATURE

A	constant
N^*	species concentration in the fluid, mol/m^3
N_∞^*	species concentration away from the plate
Nw^*	species concentration near the plate
B_1^*	dimensionless concentration
C_p	specific heat at constant pressure, J/(kg K)
D	mass diffusion coefficient, m^2/s
Gc	Grashof number (mass)
Gr	Grashof number (thermal)
g	accelerated due to gravity, m/s^2
k	thermal conductivity, J/(m K)
K_2^*	chemical reaction
Ki	chemical reaction parameter
Pr	Prandtl number
Sc	Schmidt number
Sh	Sherwood number
Nu	Nusselt number
Fw^*	fluid temperature near the plate
F_∞^*	temperature away from the plate
F*	fluid temperature closer to the plate
t	dimensionless time
t_3^*	time
u	fluid velocity in the vertical direction, m/s
U_0	velocity of the plate, m/s
P_2^*	dimensionless velocity
x	spatial coordinate along the plate
y'	coordinate axis normal to the plate, m
y	dimensionless coordinate axis normal to the plate
Z_2^*	similarity parameter
Greek symbols	
α^*	Angle of inclination
β_2	volumetric coefficient of thermal expansion, 1/K
β_3^*	volumetric coefficient of expansion with concentration, 1/K
ν	kinematic viscosity, m^2/s
ρ	density of the fluid kg/m^3
τ	dimensionless skin-friction,kgs^2/m
σ^*	dimensionless temperature
erfc	complementary error function
Subscripts	
w	conditions at the wall
∞	conditions in the free stream

REFERENCES

[1] O.A. Bég, T.A. Bég, A.Y. Bakier, V.R. Prasad, Int. J. Appl. Math. Mech. 5(2) (2009) 39–57. https://www.scirp.org/reference/referencespapers?referenceid=207616.

[2] O. Aydm, A. Kaya, Heat Mass Transfer 46 (2009) 129–136. https://sci-hub.wf/10.1007/s00231-009-0551-4.

[3] R. Muthucumaraswamy, G. Nagarajan, V.S.A. Subramanian, Ann. Fac. Eng. Hunedoara 8 (2010) 220–225.https://annals.fih.upt.ro/pdf-full/2010/ANNALS-2010-3-45.pdf.

[4] R. Muthucumaraswamy, Chem. Ind. Chem. Eng. Q. 16 (2010) 167–173. https://doi.org/10.2298/CICEQ091231024M.

[5] V. Bisht, M. Kumar, Z. Uddin, J. Appl. Fluid Mech. 4 (2011) 59–63. https://doi.org/10.36884/jafm.4.04.11947.

[6] M. Sundar Raj, R. Muthucumaraswamy. V.S.A. Subramanian, Int. J. Appl. Mech. Eng. 16(3) (2011) 885–891. https://www.infona.pl/resource/bwmeta1.element.baztech-article-BPZ5-0017-0038.

[7] O.D. Makinde, ZNA 67a (2012) 239–247. https://doi.org/10.5560/zna.2012-0014.

[8] P. Rana, R. Bhargava, O.A. Bég, Comput. Math. Appl. 64 (2012) 2816–2832. https://doi.org/10.1016/j.camwa.2012.04.014.

[9] M.S. Alam, M. Ali, M.D. Delowar Hossain, Int. J. Eng. Sci. 2(7) (2013) 81–88. https://www.theijes.com/papers/v2-i7/Part.6/K0276081088.pdf.

[10] R. Muthucumaraswamy, L. Jeyanthi, ARPN J. Eng. Appl. Sci. 10(20) (2015) 9596–9603 http://www.arpnjournals.org/jeas/research_papers/rp_2015/jeas_1115_2914.pdf.

[11] M. Narahari, S. Tippa, R. Pendyala, M.Y. Nayan, Recent Adv. Appl. Theor. Mech., Proc. WSEAS Int. Conf. (MECHANICS '15), 11th, 126–137 (2015). http://www.wseas.us/e-library/conferences/2015/Malaysia/APTHME/APTHME-15.pdf.

[12] H. Mondal, D. Pal, S. Chatterjee, P. Sibanda, Ain Shams Eng. J. 8 (2016) 2111–2121. https://doi.org/10.1016/j.asej.2016.10.015.

[13] F. Akter, M. Islam, A. Islam, S. Khan, S. Hossain, Open J. Fluid Dyn. 6 (2016) 62–74. http://dx.doi.org/10.4236/ojfd.2016.61006.

[14] Jyotsna Rani Pattnaik, Gouranga Charan Dash, Suprava Singh, Ain Shams Engineering Journal. 8(1) (2017) 67–75 http://dx.doi.org/10.1016/j.asej.2015.08.014.

[15] S. Khalid, M.A. Kamal, U. Rasheed, S. Farooq, S. Kussain, H. Waqas, J. Appl. Environ. Biol. Sci. 7(5) (2017) 154–165. https://www.textroad.com/pdf/JAEBS/J.%20Appl.%20Environ.%20Biol.%20Sci.,%207(5)154-165,%202017.pdf.

[16] S.V. Sailaja, B. Shanker, R. Srinivasa Raju, J. Nanofluids 6(3) (2017) 420–435. https://doi.org/10.1166/jon.2017.1337.

[17] R.K. Dhal, B. Jena, P.M. Sreekumar, Int. Res. J. Adv. Eng. Sci. 2(2) (2017) 299–303. http://irjaes.com/wp-content/uploads/2020/10/IRJAES-V2N2P239Y17.pdf.

[18] U.S. Rajput, Gaurav Kumar, Jordanian J. Mech. Ind. Eng. 11(1) (2017) 41–49. https://jjmie.hu.edu.jo/vol%2011-1/JJMIE-13-16-01.pdf.

[19] S. Agarwalla, N. Ahmed, Heat Transfer-Asian Res. (2017) 1–15. https://sci-hub.wf/10.1002/htj.21288.

[20] H. Mondal, D. Pal, S. Chatterje, P. Sibanda, Ain Shams Eng. J. 9(4) (2018) 2111–2121. https://doi.org/10.1016/j.asej.2016.10.015.

[21] M. Ahmad, M.A. Imran, M. Aleem, I. Khan, J. Therm. Anal. Calorim. 137 (2019) 1783–1796. https://doi.org/10.1007/s10973-019-08065-3.

[22] A. Sandhya, G.V. RamanaReddy, G.V.S.R. Deekshitulu, Int. J. Appl. Mech. Eng. 25 (3) (2020) 86–102. https://doi.org/10.2478/ijame-2020-0036.

[23] T.L. Oyekunle, S.A. Agunbiade, Oyekunle, A. Gunbiade, J. Egypt. Math. Soc. 28(51) (2020) 1–19. https://doi.org/10.1186/s42787-020-00110-7.

[24] S. ThamizhSuganya, P. Balaganesan, L. Rajendran, M. Abukhaled, Eur. J. Pure Appl. Math. 13(3) (2020). https://doi.org/10.29020/nybg.ejpam.v13i3.3730.

[25] A.S. Idowu, B.O. Falodun, Arab. J. Basic Appl. Sci. 27(1) (2020) 149–165. https://doi.org/10.1080/25765299.2020.1746017.

[26] M.B. Riaz, A. Atangana, S.T. Saeed, in Fractional Order Analysis: Theory, Methods and Applications, H. Dutta,

A.O. Akdemir, A. Atangana, Eds., John Wiley & Sons Inc., (2020) 253–282. https://sci-hub.se/https://doi.org/10.1002/9781119654223.ch10.

[27] P.K. Dadheech, P. Agrawal, A. Sharma, A. Dadheech, Q. Al-Mdallal, S.D. Purohit, Case Stud. Therm. Eng. 28 (2021) 101491. https://doi.org/10.1016/j.csite.2021.101491.

[28] A.A. Zafar, J. Awrejcewicz, G. Kudra, N.A. Shah, S.J. Yook, Case Stud. Therm. Eng. 27 (2021) https://doi.org/10.1016/j.csite.2021.101249.

[29] D.P.C. Rao, S. Thiagarajan, V. Srinivasakumar, Heat Transfer 50(7) (2021) 7120–7138. https://onlinelibrary.wiley.com/doi/10.1002/htj.22220.

[30] K. Raghunath, N. Gulle, R.R. Vaddemani, O. Mopuri, Heat Transfer 51(3) (2021) 2742–2760 https://onlinelibrary.wiley.com/doi/10.1002/htj.22423.

[31] R. Vijayaragavana, V. Bharathib, J. Prakash, Indian J. Pure Appl. Phys. 59 (2021) 28–39. https://pdfs.semanticscholar.org/7d14/5f4f87013207ba593f8d93ed60d2030d028d.pdf.

[32] C. PavanKumar, K. Raghunath, M. Obulesu, Turk. J. Comp. Math. Edu. 12(13) (2021) 960–977. https://turcomat.org/index.php/turkbilmat/article/view/8584/6710.

[33] R. SureshBabu, T. SaravanKumar, M.V. Govindaraju, B. Mallikarjuna, Biointerface Res. Appl. Chem. 11(5) (2021) 13252–13267. https://doi.org/10.33263/BRIAC115.1325213267.

[34] Raghunath Kodi, Obulesu Mopuri, Heat Transfer 51 (2021) 733–752. https://doi.org/10.1002/htj.22327.

[35] S.G. Bejawada, W. Jamshed, R. Safdar, Y.D. Reddy, M.M. Alanazi, H.Y. Zahran, M.R. Eid, Coatings 12(2) (2022) 151. https://doi.org/10.3390/coatings12020151.

[36] H.I. Osman, N.F.M. Omar, D. Vieru, Z. Ismail, J. Adv. Res. Fluid. Mech. Therm. Sci. 92(1) (2022) 18–27. https://doi.org/10.37934/arfmts.92.1.1827.

[37] B.K. Tad, N. Ahmed, Biointerface. Res. Appl. Chem. 12(5) (2022) 6280–6296. https://biointerfaceresearch.com/wp-content/uploads/2021/11/20695837125.62806296.pdf.

[38] G. Nagarajan, M. SundarRaj, R. Muthucumaraswamy, Int. J. Appl. Mech. Eng. 27(4) (2022) 105–116. https://doi.org/10.2478/ijame-2022-0053.

[39] B.C. Nhial, V.S. HariBabu, V.N. Vellanki, G.Y. Sagar, JPSP 6(5) (2022) 697–706. https://journalppw.com/index.php/jpsp/article/view/5861/3858.

[40] K. Raghunath, N. Gulle, R. R. Vaddemani, O. Mopuri, Heat Transfer 51(3) (2022) 2742–2760. https://doi.org/10.1002/htj.22423.

[41] R. MohanaRamana, K. VenkateswaraRaju, K. Raghunath, Heat Transfer 51(7) (2022) 6431–6449. https://doi.org/10.1002/htj.22598.

[42] N. Shehzad, A. Zeeshan, M. Shakeel, R. Ellahi, S. M. Sait, Coatings 12(430) (2022) 1–25. https://doi.org/10.3390/coatings12040430.

[43] A. Raza, U. Khan, Z. Raizah, S.M. Eldin, A.M. Alotaibi, S. Elattar, A.M. Abed, Symmetry 14 (2022) 2412. https://www.mdpi.com/2073-8994/14/11/2412.

[44] P. Sivakumar, R. Muthucumaraswamy, Gis Sci. J. 9(1) (2022) 167-177. 1869–9391. https://drive.google.com/file/d/1DKDzhYzeHz1QWap1sh dTcDFXAfyvDI-/view.

[45] K. Raghunath, O. Mopuri, Heat Transfer, 51 (2022), 733–752. https://doi.org/10.1002/htj.22327.

[46] M. SundarRaj, G. Nagarajan, V.P. Murugan, R. Muthucumaraswamy, Int. J. Appl. Mech. Eng. 28(2) (2023) 64–76. https://www.ijame-poland.com/pdf-168439-91810?filename=Impacts%20of%20chemical.pdf.

[47] N.S. Wahid, N.M. Arifin, N.S. Khashi, I. Pop, Alexandria Eng. J. 66 (2023) 769–783. https://doi.org/10.1016/j.aej.2022.10.075.

[48] J.S. Huang, J. Mech., 39(2023) 88–104. https://doi.org/10.1093/jom/ufad006.

[49] B. P. Reddy, M.H. Simba, A. Hugo, Hindawi Int. J. Chem. Eng. ID 9342174 (2023). https://doi.org/10.1155/2023/9342174.

[50] K.V. Raju, R. Mohanaramana, S. Sudhakar Reddy, K. Raghunath, Communications in Mathematics and Applications. 14(1) (2023) 237–255. https://doi.org/10.26713/cma.v14i1.1867.

[51] R. Rajaraman, R. Muthucumaraswamy, Chem. Ind. Chem. Eng. Q. 30 (3) 223—230 (2024). https://doi.org/10.2298/CICEQ230526025R.

NAGARAJAN GNANAVEL[1]
SUNDARRAJ MARIADOSS[1]
VENKATESAN JAYAVELU[2]
VENKATA MOHANREDDY POLAKA[3]
MUTHUCUMARASWAMY RAJAMANICKAM[4]

[1]Department of Mathematics, Panimalar Engineering College, Poonamallee, Chennai, Tamil Nadu, India

[2]Department of Mathematics, Rajalakshmi Engineering College, Thandalam, Chennai, Tamil Nadu, India

[3]Department of Mathematics, Saveetha School of Engineering, Saveetha Institute of Medical and Technical Sciences, Saveetha University, Chennai, Tamil Nadu, India

[4]Department of Applied Mathematics, Sri Venkateswara College of Engineering, Sriperumbudur, Tamil Nadu, India

NAUČNI RAD

UTICAJI HEMIJSKIH PROCESA NA NAGNUTU POVRŠINU PRI PROMENLJIVOJ MASI I KONSTANTNOJ TEMPERATURI

Istraživano je opsežno turbulentno strujanje oko neograničene nagnute ploče u uslovima ujednačene temperature i disperzije promenljive mase. Tokom ove analize, temeljno je razmatran uticaj hemijskih reakcija unutar sistema. Fokusirajući se na harmonijski nagib ploče unutar njene ravni, korišćen je pristup Laplasove transformacije za precizno rešavanje bezdimenzionalnih jednačina. U razmatranju različitih profila, istraživan je uticaj nekoliko ključnih fizičkih faktora: varijable hemijskog odgovora, Šmitov broj, termički Grashofov broj, maseni Grashofov broj i vreme. Ova studija se bavi složenim uticajem različitih faktora na složenu dinamiku protoka oko iskošenih ploča, posebno se fokusirajući na fenomene prenosa toplote i mase. Ispitujući ove odnose, ona pruža ključne uvide u poboljšanje efikasnosti procesa prenosa toplote i mase unutar sistema koji uključuju nagnute površine. Štaviše, ovo znanje može potencijalno doprineti napretku u različitim oblastima, od sistema obnovljivih izvora energije do proizvodnih procesa, gde prenos toplote i mase igra ključnu ulogu.

Ključne reči: nagnuta površina; prenos toplote; prenos mase; hemijska reakcija; Laplasove transformacije.

CI&CEQ
Chemical Industry & Chemical Engineering Quarterly

Available online at
Association of the Chemical Engineers of Serbia *AChE*
www.ache.org.rs/CICEQ

Chem. Ind. Chem. Eng. Q. 31 (2) 163–172 (2025) CI&CEQ

JACQUELINE ARNAUTOVIC NASCIMENTO[1]
PAULO ROBERTO BRITTO GUIMARÃES[2]
REGINA FERREIRA VIANNA[1]

[1]Escola Politécnica, Universidade Federal da Bahia. Curso de Engenharia química, Salvador, BA, Brasil

[2]BAHIAINVESTE - Empresa Baiana de Ativos, Salvador - Bahia

SCIENTIFIC PAPER

UDC 678.743:628.3:547.322.32:66

OPTIMIZATION OF THE VINYL-MONOCHLORIDE RECOVERY PROCESS FOR THE REDUCTION OF COSTS AND ENVIRONMENTAL IMPACT

Article Highlights

- The steady-state simulation of a Vinyl Chloride recovery unit made up of three condenser banks
- Use of parametric sensitivity analysis to evaluate the influence of operational parameters
- Optimizing and proposing improvements to the existing system based on parametric sensitivity
- Development of a process monitoring tool using a commercial simulator

Abstract

Reducing environmental impacts in the production processes is the focus of large industries. In the PVC production process, the loss of vinyl monochloride (VCM) through an incineration stream of inert materials is a point of attention due to the emission of greenhouse gases. VCM is lost as part of the stream of uncondensed gases from the VCM recovery unit. The optimization of the VCM recovery process was carried out by modeling the industrial system and running it using a process simulator. The unit model and simulation results have been verified through plant operating data. Sensitivity analyses were performed to identify which independent variables improved the VCM condensation rate. Based on plant operating experience, three independent variables were selected and their influence on the VCM recovery flow rate was verified: pressure, the composition of the input stream, and utility water flow rate. After the sensitivity analysis, the plant operating pressure was selected for optimization, resulting in the additional quarterly recovery of 7.5 tons of VCM and a reduction of more than 5 tons of natural gas fuel, that is, an annual reduction of 23 tons of fuel, which represents 53 tons of CO_{2eq}*. Overall, the annual savings amount to US\$15,000 and US\$1,060 by reducing the consumption of fuel gas alone. Therefore, by ensuring greater VCM recovery, competitiveness improves by reducing production costs, and greenhouse gas emissions are reduced due to the decrease in gas incineration.*

Keywords: vinyl monochloride; simulation; heat exchangers in series; optimal operating conditions.

The environmental impacts caused by industrial processes and their contribution to climate change are one of the most important themes of our time, and developing solutions that reduce greenhouse gas (GHG) emissions is essential. At present, human society is dependent on plastics, among which is polyvinyl chloride (PVC) which uses vinyl monochloride (VCM) as raw material. One of the existing technologies for PVC production, and the one used in this study, is batch production, in which VCM, water, nitrogen, and other products are added to the polymerization reactor. After completion of the reaction, two streams result in a bottom stream composed of the PVC sludge, sent for drying, and a top stream composed of unreacted VCM and inert materials, sent

---

Correspondence: J.A. Nascimento, Escola Politécnica, Universidade Federal da Bahia. Curso de Engenharia química Rua Aristides Novis, No. 2, Cep 40210-630, Salvador, BA, Brasil.
E-mail: eng_jacqueline.nascimento@yahoo.com

Paper received: 25 August, 2023
Paper revised: 13 June, 2024
Paper accepted: 28 june, 2024

https://doi.org/10.2298/CICEQ230825024A

to the VCM recovery unit [1], where it goes through compression and condensation processes through a series of shell and tube heat exchangers, separating the VCM from other substances. The VCM is then distilled and recycled to the reactor feed. The stream of uncondensed gases is sent to an incinerator due to the presence of chlorinated organic vapors. This optimization study concentrates on the operating conditions of the set of shell and tube heat exchangers of the VCM recovery unit.

VCM is recognized as a carcinogen for humans and animals. Recent studies have reported that even below the minimum exposure limit, workers suffer health problems [2–6]. Over the years, possible harm to health was identified, and as a result, regulations have been created to define the maximum concentration of VCM in the final product, which drove the development and improvement of technologies to guarantee maximum recovery of VCM and meet the specifications that became more restrictive [7]. According to ASTM D3749, the maximum content allowed is 1 ppm mass [8]. In terms of environmental impacts, VCM has direct and indirect impacts. There is the possibility of contamination of groundwater reservoirs from the emission of chlorinated organic vapors, such as VCM, into the atmosphere, since, as they encounter rain, they become solubilized and percolate into the soil, reaching the groundwater reservoirs [9]. Halogenated solvents, particularly chloroethylene, are among the most prevalent pollutants [10]. Concerning indirect impacts, there are those due to the use of non-renewable sources of industrial utilities and raw materials for VCM production [11,12].

Several technologies have been developed over the years to maximize VCM recovery or minimize its emission from the recovery unit uncondensed gas stream, with varying recovery efficiencies. These technologies and their efficiencies are condensation and incineration (97%) [12], adsorption (95%) [13], absorption (99%) [14], and membrane (99.9%) [15], the latter being the most widely adopted. Combined methods, where two or more types of technologies are adopted in the same industrial process, are also used to increase the recovery efficiency of the uncondensed gas stream [12–16].

Other studies have already been carried out in similar systems in an attempt to increase the recovery efficiency of VCM. For condensation technology, sensitivity analyses were reported based on the temperature variation of cooling fluids, thermal exchange area, pressure increase, and cooling fluid exchange, and only the possibilities for economic gains were highlighted [17]. Other studies evaluate the efficiency of other VCM recovery methods, where the results do not include CO_{2eq} values [12–16]. This optimization study is based on the condensation and incineration technology of an operating plant and is aimed at identifying the best system operating conditions to increase VCM recovery and, therefore, reduce both production costs and GHG emissions by using less fossil fuels in the incinerator. The actual efficiency of this system is 95.5% [18].

Process description

In the PVC polymerization reaction, there is a surplus of VCM that is recovered from the reactors and sent to a tank at ambient conditions for subsequent treatment and use [17,18]. The recovery of the monomer from the reactors is done using a vacuum, and due to the lack of tightness, air enters the system. Furthermore, nitrogen is added to the process and is recovered together with the VCM at the end of the batch, which determines the composition of the system's input stream [18].

From this tank, the VCM treatment process is undertaken. The gaseous stream leaving this tank passes through a compression unit, before entering the condensing unit, whose system pressure is maintained within an operational range of 490.0 kPa (g) to 686.5 kPa (g) by a pressure control valve, and the temperature, as a pressure-dependent variable, between 70 °C and 90 °C. In the condensing unit, a series of shell and tube heat exchangers carry out the VCM condensation process using different cooling fluids on the shell side. The condensed monomer is treated and subsequently used as a fraction of the polymerization reactor loads for PVC and the uncondensed remainder is sent for incineration.

As air and nitrogen are admitted, the composition varies according to natural process oscillations, and the presence of these gases has a strong effect on the MVC recovery rate.

VCM condensation system

The system studied in this work is highlighted in Figure 1 and is based on an existing industrial unit, which consists of a series of four shell-and-tube heat exchangers, divided into three stages. The first has two heat exchangers operating in parallel and the others have two condensers operating in series. As the pressure is constant and controlled by an automatic control valve, the temperature range required to condense the VCM throughout the process is obtained using water, diethylene glycol, and liquid VCM as cooling fluids in the 1st, 2nd, and 3rd stages, respectively.

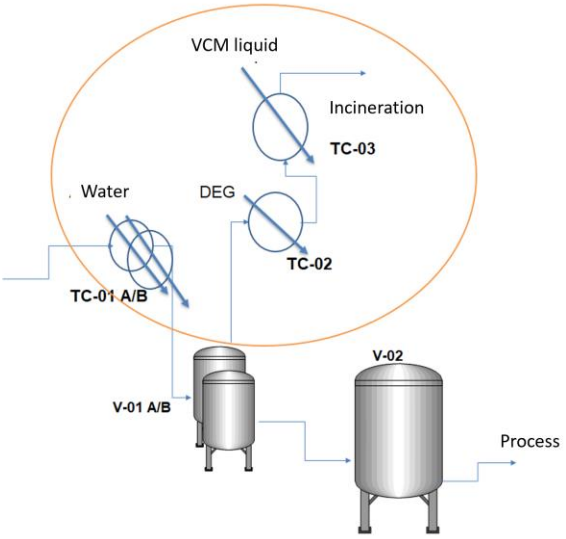

Figure 1. VCM recovery unit heat exchange system.

MATERIAL AND METHODS

Materials

The modeling and simulation of the VCM condensation system were undertaken using the Aspen Plus commercial simulator with the Aspen Exchanger Design and Rating (EDR) extension adopting the rigorous simulation method [19], in steady-state condition. The thermodynamic models selected and verified through literature data were Peng Robinson [20,21] and Soave Redlich Kwong [19]. The simulation results were verified by comparison to operating data from an existing industrial plant.

The selection of variables to be optimized was based on plant operational experience. From this selection, parametric sensitivity analyses were carried out using the direct method, where one variable is changed (independent variable), and the results of the other variables in the system are evaluated (dependent variables). In this study, the main dependent variable evaluated was the VCM flow sent to incineration, and the independent variables selected were based on plant operating experience: pressure, composition of the input stream, and utility water flow rate. Then, to correlate the VCM loss flow rate with the independent variable, regressions were developed due to the simulation results that allowed these sensitivity evaluations to be undertaken.

After the sensitivity analysis, the industrial process was optimized by selecting the variables that influenced VCM recovery, thus generating the results of this work in relation to the reduction of GHG emissions due to lower consumption of natural gas fuel in the incinerator and the economic impact of lower VCM loss.

In the end, proposals for future work were made that aim to increase the efficiency of the VCM recovery in this process stream.

Simulation set-up

The first step was the selection of the thermodynamic models, which were based on research works that evaluated similar systems and obtained good results. The models that have shown the best results are the Peng Robinson [20,21] and Soave Redlich Kwong [17] models, and so were selected to be used in the present work.

Secondly, process conditions of the system input stream were added [19]. Temperature, pressure, and flow rate were collected from online instruments of the existing industrial unit, while stream composition was determined by chromatography through the collection and analysis of five different samples.

The actual geometries of the heat exchangers were collected from the design drawings and introduced into the simulator using the Aspen Exchanger Design and Rating (EDR)® vs.11 extensions and later added to Aspen Plus® vs.11, adopting the type HeatX exchanger, in Simulation mode with a rigorous method to evaluate the behavior of the variables [19].

The heat exchanger system shown in Figure 1 was implemented in Aspen Plus ® vs. 11 according to the flowchart in Figure 2. The TC-01 A/B heat exchanger promotes much of the VCM condensation in this system. The liquid phase (LIQ2) is accumulated in the V-01 A/B vessels. The gaseous flow (ENT-TC-02) goes to the second stage (TC-02) condenser, resulting in two output streams: a gaseous phase (inerts with some residual VCM-GAS3) and a liquid phase (LIQ6) which also returns to the V-01 A/B vessels. The gaseous phase is directed to the TC-03 (GAS3) condenser, which uses the liquid VCM (heat of vaporization) in the shell side to condense part of the VCM from the process stream. The resulting gaseous stream is sent to incineration (VENTA) and the liquid part (LIQ5) returns to the V-01A/B vessels.

Due to the confidentiality of the industrial plant data, the input stream process variables, flow rate, pressure, and temperature are here described as ranges. The flow rate varies from 3 t/h to 10 t/h and the VCM mass concentration from 92% to 97%. The average mass composition of the five samples analyzed is 92.7% VCM, 0.5% oxygen, 5.6% nitrogen, 0.1% CO, 0.6% CO_2, and 0.5% H_2O. The system pressure is maintained within an operational range of 490.0 kPa (g) to 686.5 kPa (g) by a pressure control valve, and the temperature, as a pressure-dependent

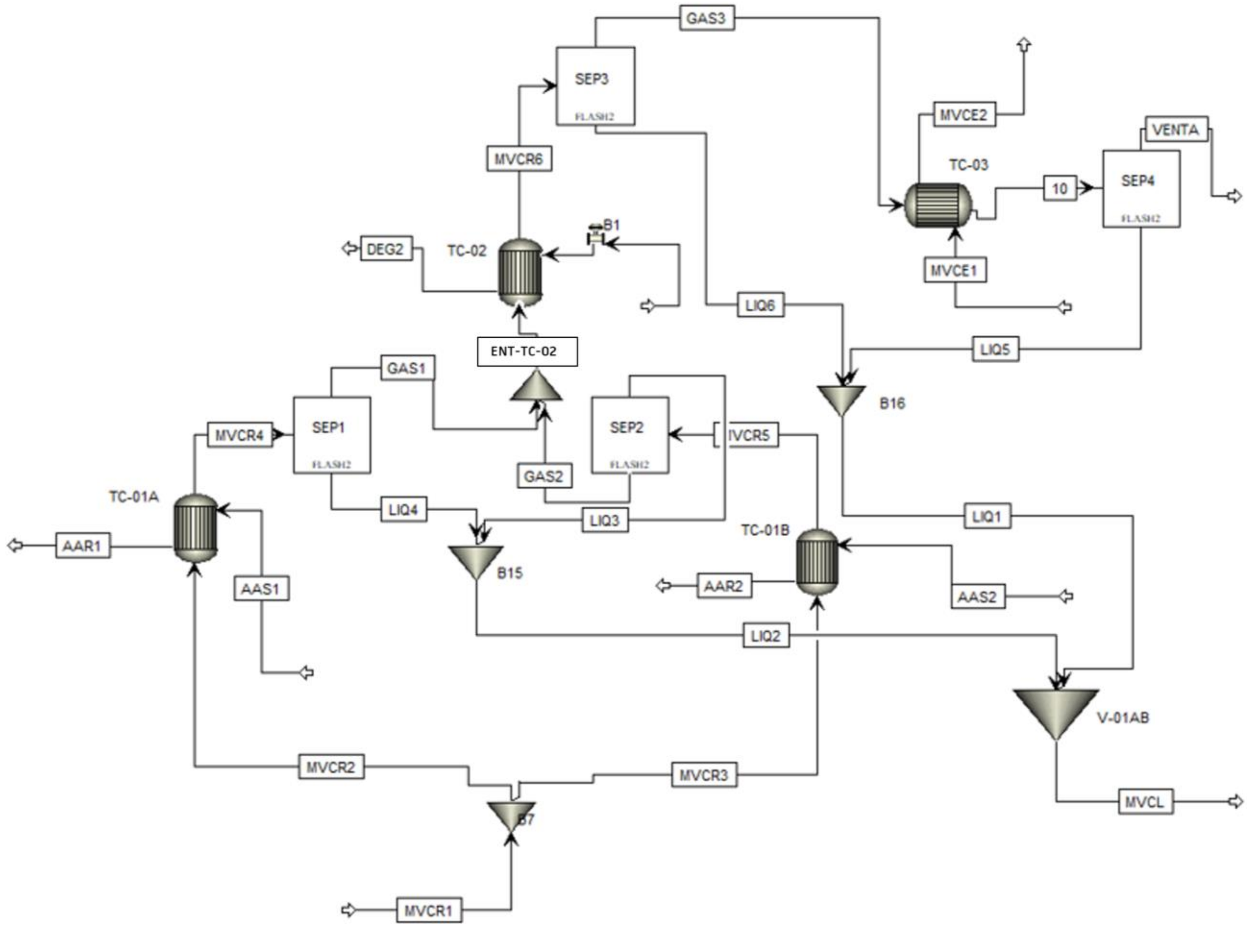

Figure 2. VCM recovery unit flowchart for process simulation.

variable, is between 70 °C and 90 °C.

The design flow rates were those adopted for the existing heat exchanger utilities. The cooling water flow rate was in the range of 26 t/h to 35 t/h, the diethylene glycol flow rate from 2 t/h to 3 t/h, and the VCM flow rate, as cooling fluid, from 0.2 t/h to 0.25 t/h, all operating in the shell side of the heat- exchangers.

Model and simulation verification

To verify the simulation results, comparisons were made between the simulated VCM flow rates sent to the incinerator and the actual flow rates observed at the industrial unit. For each sample of the input stream, samples of the output stream for incineration were collected and analyzed, and these laboratory results were used to verify the simulation results. A total of ten simulations using the Peng Robinson and Soave Redlich Kwong models were carried out adopting the five samples and their respective process variables: conditions of both the input and utility streams at the time of sample collection.

Once the simulation model had been verified, sensitivity evaluations were made possible and subsequently undertaken.

Parametric sensitivity analyses

For the sensitivity analyses the direct method, in which the operating parameters are varied one at a time and the effects on the system responses are analyzed, was selected [17,22,23]. The focus was to observe the trajectory of the operating system and the behavior of the VCM recovery flow rate as a function of each variable.

Based on operational experience, the following parameters were varied: operating pressure, feed composition, and cooling water flow rate to the TC-01A/B heat exchangers. The dependent variables were temperature, composition (VCM concentration), and flow rates of the process streams, including the output stream for incineration, the focus of this work.

Adopting fictitious initial pressure values of 5 kgf/cm²g, a mass composition of VCM (92.7%), O_2 (0.5%), N_2 (5.6%), CO (0.1%), CO_2 (0.6%), H_2O (0.5%) and water flow of 26 t/h, the variations carried out in the simulator were: pressure: +5%, +10%, +25%, +30%, inert composition: -10%, -5%, +5%, +10%, +30% and cooling water flow: -20%, -10%, +10%, +20%.

Process optimization

After sensitivity analyses, process optimization was proposed. An effort vs. impact [24] matrix was used to select the variables based on operational experience and with the results of the VCM reduction from the optimization, it was possible to quantify the economic and environmental gains.

Economic and environmental results

To evaluate the economic gain, Eq. (1) was used. Eqs. (2–5) were used to calculate the amount of natural gas that was saved [25].

$$Savings\left(\$\right)=\frac{8100h}{y}\cdot VCM\ \text{recovery}\ \left(t/h\right)\cdot \text{Price}\ VCM\left(\$/h\right)$$
$$+m_{ng}\left(t/y\right)\cdot \text{natural gas price}\ \left(\$/t\right) \quad (1)$$

$$Q_{VCM\ \text{combustion}}=Q_{\text{natural gas combustion}} \quad (2)$$

$$\left(PCI\cdot \dot{m}\right)_{VCM}=Q_{\text{natural gas combustion}} \quad (3)$$

$$Q_{\text{natural gas combustion}}=\left(PCI\cdot \dot{m}\right)_{ng} \quad (4)$$

$$m_{ng}=\dot{m}_{ng}\cdot time \quad (5)$$

where PCI is the lower heating value (GJ/t of VCM) and (GJ/t of natural gas), $\dot{m}_{VCM}$ is the mass flow rate of the recovered VCM in t/h, $\dot{m}_{ng}$- mass flow rate of recovered natural gas in t/h, and m_{ng} is mass natural gas in t.

Knowing the amount of natural gas (ng) that was not burned, it is possible to calculate the amount of CO_{2eq}, through Eq. (6). The fuel conversion factor for CO_{2eq} is derived from the Boiler/Furnace Protocol: EPA AP-42, which indicates which constant should be used for the conversion and is obtained from the average composition of the fuel. In the case of natural gas used in the industrial plant under study, the conversion factor is 2.26 t of CO_2/t of natural gas [26].

$$CO_{2eq}=m_{ng}\cdot 2.26\frac{t\ CO_2}{t\ ng} \quad (6)$$

RESULTS AND DISCUSSION

Simulation

Figure 3 shows the differences between the simulation results and the actual plant data for the flow rates of VCM loss in the uncondensed gas stream for each thermodynamic model. The results had a maximum difference of 9.7% for the PR model and 10.4% for the SRK model. These deviations are considered acceptable, both because flow rate instruments have a measurement error of up to 10%, and the flow rate of VCM to be incinerated is 20 times smaller than the main process stream. Based on these results, the Peng Robinson model was selected to continue with the evaluations in this study.

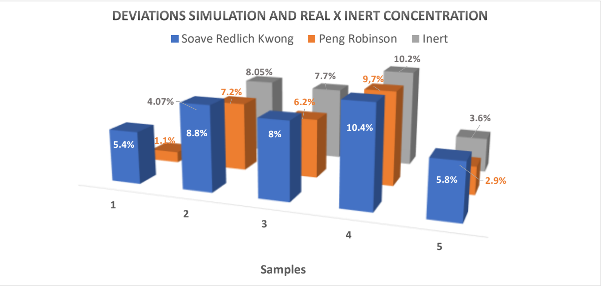

Figure 3. Deviations between the simulation results and actual plant data.

Parametric sensitivity analyses

The results of the disturbances in the independent variables chosen on the VCM flow rate to incineration are presented in Figure 4.

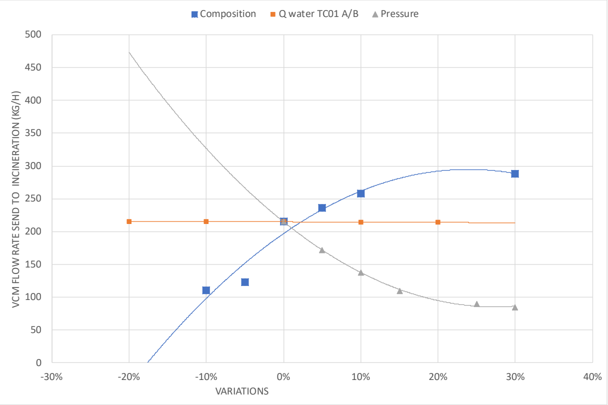

Figure 4. VCM flow rate to incineration after process changes.

In Figure 4, it is possible to observe that both composition (N_2 concentration) and pressure have impacts on the VCM recovery results, while the change in water flow rate did not affect the studied variable.

Effects of pressure variation

Figure 4 shows an inverse relationship between the system pressure and the flow rate of VCM loss to incineration. This is because the equilibrium temperature for condensing the VCM increases with increasing pressure. Therefore, for a fixed volume (the installed equipment has a fixed capacity), the higher the pressure, the greater the difference between the temperatures of the cold and hot sides in the condenser, which improves heat exchange and, consequently, increases the amount of VCM condensed for the same process conditions of utilities and installed equipment [25].

The amount of VCM loss to incineration, in kg/h, as a function of system pressure, in kPa, is represented by Eq. (7) obtained by the data regression method with an R^2 of 0.9987.

$$\dot{m}_{VCM\ \mathrm{lost}} = 34.959P^2 - 624.01P + 2{,}869.5 \tag{7}$$

The minimum point of the curve is described by Eqs (8) and (9) and indicates the lowest flow rate of VCM loss and the corresponding system pressure. Using the minimum value of the method [27] represented by these equations, the minimum flow rate of VCM loss is 84.89 kg/h at a pressure of 874.8 kPa(g).

$$\dot{m}_{VCM\ \mathrm{lost}} = -\frac{\Delta}{4\alpha} \tag{8}$$

where, $\Delta = b^2 - 4ac$ (9)

and parameters *a*, *b*, and *c*, 34.959; 624.01 and 2,869.5, respectively, are taken from Eq, (7).

Effects of composition variation

Of all the variables analyzed, according to Figure 4, the change in composition had the greatest impact on the VCM condensation rate. This can be explained by the higher concentration of Nitrogen (inert) in the input stream, which pressurizes the system and forces the pressure control valve to open more frequently. As a result, there is a greater loss of VCM due to the drag effect, as well as greater difficulty in condensation due to the reduction in the partial pressure of the VCM in the mixture, which, by getting smaller, ends up requiring a lower temperature for phase change (equilibrium conditions). This same effect can be evidenced in Figure 3, in which samples 2, 3, and 4 showed greater deviations between the simulated values and the actual of the industrial unit.
A better understanding of the effect on the VCM partial pressure can be shown by adopting Eq. (10), Dalton's law [28].

$$p_i = y_i P \tag{10}$$

If the total pressure of the system is the sum of the partial pressures of each substance in the mixture, keeping the pressure constant (due to the pressure control valve), the greater the concentration of Nitrogen, the greater its partial pressure and the lower the pressure partial VCM in the mixture, as shown by Eq. (11), in which the arrows illustrate the increasing (↑) or decreasing (↓) trends of each variable).

$$\begin{gathered} p_{N_2}\uparrow + p_{O_2}\downarrow + p_{CO_2}\downarrow + pH_2O\downarrow + p_{VCM}\downarrow = \\ \left(y_{N_2} + y_{O_2} + y_{CO_2} + y_{H_2O} + y_{CO} + y_{VCM}\right)P \end{gathered} \tag{11}$$

Therefore, as the system volume is constant because the installed equipment does not undergo structural changes, the lower the saturation pressure, the lower the temperature must be to condense the VCM. However, it is not possible to easily adjust the temperature of utilities in the industrial plant due to the needs of other consumers present in the distribution network of water, diethylene glycol, and liquid VCM used in the shell side of TC-03, which reduces the efficiency of VCM recovery in the process stream.

The relationship between the increase in Nitrogen in the system and the flow rate of VCM loss to incineration is directly proportional, as can be seen in Figure 4 and in Eq. (12), which represents the correlation of the composition (flow rate) of N_2 with the flow rate of VCM loss, with an R^2 of 1.0.

$$\begin{aligned} \dot{m}_{VCM\ \mathrm{lost}} &= 2\cdot 10^{11}N_2^{\,4} - 4000N_2^{\,3} + 3\cdot 10^{9}N_2^{\,2} \\ &\quad -10^{8}N_2 - 2\cdot 10^{6} \end{aligned} \tag{12}$$

To find the lowest possible values of VCM loss to incineration, the solutions of this equation would be necessary, but the equation has no real roots. Despite this, as explained previously, the smaller the amount of N_2, the higher the condensation of VCM and, so, the greater its recovery. Therefore, the Nitrogen concentration should be reduced as much as possible.

Effects of cooling water flow rate variation

As can be seen in Figure 4, the flow rate of cooling water in the shell side of the TC-01 A/B heat exchangers has almost no effect on the amount of condensed VCM. This can be explained by the correlation Eq.13 that describes the sensible heat exchange of pure liquids [25].

$$Q_{cold} = \dot{m}_{cold}\, Cp\Delta T \tag{13}$$

For example, a 30% increase in water flow rate would provide about 30% more sensible heat, which would increase VCM recovery by only 3.11%, for the existing process conditions.

The regression of the data presented in Figure 4 led to Eq. (14), which represents the correlation of the cooling water flow with the VCM loss flow rate with an R^2 of 0.9905.

$$\dot{m}_{VCM\ \mathrm{loss}} = -3\cdot 10^{-9}Q^2 - 10^{-4}Q + 214.08 \tag{14}$$

To eliminate the loss of VCM, the water flow must be increased to 250,985.7 t/h, which in practice would not be possible since the two heat exchangers are not large enough, making it necessary to install a new one, in addition to the fact that the heat exchanger system cooling water is already fully used by other process demands.

Process optimization

Using an effort vs. impact matrix [24], the pressure was selected as the initial variable to be optimized because it is easily manipulated and requires no initial investment.

To increase the operating pressure of the VCM recovery unit, it was first necessary to evaluate the maximum permitted working pressure conditions to avoid equipment ruptures and damage to installations. An analysis of equipment documentation indicated that the pressure could be safely increased by up to 14% in relation to the current operating value. To evaluate the possible gains from this change, an additional simulation was undertaken with the new proposed pressure condition.

Then, after the pressure change, a new simulation was carried out to optimize the system based on the composition: 20% reduction in Nitrogen in the input stream, also based on the effects of the inerts in this system.

Simulation results for the pressure value adjustment

Simulations were performed for the five feed compositions and their respective flow rates for the pressure set 14% above the present operating condition. The results of the flow rate of VCM sent to incineration evaluated with the new pressure compared to the present plant data are shown in Table 1.

Table 1. Comparison of VCM loss before and after pressure adjustment.

Samples	Present VCM loss (kg/h)	VCM loss after a 14% increase in pressure (kg/h)	Variation (%)
1	174.0	173.2	-0.5%
2	574.3	612.1	6.6%
3	478.4	503.4	5.2%
4	636.4	697.1	9.5%
5	99.9	94.3	-5.6%

Table 1 shows that the pressure adjustment of 14% is not enough to increase the recovery efficiency of the VCM of all samples, indicating that the amount of inerts in the process stream has a strong effect on the dependent variable, as can be seen in the results of samples 2, 3, and 4. Therefore, the higher concentration of inerts affects the equilibrium pressure of VCM and, consequently, reduces its condensation rate compensating in some amount the effect of pressure increase. However, based on operating experience, it was expected that the increase of pressure would reduce the loss of VCM to a certain extent, as the control valve would both reduce the frequency of openings (depressurization), thus reducing the drag effect, and result in a VCM partial pressure higher than the present value, thus improving heat exchange. Besides, carrying out this change in the industrial plant is easy and does not require any investment.

Simulation results for the composition value adjustment

After the pressure change, a simulation was carried out to optimize the system based on a 20% reduction in Nitrogen in the input stream, also based on the effects of the inerts in this system, and the results of the sensitivity analysis are represented in Table 2.

The proposal to reduce 20% of N_2 flow is based on the risk of VCM emission to the atmosphere, because this Nitrogen will be sent to a safety vent, and by increasing the amount of N_2, the greater the probability of dragging more VCM [18].

Table 2. Results of the amount of VCM loss vs. reduction of N_2 in the input stream.

Samples	Present VCM loss (kg/h)	Simulation results VCM loss (kg/h)	-20% of N_2-VCM loss (kg/h)	Reduction of VCM loss (kg/h)*	% Reduction
1	178.2	176.1	115.8	62.4	34.2
2	336.7	355.0	229.0	107.7	35.2
3	389.1	418.0	311.3	77.8	25.5
			Average	82.6	

$$^{*}\text{Reduction } \dot{m}_{VCM\ \mathrm{loss}} = \text{Present } m_{VCM\ \mathrm{loss}} - \left(m_{VCM\ \mathrm{loss}}\,\textit{after less than } 20\% \text{ of } N_2\right) \tag{15}$$

Economic and environmental analysis

Pressure adjustment

Pressure adjustment was implemented in the plant through a test plan. After three months, the financial and environmental results were evaluated based on the internal VCM indicator used to produce PVC, these values being presented in Table 3.

It can be observed that the increase in the VCM recovery rate occurred consistently throughout the three months with a reduction of around 5 t in the consumption of natural gas in the incinerator. As the process is not constant, variations in the concentrations of substances in the process mean that the amount of VCM loss is not constant. As a premise for calculating the amount of VCM loss over the period, the difference between the average flow rate of VCM loss (t/h) in the previous year and the average rate of VCM loss during the three months was considered.

Table 3. Results of the reduced amount of VCM loss over 3 months.

Month	VCM reduction (t)	NG reduction (t)	Total Savings (US$)
1	2.3	1.54	1,047
2	3.2	2.17	1,472
3	2.0	1.35	916
TOTAL	7.5	5.06	3,435

To evaluate the economic gain, Eq. (1) was used. Eqs (2–5) were used to calculate the amount of natural gas that was saved [25]. Knowing the amount of natural gas (ng) that was not burned, it was also possible to calculate the amount of CO_{2eq}, through Eq. (6).

Thus, from Table 3, US$ 3,435 could be saved over the three months due to lower consumption of natural gas and VCM loss, since the recovered VCM is recycled. In one year, savings would reach almost US$ 15,000/y, US$ 1,060 only from the reduction in fuel gas consumption. Based on the average recovery value of VCM during the three months, it would be possible to reduce CO_{2eq} emissions by up to 53 t/y.

Composition adjustment

Based on the average reduction of 82.6 kg/h (Table 2), the savings are calculated by the Eq. (1), using the Equations (2–5). Besides this, due to the environmental analysis, Eq. (6), it would be possible to reduce 1,080 t/y of CO_{2eq} emissions and generate savings of up to US$ 300,000/y, Eq. (1).

Further improvements would require investments and therefore a technical and economic evaluation study is recommended to evaluate the most adequate solution between changing to a technology with better efficiency or carrying out structural changes to reduce the concentration of Nitrogen in the input stream.

CONCLUSION

The selection of optimal operating conditions for a VCM recovery process has been undertaken through the systematic application of computer simulations and economic analyses. The unit models and plant simulation were verified against actual plant operating data and the maximum error between the actual and simulated VCM compositions was around 9.7%, which is considered adequate due to the accuracy of the plant instruments and considering the simulation objectives.

A sensitivity analysis was carried out to identify the set of parameters that affected the loss of VCM and among the selected variables, both the operating pressure and the composition of the feed were those that most affected the VCM loss for incineration. However, when carrying out a stress impact analysis it became clear that manipulating the composition of the feed is not as easy as adjusting the setpoint of the PSVs of the vessels and the pressure control valve. Therefore, the plant pressure was increased by 14%, which made it possible to reduce by 7.5 t the VCM loss and reduce consumption by 5 t of natural gas, which represents savings of US$ 3,435. Annually there is the possibility of reducing CO_{2eq} emissions by 53 t from 23 t of fuel saved, which represents US$ 15,000.

Despite the financial and environmental savings, there was no significant increase in the recovery efficiency of the VCM when compared to the theoretical efficiency of the system (97%) [12].

For future work, in relation to other technologies that have better VCM recovery efficiency [12–16], it is recommended that a technical and economic evaluation study be carried out to verify whether changing the technology would make sense for this industrial unit, or whether the solution of changing the composition of the input stream by reducing the concentration of inerts would be more appropriate, as preliminary results showed that a reduction of 20% in N_2 would allow increasing the recovery efficiency of VCM with the reduction of 1,080 t/y of CO_{2eq} emissions and annual savings of up to US$ 300,000.

Another achievement of this work was the development of the simulation strategy, which made it possible to create a procedure that helps the unit operational team in making more assertive decisions, as well as enabling the identification of process deviations more quickly, which guarantees better competitiveness since it lowers the correction time.

NOMENCLATURE

Cp	Heat capacity
CO	Carbon monoxide
CO_2	Carbon dioxide
CO_{2eq}	Carbon dioxide equivalent
DEG	Diethylene glycol
EDR	Exchanger design and rating
GHG	Greenhouse gases
H_2O	Water
$\dot{m}_{cold}$	Mass flow rate of the cold product in t/h
m_{ng}	Mass natural gas in t
$\dot{m}_{ng}$	Mass flow rate of recovered natural gas in t/h
$\dot{m}_{VCM}$	Mass flow rate of recovered VCM in t/h
$\dot{m}_{VCM\ loss}$	Mass flow rate of vinyl chloride loss in t/h
N_2	Nitrogen
O_2	Oxygen

P	Pressure in the system
p_{CO2}	Carbon dioxide partial pressure
PCI	Lower heating value (GJ/t of VCM) and (GJ/t of natural gas)
p_{H2O}	Water partial pressure
p_i	Partial pressure of a component *i* in a mixture
p_{N2}	Nitrogen partial pressure
p_{VCM}	Vinyl chloride partial pressure
p_{O2}	Oxygen partial pressure
ppm	Part per million
PR	Peng Robinson
PSV´s	Pressures relief valves
PVC	Polyvinyl chloride
Q	Total heat
Q_{cold}	Cold heat
R^2	Correlation factor
SRK	Soave Redlich Kwong
TC-01 A/B	First heat exchange of the system
TC-02	Second heat exchange of the system
TC-03	Third heat exchange of the system
VCM	Vinyl chloride
y_{CO}	Carbon monoxide composition in the mixture
y_{CO2}	Carbon dioxide composition in the mixture
y_{H2O}	Water composition in the mixture
y_{N2}	Nitrogen composition in the mixture
y_{O2}	Oxygen composition in the mixture
y_{VCM}	Vinyl chloride composition in the mixture
y_i	Component *i* in a gaseous mixture
ΔT	Delta temperature

REFERENCES

[1] W.A. Michael, V. Giovanni, Vinyl Chloride Polymers. Encyclopedia of Polymer Science and Technology. John Wiley & Sons. Ed. 8, Herman F. Mark, New York (2002) 437–475. ISBN: 9780471440260.

[2] M.R. Azari, R. Tayefeh-Rahimian, M.J. Jafari, H. Souri, Y. Shokoohi, A. Tavakol, Z. Yazdanbakhsh, Toxicol. Ind. Health 32(12) (2016) 1921–1926. http://doi.org/10.1177/0748233715596663.

[3] R.N. Wheeler Jr, Environ. Health Perspect. 41(1981) 123–128. https://doi.org/10.1289/ehp.8141123.

[4] IARC Monographs on the Evaluation of Carcinogens Risks to Humans, 7th ed., World Health Organization, Lyon (1974) 291-305. ISBN 978-92-832-1207-2.

[5] S. Alberto, M. Davide Di, C. Marisa, M. Stefania, M. Alessandro, I. Sergio, Arch. Environ. Occup. Health 77(5) (2022) 372–381. https://doi.org/10.1080/19338244.2021.1900045.

[6] U. Fedeli, P. Girardi, G. Gardiman, D. Zara, L. Scoizzato, MN. Ballarin, M. Baccini, R. Pirastu, P. Comba,G. Mastrangelo, Am. J. Ind. Med. 62(1) (2019) 14–20. https://doi.org/10.1002/ajim.22922.

[7] G.C.Bertram. Environ. Sci. Technol. 11 (9) (1977) 864–868. https://doi.org/10.1021/es60132a014.

[8] World Health Organization, European Commission, ICSC 0082, vinyl monochloride CAS: 75-01-4. https://www.ilo.org/dyn/icsc/showcard.display?p_version=2&p_card_id=0082&p_lang=es.

[9] L. C. GOMES, Master Thesis, University of Paraná and University of Bragança, Portugal (2021).

[10] F.S. Rodrigo, G.M.N. Luis, Rev. Cienc. Exatas Apl. Tecnol. 5(1) (2013) 12–26. https://doi.org/10.5335/ciatec.v5i1.3119.

[11] R. Monica, Doctoral Dissertation, California State University, Long Beach, USA (2022).

[12] Central Pollution Control Board, Minimizing Release and Environmental Implications of Chlorine and its Compounds, Ministry of Environment & Forests, Delhi (2008) 21–24. https://cpcb.nic.in/openpdffile.php?id=UmVwb3J0RmlsZXMvTmV3SXRlbV8xMzdfY2hsb3JpbmVfcGFja2FnZS5wZGY=.

[13] C. Paulo, R.M. Ana, R.E. Alírio, F. Alexandre, Aiche J. 66 (5) (2020). https://aiche.onlinelibrary.wiley.com/toc/15475905/2020/66/5.

[14] K.E. John, (Geon Co), EP0027805B1 (1980).

[15] J. L. Richard, H. W. Mark, W. G. Johannes, K. Juergen, Aiche J. 32 (10) (1993) 2236-2241. https://doi.org/10.1021/ie00022a006.

[16] P.J. Piyush, T.G. Clay, H.J. Edward, S.S. Carl, US3984218A (1976).

[17] A. Fedak, Master Thesis, University of Aveiro, Portugal (2011).

[18] N. A. Jacqueline. Master Thesis, University of Bahia, Brazil (2023).

[19] H. Juma, Chemical Process Design and Simulation: Aspen Plus and Aspen Hysys Applications, Wiley-AIChE (2019). ISBN: 978-1-119-08911-7.

[20] F.P. Renato, Master Thesis, University of Campina Grande, Brazil (2009).

[21] C.D. Neves, J.M.D. Oliveira, Resultados da simulação estática da torre de destilação de VCM e antipolimerizante. Braskem´s report intern. (2017).

[22] G.L. Silva, R.A.F. Lima, Master Thesis, University of Pernambuco, Brazil (2007).

[23] M.R. Souza, Master Thesis, University of Bahia, Brazil (2016).

[24] R. Vargas. Gestão Industrial de A a Z, 1st ed., CreateSpace Independent Publishing Platform, Brazil (2015). ISBN: 1505837308.

[25] P.F. Incropera, D. P. DeWitt, T.L. Bergman, A.S. Lavine, Fundamentals of heat and mass transfer, 6th ed., John Wiley & Sons, New York (2006). ISBN: 978-0471457282.

[26] Air Emissions Factors and Quantification. Protocol Boiler/Furnace: EPA AP-42, Ed. 5. Chapter 1, Sections 1.1, 1.3, 1.4 and 1.5., EPA- United States Environmental Protection Agency (https://www.epa.gov/air-emissions-factors-and-quantification/ap-42-fifth-edition-volume-i-chapter-1-external-0). [Accessed on 02 January 2022].

[27] Unacademy. Understanding Maximum and Minimum Value of Quadratic Equation (unacademy.com) [Accessed on 02 July 2023]. https://unacademy.com/content/upsc/study-material/mathematics/maximum-and-minimum-value-of-quadratic-equation/.

[28] J.M. Smith, H.C. Van Ness, M.M. Abbott, Introdução à Termodinâmica da Engenharia Química, LTC Ed. 8, São Paulo (2020). ISBN:9788521636847.

JACQUELINE ARNAUTOVIC NASCIMENTO[1]
PAULO ROBERTO BRITTO GUIMARÃES[2]
REGINA FERREIRA VIANNA[1]

[1]Escola Politécnica, Universidade Federal da Bahia. Curso de Engenharia química, Salvador, BA, Brasil
[2]BAHIAINVESTE – Empresa Baiana de Ativos, Salvador – Bahia

NAUČNI RAD

OPTIMIZACIJA PROCESA REKUPERACIJE VINIL-MONOHLORIDA ZA SMANJENJE TROŠKOVA I UTICAJA NA ŽIVOTNU SREDINU

Smanjenje uticaja na životnu sredinu u proizvodnim procesima je fokus velikih industrija. U procesu proizvodnje PVC-a, gubitak vinil monohlorida (VCM) kroz insineraciju struje inertnih materijala je tačka pažnje zbog emisije gasova sa uticajem staklene bašte. VCM se gubi kao deo toka nekondenzovanih gasova iz jedinice za oporavak VCM. Optimizacija procesa rekuperacije VCM je sprovedena modelovanjem industrijskog sistema i njegovim pokretanjem pomoću simulatora procesa. Model jedinice i rezultati simulacije su verifikovani preko radnih podataka postrojenja. Urađene su analize osetljivosti da bi se identifikovale koje nezavisne promenljive su poboljšale stepen kondenzacije VCM. Na osnovu iskustva u radu postrojenja, izabrane su tri nezavisne promenljive i verifikovan je njihov uticaj na povratni protok VCM: pritisak, sastav ulaznog toka i protok komunalne vode. Nakon analize osetljivosti, izabran je radni pritisak postrojenja za optimizaciju, što je rezultiralo dodatnim tromesečnim povratom od 7,5 tona VCM i smanjenjem više od 5 tona goriva prirodnog gasa, odnosno godišnje smanjenjem od 23 tone goriva, što predstavlja 53 tone CO_{2ek}*. Sve u svemu, godišnja ušteda iznosi 15.000 USD i 1.060 USD samo smanjenjem potrošnje goriva. Stoga, obezbeđivanjem veće rekuperacije VCM, konkurentnost se poboljšava smanjenjem troškova proizvodnje, a emisije gasova sa efektom staklene bašte se smanjuju usled smanjenja spaljivanja gasa.*

Ključne reči: vinil monohlorid; simulacija; serijski izmenjivači toplote; optimalni radni uslovi.